

**ORGANIC-INORGANIC HYBRID  
PEROVSKITES: SYNTHESIS,  
CHARACTERIZATION AND EVALUATION**

*A Thesis submitted  
in partial fulfillment for the Degree of*

**Doctor of Philosophy**

*By*

**NISHA BALACHANDRAN**

**SC16DO45**



**Department of Chemistry  
INDIAN INSTITUTE OF SPACE SCIENCE AND TECHNOLOGY  
THIRUVANANTHAPURAM  
NOVEMBER 2021**

*Dedicated to my family and teachers*





www.iist.ac.in

## भारतीय अंतरिक्ष विज्ञान एवं प्रौद्योगिकी संस्थान

(वि.अ.आयोग अधिनियम 1956 की धारा-3 के अधीन मान्यता प्राप्त विश्वविद्यालय घोषित)

भारत सरकार, अंतरिक्ष विभाग, वलियमला पोस्ट, तिरुवनंतपुरम 695 547 भारत

## INDIAN INSTITUTE OF SPACE SCIENCE AND TECHNOLOGY

(A Deemed to be University u/s 3 of the UGC Act, 1956)

Government of India, Department of Space

Valiamala P. O., Thiruvananthapuram 695 547 India

### CERTIFICATE

This is to certify that the thesis entitled '**ORGANIC-INORGANIC HYBRID PEROVSKITES: SYNTHESIS, CHARACTERIZATION AND EVALUATION**' submitted by **NISHA BALACHANDRAN (SC16DO45)** to the Indian Institute of Space Science and Technology, Thiruvananthapuram, in partial fulfilment for the award of the degree of **Doctor of Philosophy** is a *bonafide* record of research work carried out by her under our supervision. The contents of this project report, in full or in parts, have not been submitted to any other Institution or University for the award of any degree or diploma.

Dr. Dona Mathew  
Sci/Engr G  
Polymers and Special Chemicals Division  
PSCG, VSSC Thiruvananthapuram

Dr. Jobin Cyriac  
Associate professor  
Department of Chemistry  
IIST Thiruvananthapuram

Thiruvananthapuram

November 2021



Counter signature of HOD with seal

डॉ. के. प्रभाकरन / Dr. K. Prabhakaran  
आचार्य एवं अध्यक्ष / Professor & Head  
रसायन विभाग / Department of Chemistry  
भारतीय अंतरिक्ष विज्ञान एवं प्रौद्योगिकी संस्थान  
Indian Institute of Space Science and Technology  
अंतरिक्ष विभाग, भारत सरकार  
Department of Space, Government of India  
तिरुवनंतपुरम / Thiruvananthapuram - 695 547

## DECLARATION

I declare that this project report entitled “**Organic-Inorganic Hybrid Perovskites: Synthesis, Characterization And Evaluation**” submitted in partial fulfillment of the degree of Doctor of Philosophy is a record of original work carried out by me under the joint supervision of **Dr. Dona Mathew and Dr. Jobin Cyriac**, has not formed the basis for the award of any degree or diploma, in this or any other Institution or University. In keeping with the ethical practice in reporting scientific information, due acknowledgements have been made wherever the findings of others have been cited.

Nisha Balachandran  
SC16DO45

Thiruvananthapuram-695 547

Date: 1-11-2021

## ACKNOWLEDGEMENTS

First and above all, I would like to thank and praise God, the almighty, for providing me strength; courage and granting me the capacity to proceed successfully with this research work in such a reputed institution like Indian Institute of Space Science and Technology (IIST).

It gives me an immense debt of gratitude to express my sincere thanks to my research supervisors Dr. Dona Mathew, VSSC and Dr. Jobin Cyriac, IIST for giving me an opportunity to work under their supervision and also for their excellent guidance, inspiration, advice, continuous support and constant encouragement throughout my research work. I have been extremely fortunate to have these supervisors who cared so much about my work. Both my research supervisors had spent enough time discussing the experiments, data analysis and paper writing and gave me a lot of suggestions and support to overcome the difficulties during my Ph.D study. Both of them are very responsible and helpful, I respect their dedication. Without their support and help, the improvement gained on experimentation and writing could not be achieved. I would like to thank them for their guidance on writing scientific papers, including this PhD thesis and for correcting my papers by spending their valuable time.

I take this opportunity to thank Dr. S. Somanath, Director, IIST & VSSC and Dr. Vinay Kumar Dadhwal, former Director, IIST, for providing me with all the necessary facilities. I thank Dr. S. C. Sharma, Former DD, PCM and Dr. S.A Illangovan, DD, PCM for giving permission to join part-time Ph.D course. I would like to express my gratitude to Prof. Dr. Prabhakaran. K, HOD, Dept. of Chemistry, Prof. Kuruvilla Joseph, Dean S A and Dr. Nirmala Rachael James, Former HOD of Chemistry, IIST, for their support throughout my research work. I am thankful to Deans, Senior Professors, Professors, all the faculty members and staff of the Department of Chemistry, IIST for their support and encouragement. I would be thankful to my Doctoral Committee members; Dr. R. Rajeev (VSSC), Dr. Vijayakumar C. Nair (CSIR-NIIST), Dr. Jinesh K.B. (IIST), Dr. K.G. Sreejalekshmi (IIST) for their valuable suggestions and directives, which helped a lot throughout my research work.

I would be thankful to Dr. R Rajeev, Former Head, Analytical and Spectroscopy Division, VSSC, for giving me permission to register at IIST. I am deeply obliged to all members of the Analytical and Spectroscopy Division, VSSC,

particularly Ms. R. Sadhana, Ms. Salu Jacob and my friends who have supported and shared a lot of knowledge and fruitful discussions during my thesis work.

I am extremely thankful to SAIF, IIT Madras for extending their characterization facility towards single crystal XRD analysis, Amrita Institute of Nanoscience and Molecular Medicine, Kochi for the XPS and TEM analysis. I am grateful to Dr. K P Vijayalakshmi, ASD, VSSC, for the computational modelling and analysis support.

I also thank my friends in IIST for their sincere help and support especially to Dr. Manjunath Ganiga and Dr. Neema PM, IIST.

I would like to thank my dear friends and colleagues of PCM Entity, VSSC viz. Ms. Deepthi Thomas, Ms. Bhuvanewari S, Ms. Temina Mary Robert, Dr. Roshith Roshan, Smitha Sukumaran, Dhanya M.S, Dr. Sunitha K and Dr. Deepthi L Sivadas for their constant help and support in every aspect of the experimental works, material characterization and technical discussions. I would like to acknowledge the help rendered by all the staff of the Analytical and Spectroscopy Division (ASD) and Polymers and Special Chemicals Division (PSCD), VSSC for their support at various stages of my research.

I am always thankful to the most respected and lovable teacher, Prof (Dr.) M K Muraleedharan Nair, Former Principal, Govt. Brennen College, Kannur. His continuous motivation, constructive advice, follow up and inspiring suggestions were also greatly acknowledged.

Last but not least, I wish to express my heartfelt gratitude to family members viz. parents, especially my mother, parents-in-law, sister and cousin brother for their much-needed support, patience, understanding, and encouragement in every possible way. And also, my indebtedness towards my husband and my daughter for their continuous moral support and prayers, which uphold me in accomplishing this research work successfully. Their endless love, priceless, perpetual, indispensable help, support and everything made all this possible.

NISHA BALACHANDRAN

## ABSTRACT

The organic-inorganic hybrid perovskite materials emerged as a new class of semiconducting materials with a wide range of applications viz; optoelectronics, photovoltaics, etc. Among the various solution processed semiconductors, organometal halide perovskites represent a remarkable class of materials. Optical gap tunability, efficient charge transport, strong light absorption and favourable emission properties stand as the key features of these novel semiconductors. These properties make them a candidate for developing the new generation of low-cost solar cells and optical emitters. However, the fundamental properties of these materials remain unrevealed, making active discussions among the researchers.

In the thesis work, organic-inorganic perovskite materials are prepared using different strategies. Four different approaches of synthesis and characterization of tin and lead based perovskite were included in the thesis. The applications of the synthesised material were also attempted.

Layered organic-inorganic hybrid materials based on ionic liquid and lead chloride were studied for the first time. In this study, the synthesis, characterization and optical properties of hybrid materials formed from lead chloride ( $\text{PbCl}_2$ )-methylimidazolium chloride (MimCl) and  $\text{PbCl}_2$ -alkyl methylimidazolium chlorides (AmimCl) of varying alkyl chain lengths viz. ethyl ( $\text{C}_2\text{mimCl}$ ), butyl ( $\text{C}_4\text{mimCl}$ ) and hexyl ( $\text{C}_6\text{mimCl}$ ) were evaluated. Complete structural characterisations of the synthesized materials were studied using single crystal X-ray diffraction, Raman spectroscopy, X-ray photoelectron spectroscopy. Apart from 3D structures, the presence of layered 2D structures was evident in all three structures. The interactions were studied using computational analysis and the results were correlated. The materials synthesized were non-hygroscopic and exhibited excellent thermal stability. The AmimCl- $\text{PbCl}_2$  shows absorption in the UV region with the onset extends to the visible range and exhibits good photoluminescence and exciton lifetime.

In the next chapter, organic dyes are introduced into a mesoporous perovskite layer and explored the contribution to light harvesting by co-sensitisation. Co-sensitisation has been investigated by using the bipyridyl based ruthenium dye-N719. These dyes absorb in the orange-red region of the visible spectrum and having a high molar extinction coefficient. Methyl ammonium lead bromide ( $\text{CH}_3\text{NH}_3\text{PbBr}_3$ ) hybrid perovskites are doped with the bipyridyl based Ruthenium dye-N719 were synthesized. Doping with the dye on  $\text{CH}_3\text{NH}_3\text{PbBr}_3$  exhibits a broad absorption peak in the visible region with a shift in the bandgap. The influence of doping on optical properties was studied using microscopic and spectroscopic analytical methodologies.

Tin halide perovskites are evolving as an alternate material to conventional lead based perovskites. The synthesis of methylammonium bimetallic bromide perovskites based on tin and copper ( $\text{MeSn}_{1-x}\text{Cu}_x\text{Br}_{3-y}\text{Cl}_y$ ), where  $x$  and  $y = 0, 1, 2$ , etc. were carried out. Since tin (Sn) being highly sensitive to air, perovskite structure can be self-destroyed and  $\text{Sn}^{2+}$  forms  $\text{Sn}^{4+}$  oxidation state. As the copper is substituted against the tin, there is a tendency to form a 2D perovskite structure rather than a 3D structure. The thermal stability and environmental stability was investigated using Thermogravimetric analysis (TGA) and X-ray Diffraction (XRD), respectively. UV-Vis absorption spectrum exhibits optical absorption over the entire visible spectrum with a band gap of 1.60 eV which is comparable to that of lead based perovskites. Charge carrier lifetime and luminescence behaviour of the materials were determined using time-resolved fluorescence spectroscopy.

Polymeric encapsulants are proven defect passivating agents which render perovskite films robust against harsh environments. Here, we report the new synthesis approach of tin halide perovskite encapsulated by a transparent conducting oligomer, namely polysilsesquioxane (PSQ). The stability of the tin halide perovskite is improved using the modifier. PSQ has good electrical conductivity and HOMO-LUMO energy levels being suited for promoting the hole conductivity of the perovskite materials. The crystal structure, morphology, optical properties and current-voltage characteristics were studied for the PSQ encapsulated perovskite using microscopic, spectroscopic and photovoltaic characterization techniques.

Photovoltaic cells were fabricated under ambient atmosphere (RH: > 60%) over the fluorinated tin oxide (FTO) glass substrate by solution processing method using spin coating technique. All the cells exhibited photovoltaic responses when exposed to sunlight. As the layered  $\text{AmimCl-PbCl}_2$  shows photocurrent in the UV region, these materials exhibit negligible power conversion efficiencies in solar cell devices. Photovoltaic power conversion efficiencies (PCEs) in the range of 4.8 - 6.8 % were observed for the dye-doped methylammonium lead bromide perovskites based active layer. Short-circuit current densities ( $J_{sc}$ ) were in the range of 7-8  $\text{mA}/\text{cm}^2$  with open circuit potential ( $V_{oc}$ )  $\sim 0.96$  V and fill factors (FF) in the range of 60 % under the 1 sun ( $100 \text{ mW}/\text{cm}^2$ ) illumination. The tin and copper mixed perovskites exhibited PCE of  $\sim 2$  % with an  $V_{oc}$  of  $\sim 0.95$  V,  $J_{sc}$  of  $\sim 4.3 \text{ mA}/\text{cm}^2$  and a FF of  $\sim 0.55$ . The oligomer modified methylammonium tin bromide perovskites shows a PCE of  $\sim 2.2\%$  with a  $J_{sc}$  of  $\sim 5.4 \text{ mA}/\text{cm}^2$ ,  $V_{oc}$  of  $\sim 1.0$  V and a FF of  $\sim 40$  % under 1 sun illumination. Compared to the commercial system though  $V_{oc}$  was comparable, the  $J_{sc}$  and the PCE was very low, which is probably due to the increase in resistance at the interface of the layers, defects, and increase in thickness of the layers. Further optimization of the fabrication condition can yield better PCE.

## TABLE OF CONTENTS

DESCRIPTION	PAGE NUMBER
CERTIFICATE	v
DECLARATION	vi
ACKNOWLEDGEMENTS	vii
ABSTRACT	xii
LIST OF FIGURES	xix
LIST OF TABLES	xxvi
ABBREVIATIONS	xxvii
NOTATIONS	xxviii
<b>CHAPTER 1: INTRODUCTION</b>	<b>1</b>
1.1 Introduction to Perovskites	1
1.1.1 Composition of Perovskites	2
1.1.1.1 Metal oxide perovskites	2
1.1.1.2 Metal halide perovskites	2
1.1.2 Interactions in hybrid metal halide perovskites	2
1.1.2.1 Intermolecular interaction	3
1.1.2.2 Interaction between organic molecules and octahedral framework	3
1.2 Hybrid Organic/inorganic Perovskites (HOP): Literature Perspective	4
1.2.1. Factors affecting geometry in metal halide perovskites	5
1.2.2. Lower dimensional Perovskites	8
1.2.3. Stability of Hybrid Perovskites	11
1.2.4. Properties of hybrid perovskites	12
1.2.4.1. Optical properties	12
1.2.4.2. Electrical properties	15
1.2.5. Synthesis strategies of hybrid perovskites	16
1.2.5.1 Solution-processed perovskites	16

1.2.5.2 Template assisted synthesis	20
1.2.5.3 Thermal evaporation method	20
1.2.5.4 Chemical vapor deposition (CVD)	20
1.2.6. Applications of hybrid perovskites	21
1.2.6.1 Perovskite photovoltaics	22
1.2.6.2 LEDs	22
1.2.6.3. Lasers	23
1.2.6.4 Photodetector	23
1.3 Scope and Objectives	24
<b>CHAPTER 2: MATERIALS AND METHODS</b>	25
2.1 Materials	25
2.1.1 Inorganic halides	25
2.1.2 Ionic liquids	25
2.1.3 Organic halides	25
2.1.4 Azo dye sensitizer	25
2.1.5 Polymeric encapsulant	25
2.1.6 Coatings and solvents	25
2.1.7 Solar cell substrates and electron transport layer	26
2.2 Characterisation Methods	26
2.2.1 Fourier transform infrared (FTIR) spectroscopy	26
2.2.2 Raman spectroscopy	26
2.2.3 X-ray Diffraction	26
2.2.4 X-ray photoelectron spectroscopy (XPS)	27
2.2.5 Inductively coupled plasma atomic emission spectroscopy ICP-AES	27
2.2.6 UV-Visible spectroscopy	27
2.2.7 Fluorescence spectroscopy	28
2.2.8 Differential scanning calorimetry (DSC)	28
2.2.9 Thermogravimetric analysis (TGA)	29
2.2.10 Atomic force microscopy (AFM)	29
2.2.11 Field emission scanning electron microscope (FE-SEM)	29

2.2.12 Transmission electron microscopy (TEM)	30
2.2.13 Cyclic voltammetry (CV)	30
2.2.14 Photocurrent measurement	31
2.2.15 Impedance spectroscopy	31
2.2.16 Computational methods	32
<b>CHAPTER 3: IONIC LIQUID BASED HYBRID</b>	<b>33</b>
<b>PEROVSKITES: SYNTHESIS, CHARACTERISATION</b>	
<b>AND EVALUATIONS</b>	
3.1 Introduction	33
3.2. Synthesis of the Hybrid Perovskites	35
3.3. Results and Discussion	35
3.3.1 Structural characterization	36
3.3.1.1 Conformations in the hybrid perovskite	42
3.3.2 Morphological characterisations	47
3.3.3 Optical properties	48
3.3.4 Photoconductivity studies	53
3.3.5 Thermal properties	54
3.4 Conclusions	56
<b>CHAPTER 4: DYE-SENSITISED METHYLAMMONIUM</b>	
<b>LEAD BROMIDE PEROVSKITE: SYNTHESIS,</b>	<b>57</b>
<b>CHARACTERISATION AND EVALUATIONS</b>	
4.1 Introduction	57
4.2 Experimental	58
4.2.1 Materials and Synthesis	58
4.3 RESULTS AND DISCUSSION	60
4.3.1 Structural characterization	60
4.3.2 Optical properties	64
4.3.3 Morphological characterisations	65
4.4 Conclusions	66
<b>CHAPTER 5: ENVIRONMENTALLY STABLE TIN-</b>	<b>69</b>
<b>HALIDE PEROVSKITES: OLIGOMER MEDIATED</b>	

<b>SYNTHESIS AND CHARACTERISATION</b>	
5.1 Introduction	69
5.2 Preparation of PSQ-Perovskite films	70
5.3 Results and discussions	72
5.3.1 Structural characterization	72
5.3.2 Optical characterization	74
5.3.3 Morphological characterization	76
5.3.4 Electrical characterization	77
5.3.5 Ageing studies	78
5.4 Conclusions	79
<b>CHAPTER 6: STABLE, MIXED METAL (Sn-Cu) HALIDE PEROVSKITES</b>	81
6.1 Introduction	81
6.2 Synthesis methods	82
6.3 Result and Discussion	83
6.3.1 Structural characterization	83
6.3.2 Optical characterization	91
6.3.3 Morphological characterization	95
6.3.4 Computational analysis	97
6.3.5 Electrical characterization	98
6.4 Conclusions	99
<b>CHAPTER 7: EVALUATION OF PEROVSKITE BASED SOLAR CELLS</b>	101
7.1 Fabrication of Perovskite Solar Cells	101
7.1.1 Preparation of coating solutions	101
7.1.1.1 TiO <sub>2</sub> blocking layer	101
7.1.1.2 Mesoporous layer	101
7.1.1.3 Perovskite precursor solution	101
7.1.1.4 Hole transport layer (HTM)	102
7.2. Fabrication Steps	102
7.2.1 Masking and etching process	102
7.2.2 Spin coating	103

7.2.3 Sintering of spin coated layers	105
7.2.4 Sputtering to prepare counter electrode	105
7.3 Photovoltaic Evaluation	107
7.3.1 Evaluation of photovoltaic properties of fabricated devices	107
7.3.1.1 N719 sensitised methylammonium lead bromide perovskite solar cells	107
7.3.1.2 Oligomer assisted synthesized of $\text{MASnBr}_3$	109
7.3.1.3 Tin-Copper mixed metal cation based solar Cells	110
7.4 Conclusions	113
<b>CHAPTER 8: CONCLUSIONS AND FUTURE DIRECTIONS</b>	114
8.1 Conclusion	114
8.2 Future Perspectives	115
<b>REFERENCES</b>	117
<b>LIST OF PUBLICATIONS</b>	130
<b>CONFERENCES AND WORKSHOPS</b>	131

## List of Figures

Figure No.	Title	Page No.
1.1	Structure of CaTiO <sub>3</sub> type perovskite. In CaTiO <sub>3</sub> type structures, A cation has +2 oxidation state, B cation has +4 oxidation state and O anion has -2 oxidation state.	1
1.2	Ordering of molecular dipoles in the absence and presence of an external electric field.	3
1.3	Structure of methylammonium lead iodide perovskite	5
1.4	Range of tolerance factors of various stable perovskites structures	6
1.5	The arrangement of anions having coordination number six: 4 anions in the plane, one above (shown) and one below the plane (not shown). The range of stability limit is at $r_{\text{cation}}/r_{\text{anion}} = 0.414 - 0.592$	7
1.6	The t- $\mu$ plot for various combinations of organic and inorganic hybrid perovskite components	8
1.7	Structure of 'A' cation in 2D perovskite	10
1.8	(a) Stacking different layers of 2D perovskite to 3D perovskite (b) quantum well structure of 2D perovskites (Mao, Stoumpos et al. 2018).	11
1.9	Dimensionality variations in metal halide perovskites at molecular levels	9
1.10	Proposed mechanisms for decomposition of perovskites in the presence of water at room temperature	12
1.11	Mechanism of degradation of perovskites in the presence of water and UV	12
1.12	Effect of B site substitution on the band gap of metal halide perovskites	14
1.13	The bandgap tuning of perovskites by halide substitution	15
1.14	Schematic showing synthesis setup for the growth of large CH <sub>3</sub> NH <sub>3</sub> PbI <sub>3</sub> single crystals.	17
1.15	Schematic showing the formation of different types of nanocrystals (CsPbX <sub>3</sub> (X=Cl, Br, I)). The synthesis is done by organic acid and amine ligands at room temperature. Hexanoic acid and octylamine result in spherical quantum dots, oleic acid and dodecylamine leading to nanocubes, acetate acid and dodecylamine for nanorods few-unit-cell-thick nanoplatelets could be formed using oleic acid and octylamine.	18
1.16	Schematic showing hot injection method for preparation of perovskite nanoparticles	20
1.17	Scheme showing the chemical vapour deposition method for hybrid perovskite synthesis.	21
1.18	Potential applications of hybrid organic/inorganic	

	perovskites (HOPs)	21
3.1	Chemical structures of ionic liquids used in this study	35
3.2	Raman spectra of (a) MimCl-PbCl <sub>2</sub> , (b) C <sub>2</sub> mimCl-PbCl <sub>2</sub> , (c) C <sub>4</sub> mimCl-PbCl <sub>2</sub> and (d) C <sub>6</sub> mimCl-PbCl <sub>2</sub> . The A <sub>1g</sub> +B <sub>2g</sub> , B <sub>2g</sub> and B <sub>1g</sub> modes of vibrations are marked in the figure. The label Pb-Cl <sub>b</sub> represents bridging bonds and Pb-Cl <sub>t</sub> represents terminal bonds.	37
3.3	(A) Optical image of Single crystal of C <sub>2</sub> mimCl-PbCl <sub>2</sub> , (B) 2D layered structure of C <sub>2</sub> mimCl-PbCl <sub>2</sub> elucidated from single crystal XRD data	39
3.4	(A) The XRD spectra of various ILs - PbCl <sub>2</sub> systems. The names of the hybrid materials are given as Figure legend. (B) XRD pattern of PbCl <sub>2</sub>	40
3.5	(A) Optical image of a single crystal of C <sub>2</sub> mimCl-PbCl <sub>2</sub> , (B) 2D layered structure of C <sub>2</sub> mimCl-PbCl <sub>2</sub> elucidated from single crystal XRD data	41
3.6	(A) represents the Raman spectra and (B) FTIR spectra showing the peaks corresponds to gauche (g) and trans (t) conformation of C <sub>2</sub> mimCl-PbCl <sub>2</sub> , C <sub>4</sub> mimCl-PbCl <sub>4</sub> and C <sub>6</sub> mimCl-PbCl <sub>6</sub>	43
3.7	Interaction of hexacoordinated PbCl <sub>2</sub> with (A) Mim <sup>+</sup> , (B) C <sub>2</sub> mim <sup>+</sup> , (D) C <sub>4</sub> mim <sup>+</sup> and (E) C <sub>6</sub> mim <sup>+</sup> cations and (C) interaction of pentacoordinated with C <sub>4</sub> mim <sup>+</sup> . These structures of the compounds were elucidated from Density Functional Theory (DFT) method	44
3.8.	(1-4) AFM images, (5-8) : height profile across the line drawn in Fig (1-4), (9-12) is the TEM images and (13–16) is SAED pattern of MimCl-PbCl <sub>2</sub> , C <sub>2</sub> mimCl-PbCl <sub>2</sub> , C <sub>4</sub> mimCl-PbCl <sub>2</sub> and C <sub>6</sub> mimCl-PbCl <sub>2</sub> , respectively	46
3.9	(A) shows UV-visible spectra (a) MimCl, (b) C <sub>2</sub> mimCl, (c) C <sub>4</sub> mimCl (d) C <sub>6</sub> mimCl and lead chloride, respectively. Absorption spectrum of PbCl <sub>2</sub> is given in (B).	47
3.10	(A) shows UV–visible absorption spectra and (B) shows lifetime curves of (a) MimCl- PbCl <sub>2</sub> , (b) C <sub>2</sub> mimCl-PbCl <sub>2</sub> , (c) C <sub>4</sub> mimCl-PbCl <sub>2</sub> and (d) C <sub>6</sub> mimCl-PbCl <sub>2</sub> . The UV–visible absorption spectra of the same ILs-PdCl <sub>2</sub> systems are given as the inset of (B)	49
3.11	(A), (B), (C) and (D) represents cyclic voltammetry curve and (E) energy band diagram of (a) MimCl-PbCl <sub>2</sub> , (b) C <sub>2</sub> mimCl-PbCl <sub>2</sub> , (c) C <sub>4</sub> mimCl-PbCl <sub>2</sub> and (d) C <sub>6</sub> mimCl-PbCl <sub>2</sub> respectively	51
3.12	Dark and light current measured for MimCl- PbCl <sub>2</sub> , C <sub>2</sub> mimCl-PbCl <sub>2</sub> , C <sub>4</sub> mimCl-PbCl <sub>2</sub> and C <sub>6</sub> mimCl-PbCl <sub>2</sub>	52
3.13	(A) shows TGA and (B) shows DSC curves of (a) MimCl-PbCl <sub>2</sub> , (b) C <sub>2</sub> mimCl-PbCl <sub>2</sub> (c) C <sub>4</sub> mimCl-PbCl <sub>2</sub>	53

	and (d) C <sub>6</sub> mimCl-PbCl <sub>2</sub>	
3.14	FTIR spectra of (a) MimCl- PbCl <sub>2</sub> , (b) C <sub>2</sub> mimCl-PbCl <sub>2</sub> , (c) C <sub>4</sub> mimCl-PbCl <sub>2</sub> and (d) C <sub>6</sub> mimCl-PbCl <sub>2</sub> after keeping at ambient conditions for 1 months. Important peaks and the -OH stretching region is marked.	54
4.1	Structure of N 719 dye	58
4.2	FTIR spectra of N719 dye, CH <sub>3</sub> NH <sub>3</sub> PbBr <sub>3</sub> and the dye sensitised CH <sub>3</sub> NH <sub>3</sub> PbBr <sub>3</sub>	59
4.3	(A) XRD pattern of dye, CH <sub>3</sub> NH <sub>3</sub> PbBr <sub>3</sub> and dye sensitised CH <sub>3</sub> NH <sub>3</sub> PbBr <sub>3</sub> , (B) single crystal XRD reflections of dye sensitised CH <sub>3</sub> NH <sub>3</sub> PbBr <sub>3</sub> and (C) Optical image of single crystal of dye sensitised CH <sub>3</sub> NH <sub>3</sub> PbBr <sub>3</sub>	60
4.4	(A) High-resolution XPS spectra showing the 3d orbital of Ru and 4f orbital of Pb	62
4.5	(A) and (B) shows the optimised structure obtained from computational analysis using PM6 level of semi-empirical method and (C) Zoomed region of -OH stretching peak observed in FTIR spectra	63
4.6	(A) UV-visible spectra, (B) Photoluminescence spectra of CH <sub>3</sub> NH <sub>3</sub> PbBr <sub>3</sub> and dye + CH <sub>3</sub> NH <sub>3</sub> PbBr <sub>3</sub> and (C) Energy band diagram of CH <sub>3</sub> NH <sub>3</sub> PbBr <sub>3</sub> and dye + CH <sub>3</sub> NH <sub>3</sub> PbBr <sub>3</sub>	64
4.7	(A) FE-SEM images of CH <sub>3</sub> NH <sub>3</sub> PbBr <sub>3</sub> and dye + CH <sub>3</sub> NH <sub>3</sub> PbBr <sub>3</sub>	65
4.8	(A), (C) and (E) are the HR-TEM Images and (B), (D) and (F) shows the SAED patterns of CH <sub>3</sub> NH <sub>3</sub> PbBr <sub>3</sub> , N719 dye+ CH <sub>3</sub> NH <sub>3</sub> PbBr <sub>3</sub> and N719 dye respectively	66
5.1	Scheme showing the synthetic route of polysilsesquioxanes (PSQ)	71
5.2	FTIR spectra of PSQ, PSQ+CH <sub>3</sub> NH <sub>3</sub> SnBr <sub>3</sub> and the CH <sub>3</sub> NH <sub>3</sub> SnBr <sub>3</sub> . The important features are marked.	73
5.3	(A) XRD pattern of the PSQ, CH <sub>3</sub> NH <sub>3</sub> SnBr <sub>3</sub> and PSQ+CH <sub>3</sub> NH <sub>3</sub> SnBr <sub>3</sub> . (B) XPS survey scan spectrum. (C) the deconvoluted spectrum of Sn 3d peak of CH <sub>3</sub> NH <sub>3</sub> SnBr <sub>3</sub> and (D) deconvoluted spectrum of Sn 3d peak of PSQ + CH <sub>3</sub> NH <sub>3</sub> SnBr <sub>3</sub> . Note that in (C), the deconvolution did not result in any peak split.	74
5.4	The transmittance (%) of the PSQ film in the UV-Visible region. <i>Insets</i> : glass slide coated with (A) PSQ and (B) PAQ+ CH <sub>3</sub> NH <sub>3</sub> SnBr <sub>3</sub>	75
5.5	(A) UV-visible absorption spectra (B) Photoluminescence spectra of the PSQ, CH <sub>3</sub> NH <sub>3</sub> SnBr <sub>3</sub> and PSQ+CH <sub>3</sub> NH <sub>3</sub> SnBr <sub>3</sub> .	76
5.6	(A) The AFM images of PSQ and (B) PSQ+CH <sub>3</sub> NH <sub>3</sub> SnBr <sub>3</sub> . The height profile of a line drawn	76

	in (B) is shown as (C)	
5.7	FE-SEM images of (A) PSQ, (B) $\text{CH}_3\text{NH}_3\text{SnBr}_3$ and (c) PSQ+ $\text{CH}_3\text{NH}_3\text{SnBr}_3$ films. (D) EDS spectrum of PSQ, (E) $\text{CH}_3\text{NH}_3\text{SnBr}_3$ and (F) PSQ + $\text{CH}_3\text{NH}_3\text{SnBr}_3$	77
5.8	(A) Optimised structure of the PSQ using Gaussian 09 software, (B) Cyclic voltammogram of PSQ and (C) Energy bands diagram of the materials employed for the preparation of the cell.	78
5.9	(A) UV-Visible spectra, (B) FTIR spectra and (C) XRD patterns of $\text{CH}_3\text{NH}_3\text{SnBr}_3$ and PSQ + $\text{CH}_3\text{NH}_3\text{SnBr}_3$ .	79
6.1	The XRD pattern of perovskite (A) and precursor materials (B) used for synthesing various perovskites. The name of perovskite and the precursor is given in each spectrum. The * peaks in the middle pane of (A) depict the presence of layered structure	84
6.2	FTIR spectra of perovskites (labelled in each spectrum) and MABr spectrum is given in the bottom pane for comparison. The position of $-\text{OH}_{str}$ , $-\text{NH}_3^+_{str}$ and $-\text{NH}_3^+_{bend}$ vibrations is marked with dotted lines	86
6.3	High-resolution XPS spectra of Sn 3d peaks of (A) $\text{Sn}_1:\text{Cu}_0$ (B) $\text{Sn}_{0.5}\text{Cu}_{0.5}$ and in (C), the Cu 2p peaks are shown of $\text{Cu } ^3\text{P}_{3/2}$	88
6.4	Different regions of the UPS spectra of the perovskite materials (A- $\text{Sn}_1:\text{Cu}_0$ , B- $\text{Sn}_{0.5}:\text{Cu}_{0.5}$ and C- $\text{Sn}_0:\text{Cu}_1$ ).	89
6.5	(A) Thermogram of $\text{Sn}_1:\text{Cu}_0$ , $\text{Sn}_{0.5}:\text{Cu}_{0.5}$ and $\text{Sn}_0:\text{Cu}_1$ . The dotted line represents the onset of weight loss for $\text{Sn}_{0.5}:\text{Cu}_{0.5}$ , (B) FTIR spectrum and (C) UV-visible spectrum of $\text{Sn}_{0.5}:\text{Cu}_{0.5}$ material.	90
6.6	(A) UV-visible absorption spectra and (B) Energy band diagram of the perovskites	92
6.7	(A) Photoluminescence spectra of the perovskite materials and (B) life time measurements of the perovskites	94
6.8	(A)-(C) FE-SEM images of $\text{Sn}_1:\text{Cu}_0$ , $\text{Sn}_{0.5}:\text{Cu}_{0.5}$ and $\text{Sn}_0:\text{Cu}_1$ , (D)-(F) TEM images of $\text{Sn}_1:\text{Cu}_0$ , $\text{Sn}_{0.5}:\text{Cu}_{0.5}$ and $\text{Sn}_0:\text{Cu}_1$ and (G)-(I) SAED pattern of $\text{Sn}_1:\text{Cu}_0$ , $\text{Sn}_{0.5}:\text{Cu}_{0.5}$ and $\text{Sn}_0:\text{Cu}_1$	96
6.9	Optimised structures (A) $\text{Sn}_1:\text{Cu}_0$ , (B) $\text{Sn}_{0.5}:\text{Cu}_{0.5}$ and (C) $\text{Sn}_0:\text{Cu}_1$	97
6.10	A, B and C shows the band structure of the perovskites calculated using DFT by Vienna Ab initio Simulation Package (VASP)	98
6.11	Nyquist plot of $\text{Sn}_{0.5}:\text{Cu}_{0.5}$ . <i>Inset</i> : equivalent circuit diagram	99
7.1	(A) Representation of patterned FTO plate after	102

	masking and (B) the photograph is showing the masked substrate (using Kapton tape).	
7.2	(A) Spreading of Zn powder on FTO glass and dropping of HCl solution on it, (B) Evolution of H <sub>2</sub> gas along with the etched FTO (C) the etched FTO glass after cleaning	103
7.3	Spin coating machine	103
7.4	Figure 7.4. Four steps involved spin coating of material (1) A drop of the sample solution added over the substrate, (2) substrate is rotated at very high speed (several thousand rpm) and a majority of solution flew off, (3) Solvent gets dried by air flow leaving a plasticised film and (4) shows the deposited molecules of the sample on the surface of the substrate	104
7.5	(A) Aluminum foil masking (B) the cells after sputtering	106
7.6	The photograph of the cells after attaching the connection leg	106
7.7	(A) Solar simulator used for the study and (B) shows the solar cells connected to measuring aperture	107
7.8	(A) schematic of device architecture (B) a photograph of the solar cell after fabrication (C) J-V curve of dye+MAPbBr <sub>3</sub> and MAPbBr <sub>3</sub> alone	108
7.9	(A) Photocurrent observed for FTO/CH <sub>3</sub> NH <sub>3</sub> SnBr <sub>3</sub> /PSQ/ Au, (B) J-V curve of FTO/TiO <sub>2</sub> /CH <sub>3</sub> NH <sub>3</sub> SnBr <sub>3</sub> /HTM/Au under 1 Sun illumination and inset of (C) J-V curve of FTO/TiO <sub>2</sub> /CH <sub>3</sub> NH <sub>3</sub> SnBr <sub>3</sub> +PSQ/Au under the same conditions.	109
7.10	(A), (B) and (C) are AFM images of Sn <sub>0.5</sub> :Cu <sub>0.5</sub> layer; (D) FE-SEM image of Sn <sub>0.5</sub> :Cu <sub>0.5</sub> over FTO substrate and (E) shows the cross-sectional image of different layers of coating of the solar cell.	111
7.11	J-V curve of the cell under 1 Sun illumination. The device was fabricated using Sn <sub>0.5</sub> :Cu <sub>0.5</sub> as active layer.	112

## LIST OF TABLES

TABLE	TITLE	PAGE NUMBER
3.1	Chemical composition of the synthesised perovskites obtained from ICP-AES analysis.	35
3.2	Crystal structure data derived from single crystal analysis	41
3.3	HOMO and LUMO levels of the hybrid perovskite materials	50
4.1	Unit cell parameters derived from single crystal XRD reflection of N 719 dye + CH <sub>3</sub> NH <sub>3</sub> PbBr <sub>3</sub>	61
4.2	Proportion of CH <sub>3</sub> NH <sub>3</sub> Br: SnBr <sub>2</sub> : CuCl <sub>2</sub> used for the synthesis	82
6.1	Calculation of stability factors of 3D perovskites	84
6.2	Diffraction angle and the calculated d-spacing values from XRD data. Cu K $\alpha$ radiation was used at a scan rate of 4.8°/min. In right-side columns, the diffraction peaks of Sn <sub>0.5</sub> :Cu <sub>0.5</sub> are segregated for 2D and 3D.	85
6.3	Valence band maxima obtained from UPS spectra in Fig 6.4	89
6.4	Lifetime components of perovskites, calculated from the lifetime spectra	95
6.5	The concentration of CuCl <sub>2</sub> (x) and SnBr <sub>2</sub> (1-x) was calculated using the values of copper and tin obtained from SEM-EDX.	96
7.1	Optimised spin coating parameters for different layers	106
7.2	Sintering temperature for various layer	106
7.3	Photovoltaic parameters under 1 Sun illumination	109
7.4	Photovoltaic parameter of CH <sub>3</sub> NH <sub>3</sub> SnBr <sub>3</sub> /PSQ solar cell under 1 Sun illumination	111
7.5	Photovoltaic parameters of tin-copper mixed metal cation based solar cells under 1 Sun illumination	113

## ABBREVIATIONS

1D	One dimensional
2D	Two dimensional
3D	Three dimensional
AFM	Atomic force microscopy
AmimCl	Alkylmethyl imidazolium chloride
C <sub>2</sub> mimCl	1-ethyl-3-methylimidazolium chloride
C <sub>4</sub> mimCl	1-butyl-3-methylimidazolium chloride
C <sub>6</sub> mimCl	1-hexyl-3-methylimidazolium chloride
CaTiO <sub>3</sub>	Calcium titanate
CH <sub>3</sub> NH <sub>2</sub>	Methyl amine
CH <sub>3</sub> NH <sub>3</sub> PbI <sub>3</sub>	Methylammonium lead iodide
CH <sub>3</sub> NH <sub>3</sub> PbX <sub>3</sub>	Methylammonium lead halide
CsPbI <sub>3</sub>	Cesium lead iodide
CuCl <sub>2</sub>	Copper (II) chloride
CV	Cyclic voltammetry
CVD	Chemical Vapor Deposition
DFT	Density Functional Theory
DMF	N,Ndimethylformamide
DMSO	Dimethylsulfoxide
DSC	Differential scanning calorimetry
EQE	External quantum efficiency
FAPbI <sub>3</sub>	Formamidinium lead iodide
FE-SEM	Field emission scanning electron microscope
FTIR	Fourier transform infrared spectroscopy
FTO	Fluorine-doped tin oxide
GBL	$\gamma$ -butyrolactone
Ge	Germanium
HI	Hydro iodic acid
HOMO	Highest Occupied Molecular Orbital
HOPs	Hybrid organic/inorganic perovskites
ICP-AES	Inductively coupled plasma atomic

	emission spectroscopy
LARP	Ligand-assisted reprecipitation
LEDs	Light-emitting diodes
LUMO	Lowest Unoccupied Molecular Orbital
MimCl	Methylimidazoliumchloride
MQW	Multiple-quantum-well
N719 dye	di-tetrabutylammonium cis-bis(isothiocyanato)bis(2,2-bipyridyl-4,4-dicarboxylato)ruthenium(II)
ODE	Octadecene
PAW	Projector Augmented Wave
PbBr <sub>2</sub>	Lead (II) bromide
PbCl <sub>2</sub>	Lead (II) chloride
PbI <sub>2</sub>	Lead iodide
PSPD	Position Sensitive Photo-Detector
PSQ	Polysilsesquioxanes
SAED	Selected area electron diffraction
Sn	Tin
SnBr <sub>2</sub>	Tin (II) bromide
(Me) <sub>4</sub> N <sup>+</sup>	Tetramethylammonium
TCSPC	Time-correlated single-photon counting
TEM	Transmission electron microscopy
TGA	Thermogravimetric analysis
TiO <sub>2</sub>	Titanium dioxide
UV	Ultra-violet
VASP	Vienna ab initio simulation package
XPS	X-ray photoelectron spectroscopy
XRD	X-ray Diffraction

## NOTATIONS

$t$	Goldschmidt tolerance factor
$\mu$	Octahedral factor
$\theta$	Angle of diffraction
$\lambda$	Wavelength (nm)
$\tau$	Lifetime
eV	Electron volt
cm <sup>2</sup>	Area
hf	The thickness of the coating
$\omega$	Angular velocity
rpm	Spin speed
sec	Spin duration
$\mu\text{l/spin}$	Volume of solution
V/s	scan rate
$V_{oc}$	Voltage (V)
$J_{sc}$	Current, (mA/cm <sup>2</sup> )
PCE (%)	Power conversion efficiency



# CHAPTER 1

## INTRODUCTION

### 1.1 Introduction to Perovskites

Perovskites represent an exciting class of materials for physicists, chemists and material scientists. Based on their structure and chemical composition, perovskites exhibit semiconducting nature, superconductivity, magnetoresistance, spintronics and catalytic properties (Murphy, Sunshine et al. 1987; Bibes and Barthelemy 2007; Hsiao, Wu et al. 2015; Ahmadi, Wu et al. 2017).

The term ‘perovskite’ is named after the Russian mineralogist Lev Perovski. The first of its kind,  $\text{CaTiO}_3$ , was first discovered in the Ural Mountains, of Russia, by Gustav Rose in 1839. The compounds having crystal structures similar to  $\text{CaTiO}_3$  have been classified into the family of perovskites. Presently, perovskite refers to an extensive family of compounds that possess the general formula  $\text{ABX}_3$  where ‘A’ and ‘B’ are cations and ‘X’ is generally an oxide anion (Ramadass 1978; Bhalla, Guo et al. 2000). The representation of a perovskite lattice is given in Figure 1.1. The B cations occupy corners of the cube and at face centres, X anions are present. The centre of the cube is occupied by a larger ‘A’ cation (Smith and Welch 1960).

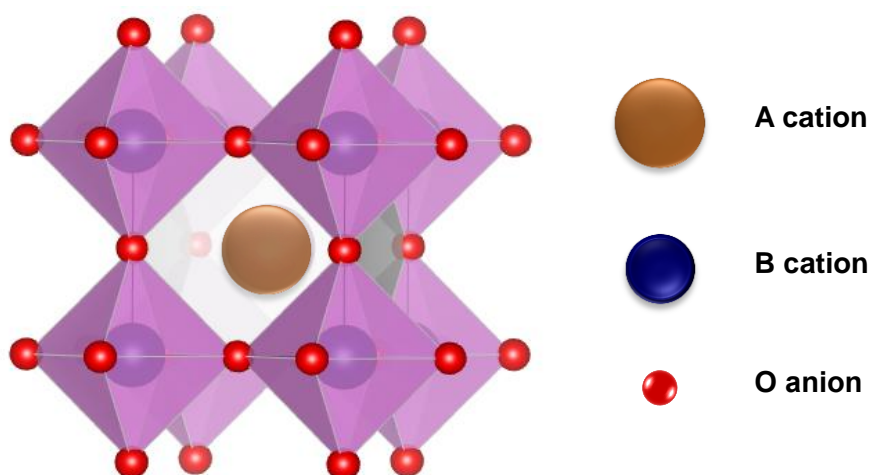


Figure 1.1. Structure of  $\text{CaTiO}_3$  type perovskite. In  $\text{CaTiO}_3$  type structures, A cation has +2 oxidation state, B cation has +4 oxidation state and O anion has -2 oxidation state.

## **1.1.1 Composition of Perovskites**

Based on their constituents, perovskites are classified into two: (i) metal oxide perovskites and (ii) metal halide perovskites.

### **1.1.1.1 Metal oxide perovskites**

Metal oxide perovskites having the general formula  $ABX_3$  can be formed using different I, II, III and IV group elements. The anions in the perovskites can vary as oxyhalides, oxynitrides, etc. and the valency of the two metal cations together is equal to six, maintaining the neutrality of the compound. Double perovskites are another class of metal oxide perovskites having the general formula,  $A_2(BB')O_6$ , where cation 'A' is usually based on an alkali-earth metal and B and B' are transition metals.

### **1.1.1.2 Metal halide perovskites**

Metal halide perovskites are also neutral compounds having the general formula  $ABX_3$ , where the cations A & B together exhibit a valency of three and the anion, X is univalent. The most studied metal halide perovskites are hybrid organic-inorganic perovskites. Here, the monovalent metal cation 'A' is substituted by an organic cation with an appropriate size to fit into the octahedral inorganic cage to form a 3-dimensional (3D) network structure. However, when the size of the organic cation is too large for the octahedral cage, the structure formed will be of lower dimensions such as two dimensional (2D) or one dimensional(1D).

## **1.1.2. Interactions in hybrid metal halide perovskites**

Both ionic and covalent interactions exist in metal halide perovskite systems. The major framework in the metal halide perovskites exists as an octahedral, 3D network. In the lead (Pb) based halide perovskites,  $sp^3d^2$  hybridization prevails, involving  $6s^2 6p^0 5d^0$  orbitals of Pb and  $5p^6$  orbital of iodide ion. The 5p orbital of iodine forms the upper valence band and 6s and 6p orbitals of Pb form the conduction band. (Rao, Cheetham et al. 2008).

### 1.1.2.1 Intermolecular interaction

The inorganic  $BX_6^-$  networks which surround the organic cation 'A' is highly polarizable and can cause variety of electrical behaviors such as paraelectric, ferroelectric, super paraelectric and antiferroelectric as shown in Figure 1.2. The organic cations can move inside the void surrounded by the  $BX_6^-$  networks.

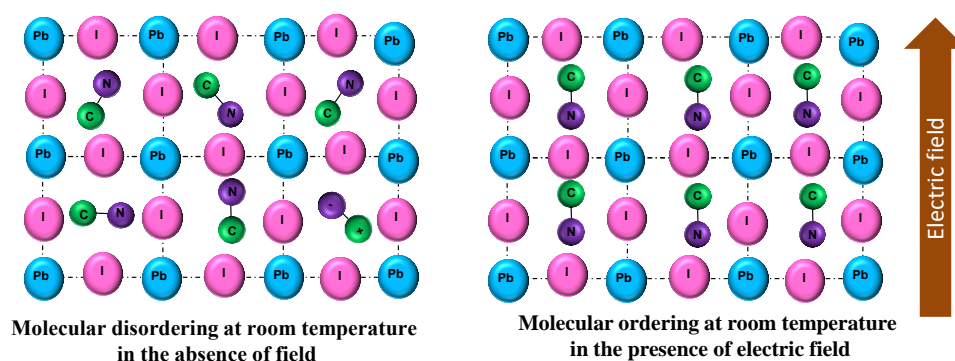


Figure 1.2 Ordering of molecular dipoles in the absence and presence of an external electric field.

### 1.1.2.2 Interaction between organic molecules and octahedral framework

The interaction between the organic cation and inorganic framework is electrostatic. Strong electrostatic potential holds the organic molecule at its lattice site in the inorganic frameworks, which can get polarized. Therefore, charge-dipole interaction occurs between the organic dipole and the inorganic framework, dictated by molecular orientation. The dipolar molecules polarize  $I^-$  ions in the framework leading to induced-dipole interactions (Debye forces) that can direct molecular orientations and deformation of the inorganic framework. The polarization of lattice has two advantageous features related to the internal electric field: (i) enhanced charge separation and improved carrier lifetime (ii) open circuit voltages above the bandgap of the material. The organic cations present in the metal halide perovskites are polar and their polarization depends upon their geometry. The permanent electrical dipole of most common organic cations-

methylammonium is 2.29 D and formamidinium is 0.21 D. The dipole moment can be varied by replacing the organic cations with electron withdrawing groups like mono, di or tri fluoro derivatives of methylammonium which is reported to increase the dipole moment to 5.35, 6.08, and 6.58 D respectively (Frost, Butler et al. 2014). When kept in an external magnetic field, these permanent dipoles interact. The dipolar interactions for the stationary molecules in voids tail off as  $1/r^3$ , while in rotating molecules, it reaches at  $1/r^6$ . Ammonium cation incorporated in the pseudo-cubic lead halide perovskites exhibits zero dipole due to its spherical structure with a small (0.3 KJ/mol) rotational barrier. Therefore, ammonium ion (and caesium ion ( $\text{Cs}^+$ )) rotate inside the void and do not interact with nearby dipoles. Other organic cations having molecular dipoles with higher rotational barriers exhibit higher interaction with nearby dipoles.

In the methylammonium cations, the terminal amine of organic cation interacts with halides in the inorganic anion layers through hydrogen bonds. Adjacent carbon chains of the organic cations are bound together by van der Waals force.

## **1.2 Hybrid Organic/inorganic Perovskites (HOP): Literature Perspective**

Hybrid organic/inorganic perovskites (HOPs) are semiconductors having the general formula  $\text{ABX}_3$ , where A is an organic cation, B is a metal cation and X is halide anion. A typical structure is shown in Figure 1.3. The methylammonium lead halide perovskite  $\text{CH}_3\text{NH}_3\text{PbX}_3$  ( $\text{X}=\text{Cl}, \text{Br}, \text{I}$ ) was first reported by Weber in 1970. These hybrid perovskites have recently attracted significant attention among scientists due to their unique combination of low-cost, good processability and highly tunable properties (Brenner 2016; Sutherland and Sargent 2016; Yuan, Li et al. 2017). Characteristic features of HOPs, crystal structure and geometry and properties that make them suitable for optoelectronic and photovoltaic applications are described in the forthcoming sections.

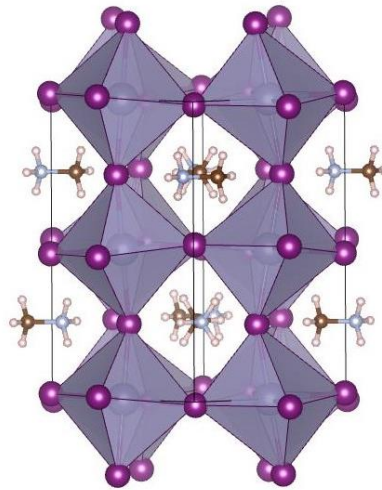


Figure 1.3. Structure of methylammonium lead iodide perovskite (Stoumpos, Malliakas et al. 2013).

### 1.2.1. Factors affecting geometry in metal halide perovskites

The geometrical distortion can significantly influence the properties of the perovskites. Ideally, cubic geometry is exhibited by the perovskites. The structural distortions from the cubic form are mainly governed by the size effect and the Jahn Teller effect.

#### (i) Size effect

Perovskite structures consist of a cubic array of corner-sharing  $BX_6$  octahedral units, in which ‘A’ cations are located within the cuboctahedral cavities. The most common and successfully used method to predict the stability and distortion of perovskite crystal geometries is the Goldschmidt tolerance factor (t). (Travis, Glover et al. 2016).

$$t = \frac{r_A + r_X}{\sqrt{2} (r_B + r_X)}$$

Ionic radii of cations, ‘A’ and ‘B’ and anion, ‘X’ are  $r_A$ ,  $r_B$ ,  $r_X$ , respectively. Generally,  $r_A > r_B$  in the perovskite crystal structure (Shannon 1976). The tolerance factor  $t=1$  indicates the ideal cubic structure. The tolerance factor of the common perovskite structures will fall in the range of 0.8 – 1 and this criterion is satisfied by almost all the inorganic perovskites containing oxide and fluoride anions. However, the hybrid perovskites are not fully satisfied due to geometrical

constraints that arise due to the larger size of the anions (Travis, Glover et al. 2016). Distortions from the cubic structure can also arise due to the size mismatch of the cations and anion, which can result in lower-dimensional perovskite structures and non-perovskite structures as well. Thus, when the cation ‘A’ is replaced by large organic cations that cannot fit in the interspace between the  $[BX_6]^{4-}$  octahedron, the network is forced to form a 2D structure. Tilting of  $BX_6$  octahedra will result in the lowering of ‘t’ value. When the size of the ‘A’ cation is large enough to occupy the octahedral voids, ‘t’ approaches 1. On lowering the dimensionality and decreasing the value of ‘t’ to less than 0.8, the possibility of forming non-perovskite structures increases. (Figure 1.4).

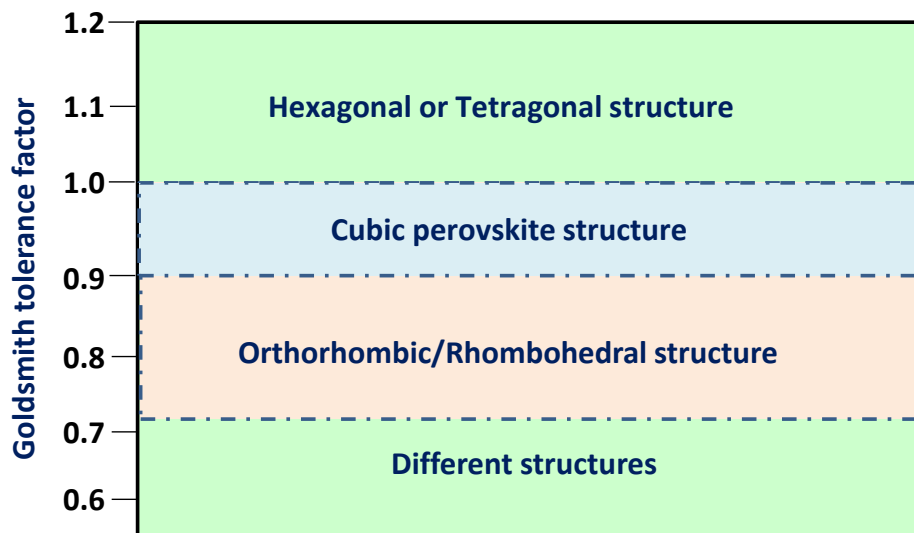


Figure 1.4. Range of tolerance factors of various stable perovskite structures

Another factor representing the stability of the crystal structure is the octahedral factor ‘ $\mu$ ’ (Ju, Dai et al. 2017). The radius of the octahedral cavity formed within the six close-packed rigid spheres is calculated as,

$$r_{hole} = 0.414r$$

As per the radius ratio rule, the crystal is more stable for coordination number six when the radius ratio  $r_B$  to  $r_X$  is greater than or equal to 0.414. Alternately, for ‘ $\mu$ ’ value smaller than 0.414, ‘B’ site cations will not touch the six X-site anions, leading to lower coordination number and crystal structure

instability. Figure 1.5 shows the arrangements of cations and anions with coordination number six. Octahedral geometry is more stable for a ‘ $\mu$ ’ slightly greater than 0.414 since the B-site cation can still maintain contact with the six X-site anions. However, the X-site anions are far from each other so that their mutual repulsion is reduced and the ‘ $\mu$ ’ value reaches 0.592. Therefore, to stabilize the  $[BX_6]$  octahedra, it requires that  $0.414 \leq \mu < 0.592$ .

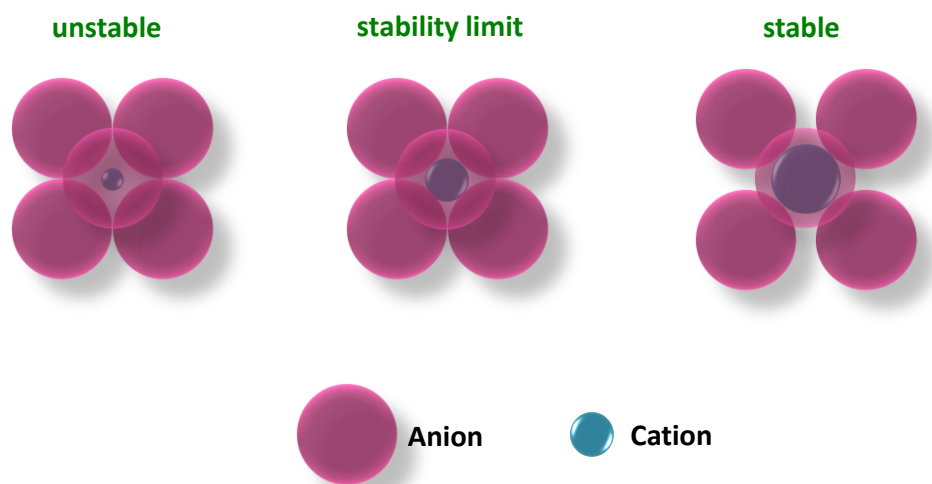


Figure. 1.5 The arrangement of anions having coordination number six: 4 anions in the plane, one above (shown) and one below the plane (not shown). The range of stability limit is at  $r_{\text{cation}}/r_{\text{anion}} = 0.414 - 0.592$

For halide perovskites,  $t$ - $\mu$  plot easily describes the stability of perovskites, as demonstrated for the  $ABX_3$ -type compounds by Travis et al. Figure 1.6 shows the variation in  $t$ - $\mu$  behaviour of Pb and Sn metal halide perovskites. To achieve a ‘ $t$ ’ close to 1, a very large A-site cation is needed for given B-site and X-site ions. Cs is such an element in the periodic table. However, it is still not large enough to hold the stable cubic iodide perovskite structure, so it must be replaced with a still larger monovalent molecule to stabilize the structure. This explains why methylammonium lead iodide ( $\text{MAPbI}_3$ ) and formamidinium lead iodide ( $\text{FAPbI}_3$ ) are more stable than  $\text{CsPbI}_3$ .

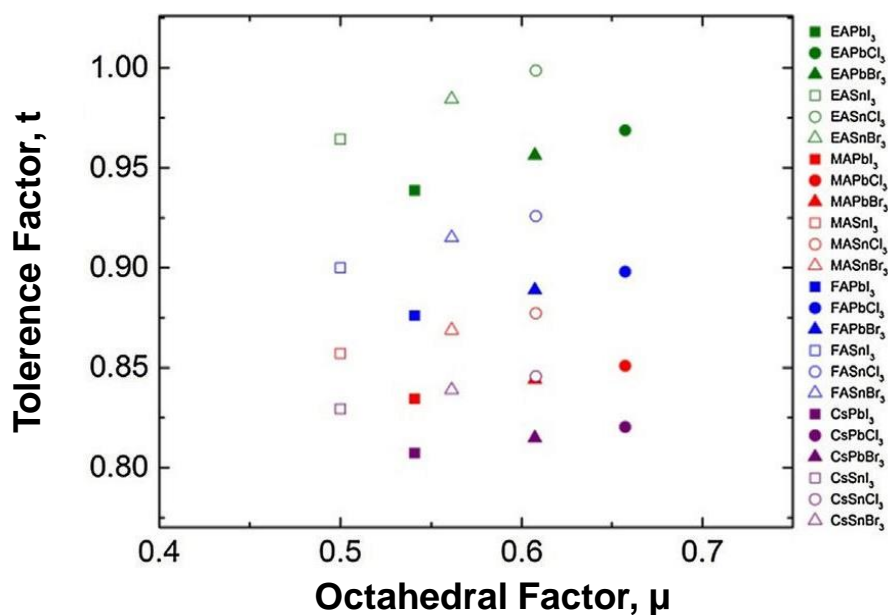


Figure 1.6 The  $t$ - $\mu$  plot for various combinations of organic and inorganic hybrid perovskite components (Chen and De Marco 2015)

(ii) *Jahn-Teller Effect*

The octahedral geometry of the perovskite framework can be elongated or compressed due to Jahn-Teller distortion of  $z$  ligand bonds. (Carpenter and Howard 2009). The molecules having degenerate electronic states distort their octahedron to remove the degeneracy, resulting in lower symmetry. The perovskites with ‘B’ atoms having orbitals with  $d^1$ ,  $d^2$ ,  $d^4$ ,  $d^5$ ,  $d^7$ ,  $d^9$  electronic configurations exhibit Jahn-Teller distortion. For example, perovskites of  $\text{Cu}^{+2}$  and  $\text{Mn}^{+3}$  forms tetragonal frameworks by elongating bonds (Tan, Kennedy et al. 2012).

### 1.2.2 Lower dimensional perovskites

By varying the size of cation ‘A’, the shape and dimensionality of metal halide perovskites can be tuned to 3D structures, 2D sheets, 1D nanorods and 0D quantum dots (Sun, Yuan et al. 2016). Figure 1.7 shows the dimensionality variation. Zero dimensional  $\text{MAPbBr}_3$  quantum dots were synthesized using organic capping ligands having long alkyl chains (Schmidt, Pertegás et al. 2014).

Nanoplatelets with 2D perovskite structure and exhibiting quantum confinement effects were reported (Tyagi, Arveson et al. 2015). The layered 2D halide perovskites overcome the environmental stability issues encountered by the 3D perovskites to a great extent.

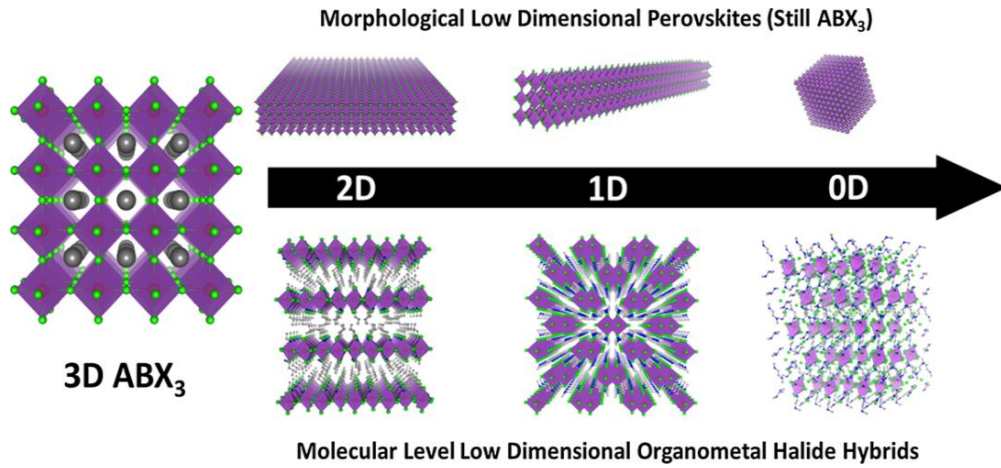


Figure 1.7. Dimensionality variations in metal-halide perovskites at molecular levels (Mao, Stoumpos et al. 2018; Zhou, Lin et al. 2019)

When the size of the cation ‘A’ is very large so that it cannot fit in the interspace between the  $[BX_6]^{4-}$  octahedron, the network is forced to form lower dimensional structures having the general formula  $(A')_2(A)_{y-1}BnX_{3y+1}$ . Where  $y$  represents the number of monolayer sheets of metal halide in between the organic layers and ‘A’ stands for the larger organic cation. From the formula, the structures are derived as  $y = 1$  for 2D structure;  $y = 2-5$  for quasi 2D structure and  $y = \infty$  for standard 3D structure (Gao, Zhang et al. 2019). When the size of the organic cation exceeds the critical size, it results in a structural transition from 3D to 2D (Tian, Zhang et al. 2020). The most commonly used organic cations are listed in Figure 1.8. When the 3D perovskites split across the lattice along  $\langle 001 \rangle$  and  $\langle 110 \rangle$  planes, layered perovskite structures called Ruddlesden–Popper perovskites are formed.

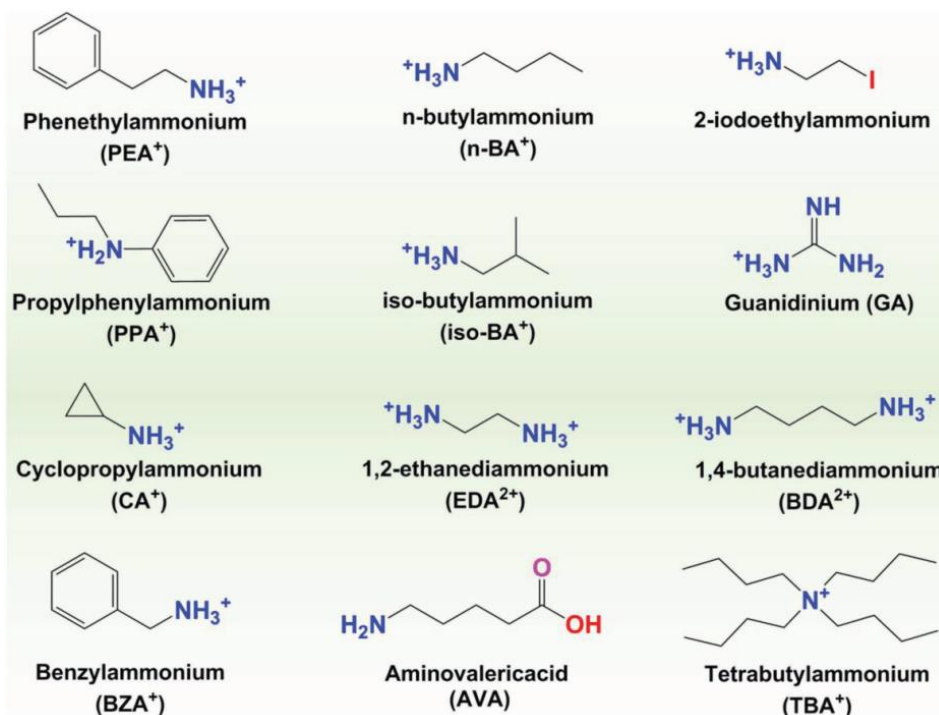


Figure 1.8. Structure of 'A' cation in 2D perovskite

The attractive advantage of layered 2D perovskites over 3D perovskites is their thermal and environmental stability. The larger cations hinder internal ionic motion and decrease the hydrophilic character through the organic moieties, improving stability. In 2D hybrid halide perovskites, the organic cations act as insulating barriers that confine the charge carriers in two dimensions. The specific arrangement of alternating organic-inorganic layers generates a crystallographically ordered 2D multiple-quantum-well (MQW) electronic structure. Due to the high dielectric contrast provided by the 2D MQW electronic structure, the perovskite materials generate huge electron-hole binding energies. So the excitons are more stable at ambient temperatures. The multitude of properties exhibited by the MQW structures makes the 2D halide MQWs a remarkable discovery in the area of optoelectronic applications. Figure 1.9. shows the stacking of different layers of 2D perovskites to 3D perovskites and the quantum well structure of 2D perovskites

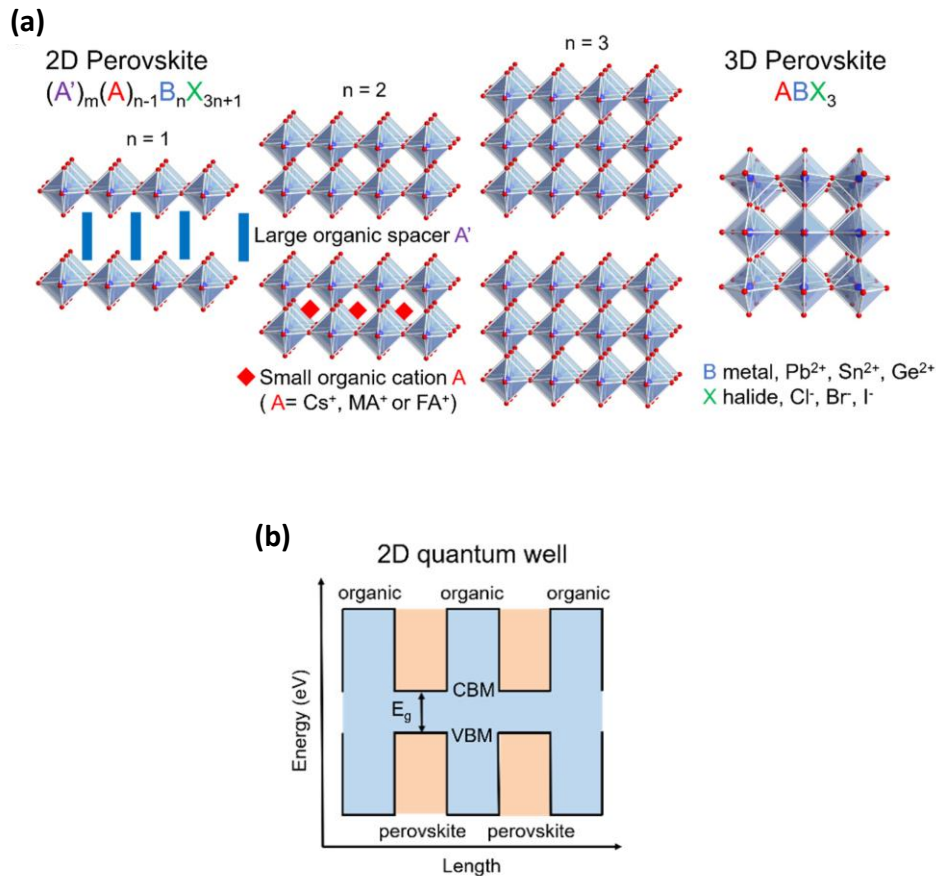


Figure 1.9. (a) Stacking different layers of 2D perovskite to 3D perovskite (b) quantum well structure of 2D perovskites (Mao, Stoumpos et al. 2018).

### 1.2.3 Stability of Hybrid Perovskites

The poor stability of hybrid metal halide perovskites is a major concern in solid state devices. Atmospheric moisture, oxygen, temperature and UV radiation affect their stability. E.g.:  $\text{CH}_3\text{NH}_3\text{PbI}_3$  is highly sensitive to water and gets hydrolyzed in moisture (Niu, Guo et al. 2015). A reported mechanism of decomposition of perovskites in the presence of water is shown in Figure 1.10. The decomposition of hybrid metal halide perovskites occurs in the presence of moisture by a simple acid-base reaction. Water molecule acts as a Lewis base and reacts with the hybrid metal halide perovskite, methylammonium lead bromide ( $\text{CH}_3\text{NH}_3\text{PbI}_3$ ), accepting one proton from the ammonium ion and converts the perovskites into an intermediate compound  $[(\text{CH}_3\text{NH}_3^+)_{n-1}(\text{CH}_3\text{NH}_2)\text{PbI}_3] [\text{H}_3\text{O}^+]$ . The intermediate is then converted to HI,  $\text{CH}_3\text{NH}_2$ , and finally into  $\text{PbI}_2$ . The

$\text{CH}_3\text{NH}_3\text{PbI}_3$  starts to decompose from a humidity of 55%, with a consistent change in colour from dark brown to yellow. The decomposition of metal halide perovskites become rapid in the presence of light. Only a single water molecule is sufficient to degrade the perovskites and dissolve the HI and  $\text{CH}_3\text{NH}_2$  by-products. Based on this proposed mechanism, it is clear that perovskites formed from aprotic organic cations like tetramethylammonium,  $(\text{Me})_4\text{N}^+$ , may be chemically more stable. (Frost, Butler et al. 2014)

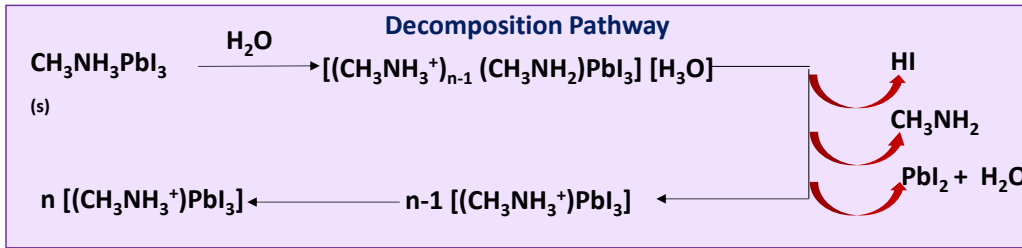


Figure 1.10. Proposed mechanism for decomposition of perovskites in the presence of water at room temperature (Huang, Tan et al. 2017).

A mechanism for the degradation of perovskites in the presence of moisture, oxygen and UV radiation is also reported (see Figure 1.11). (Shirayama, Kato et al. 2016). Here, it is observed that the 2D perovskite reported more resistance to moisture than their 3D perovskites (Wang, Ganose et al. 2019).

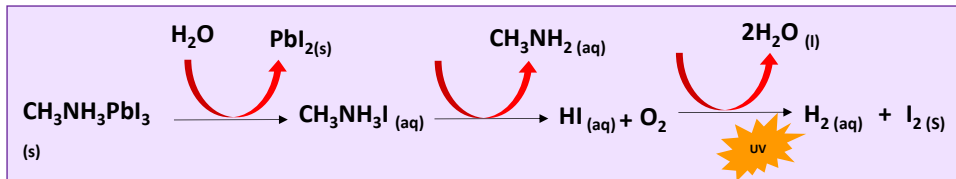


Figure 1.11. Mechanism of degradation of perovskites in the presence of water and UV

## 1.2.4. Properties of hybrid perovskites

### 1.2.4.1 Optical properties

#### *Bandgap*

The primary factor that decides the optical properties of a material is its bandgap. 3D perovskites exhibit strong absorption in the visible region with high

absorption coefficient. The bandgap of perovskites can be tuned by tailoring the geometry employing different A, B and X components. For example, in the case of methylammonium cation, the bandgap is 1.55 eV, but when it is substituted by ammonium cation, a decrease of 0.3 eV was observed. (Frost, Butler et al. 2014). Temperature also plays a significant role in deciding the bandgap of hybrid perovskites. The bandgap of  $\text{CH}_3\text{NH}_3\text{PbI}_3$  decreases from 1.61 eV to 1.55 eV on lowering the temperature from 300 K to 150 K. (Yamada, Nakamura et al. 2014)

The substitution of 'A' cations does not directly influence the electronic structure of organic-inorganic perovskites, but can alter their crystal geometry. (Filip, Eperon et al. 2014) Cations smaller than the methylammonium can lead to geometric deformations leading to a lower bandgap. (Ju, Dai et al. 2017), (Ma, Imran et al. 2018). A widely used 'A' cation is formamidinium (FA). It is reported that this asymmetric molecular ion undergoes geometry distortion, resulting in a lower bandgap. (Zhou, Pang et al. 2016) A cation of large size can form layered perovskites (2D, 1D) with a bandgap comparable to that of 3D perovskites. (Cheng and Lin 2010). Thus, the bandgap of metal halide perovskites increases when the metal on the B site is higher in the group of the periodic table (Ou, Bao et al. 2019). Thus, the replacement of lead in  $\text{MAPbI}_3$  by isovalent tin (Sn) or germanium (Ge) shows an increase in bandgap from 1.55 eV to 1.26 eV and 1.9 eV, respectively (Figure 1.12) (Nayak, Moore et al. 2016). Also, these metals get readily oxidized to +4 oxidation state, leading to instability in octahedral framework. (Krishnamoorthy, Ding et al. 2015; Ju, Dai et al. 2017)

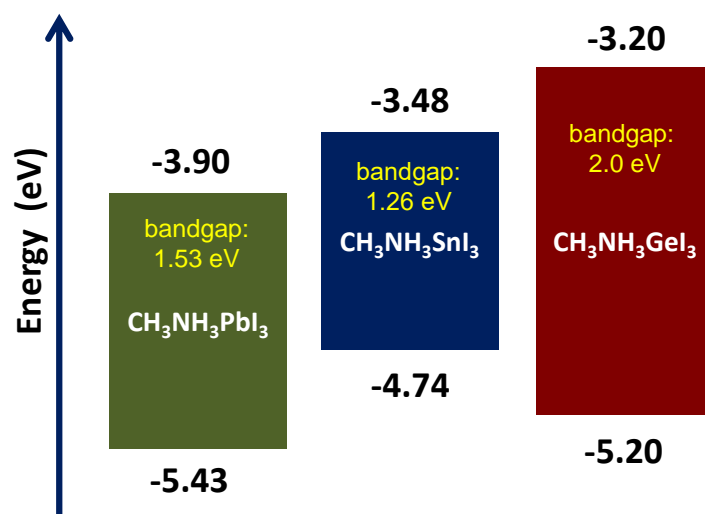


Figure 1.12 Effect of B site substitution on the bandgap of metal halide perovskites (Krishnamoorthy, Ding et al. 2015; Ye, Hong et al. 2016; Zhao, Gu et al. 2017)

Mixed isovalent metal halide hybrid perovskites exhibit a lower bandgap compared to single metal halide perovskites. Thus, for  $\text{CH}_3\text{NH}_3\text{Sn}_{1-x}\text{Pb}_x\text{I}_3$  where  $x=0$  to 1, the bandgap approaches 1.18 eV, depending upon the composition of perovskites. (Hao, Stoumpos et al. 2014)

The anions in the hybrid perovskites X sites are major components that control the bandgap of the material. Changes in the halides can bring about significant differences in the bandgap compared to the changes in the A cations. (Galkowski, Mitioglu et al. 2016) The reason for the change in bandgap can be related to the electronic state of anions. As the valence band composition changes from 3p to 4p to 5p for Cl, Br and I, respectively, there will be a corresponding decrease in electron binding energies, as evident from Figure 1.13. Thus, changing the I-Br ratio in the standard methylammonium halide perovskite can tune the bandgap because of their comparable ionic sizes (Noh, Im et al. 2013). But the I-Cl ratio in perovskites has not made any major change in the bandgap due to the significant difference in their size.

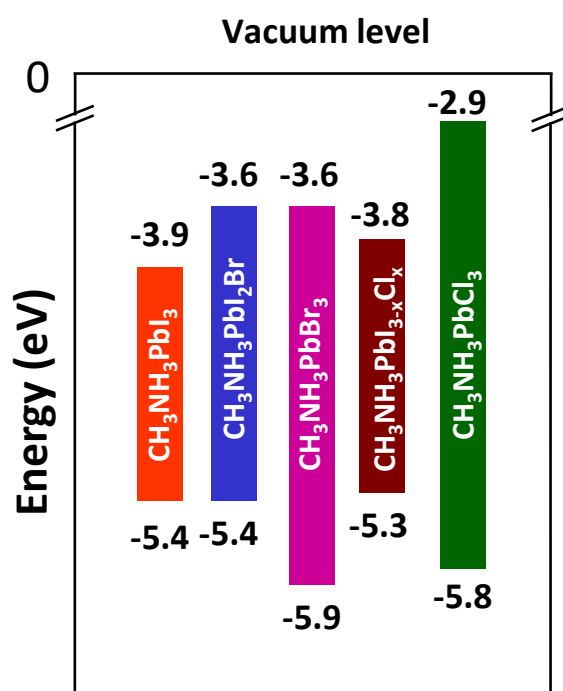


Figure 1. 13. The bandgap tuning of perovskites by halide substitution (Wu, Chen et al. 2018).

#### 1.2.4.2 Electrical properties

Hybrid perovskites exhibit exceptional carrier transport properties that confer their remarkable performance in photovoltaics and optoelectronics. The major factors that determine the electrical properties are charge carrier type, concentration, and mobility. However, in perovskites, these properties vary broadly, often influenced by their synthesis method. The coating thickness, smoothness, uniformity, grain size, etc., are the factors that determine their intrinsic electrical properties. Thermoelectric measurements of the Seebeck coefficient, Hall measurements of the conductivity's response to an applied magnetic field, or a thin-film transistor's response to a gating electric field are used to determine their charge carrier concentration. By tuning the precursor concentration, the carrier type can be modified. For example, if the concentration of the methylammonium cation is higher in  $\text{CH}_3\text{NH}_3\text{PbI}_3$ , it will lead the nature of the carrier to p-type. The electron mobility of polycrystalline  $\text{CH}_3\text{NH}_3\text{PbI}_3$  films is comparable to that of other absorber materials such as CdTe ( $10 \text{ cm}^2/\text{V}/\text{s}$ ) and

polycrystalline Si ( $100 \text{ cm}^2/\text{V.s}$ ). It is larger than the mobility of state-of-the-art thin polymer films ( $10 \text{ cm}^2/\text{V.s}$ ) and colloidal quantum dots ( $\sim 1 \text{ cm}^2/\text{V.s}$ ).

Hybrid perovskites are inexpensive in processing and they exhibit good tolerance to defects which offer a significant advantage over conventional semiconductors. The electrical properties of hybrid perovskites are correlated with their composition and morphology. The difference in the light and dark current in hybrid perovskites has been attributed to changes in the perovskite's Fermi level. This can arise due to more iodide vacancies on the surface or due to grain boundaries.

### **1.2.5 Synthesis strategies of hybrid perovskites**

The first reported synthesis of organometallic halide perovskite was  $\text{CH}_3\text{NH}_3\text{PbX}_3$ , by reacting  $\text{CH}_3\text{NH}_3\text{X}$  and  $\text{Pb}(\text{NO}_3)_2$  and an aqueous solution of  $\text{Br}_2$  at  $100^\circ\text{C}$ . Later on, methods based on solution processing and evaporation were established to synthesise organometallic hybrid halide perovskites.

#### **1.2.5.1 Solution-processed perovskites**

The solution-processing method is proved to be one of the most effective routes to achieve crystalline organometal halide perovskites. In this, both the metal halide and organic halide are dissolved in solvents like  $\gamma$ -butyrolactone (GBL), N,N-dimethylformamide (DMF) and dimethyl-sulfoxide (DMSO) and the perovskite product was precipitated by evaporation. A similar methodology can also synthesize mixed halide perovskite by varying the ratio of precursors. Perovskite can be deposited in the form of the films by spin coating the precursor solution on suitable substrates (generally conductive glass substrates) followed by heat treatment. Another approach to obtain the perovskite film of uniform morphology is by two-stage deposition followed by thermal annealing. This method is proven to be very effective in achieving better crystallinity in the system. Precise control of the morphology and phase of perovskite can be obtained by adding a small amount of  $\text{Cl}^-$ . Different solution processing methodologies are reported for the synthesis of single-crystal perovskites and nanocrystalline perovskites.

(a) Synthesis of single crystal perovskites

Single crystal perovskites can be synthesized by solution-processing techniques. Dong et al. reported the synthesis of single-crystalline perovskite materials with comparatively fewer defects, voids and grain boundary, using a temperature gradient top-growth method (Fang, Dong et al. 2015). Another method reports an anti-solvent, vapor-assisted crystallization approach (Jena, Kulkarni et al. 2019). In the latter method, the mechanism of single crystal formation is explained as the anti-solvent diffusion into a solution containing the perovskite precursors slowly, forming the perovskite single-crystal. Another interesting solvent/antisolvent vapor-assisted crystallization is through slow evaporation of the solution (Gedamu, Asuo et al. 2018). The disadvantage of this solution-mediated growth process of single crystal perovskites is the long duration, of the order of few months. Yet another effective method, requiring lesser time of crystallization was reported by Saidaminov et al. (Saidaminov, Abdelhady et al. 2015). They used the inverse temperature crystallization technique to synthesize good quality, bulk single crystals within few minutes. Figure 1.14 Schematic diagram shows synthesis setup adopted for the growth of large  $\text{CH}_3\text{NH}_3\text{PbI}_3$  single crystals.

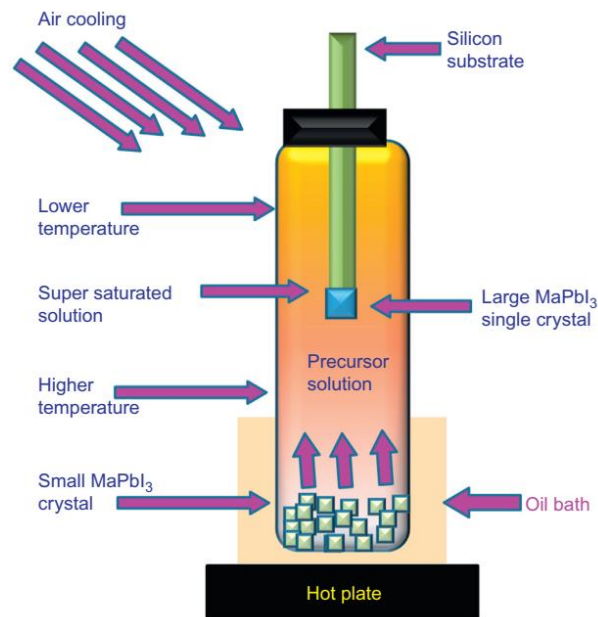


Figure 1.14. Schematic showing synthesis setup for the growth of large  $\text{CH}_3\text{NH}_3\text{PbI}_3$  single crystals. (Q, Dong. et al. 2015)

*(b) Synthesis of perovskite nanoparticles (NPs)*

Several methods have been demonstrated to synthesise the colloidal perovskite nanoparticles (NPs) including solvent-induced reprecipitation, ligand-assisted reprecipitation (LARP), hot injection method and template assisted synthesis (Shamsi, Urban et al. 2019).

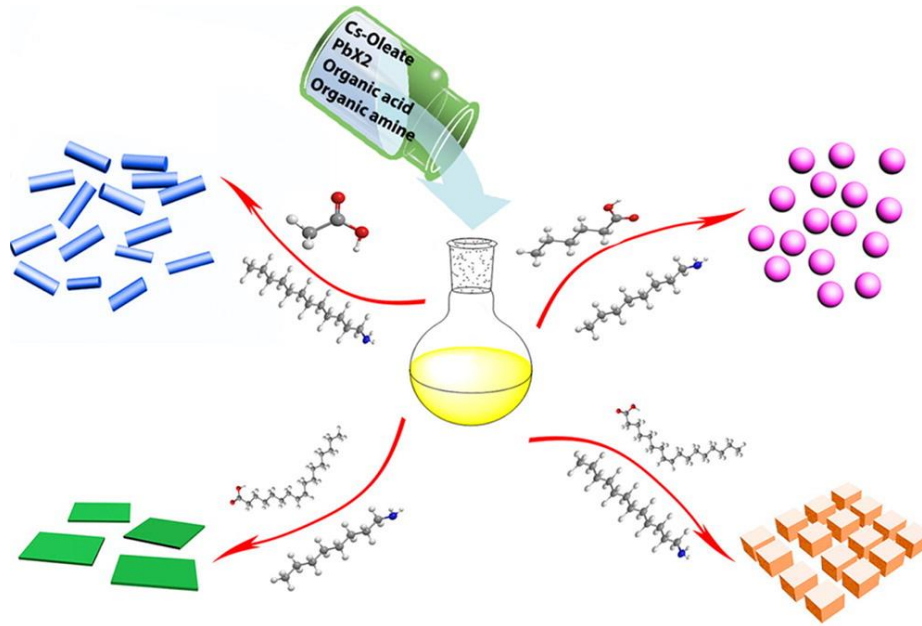


Figure 1.15. Schematic showing the formation of different types of nanocrystals (CsPbX<sub>3</sub> (X=Cl, Br, I)). The synthesis is done by organic acid and amine ligands at room temperature. Hexanoic acid and octylamine result in spherical quantum dots, oleic acid and dodecylamine leading to nanocubes, acetate acid and dodecylamine for nanorods few-unit-cell-thick nanoplatelets could be formed using oleic acid and octylamine.

Reproduced from (Sneha, A, Kulkarni et al. 2019)

*(i) Solvent-induced re-precipitation*

The size of the NPs can be controlled by using long chain amines, oleic acid, etc., which suppresses aggregation and ensures colloid stability. Thus, colloidal MAPbBr<sub>3</sub> NPs were synthesized by the reaction of perovskite precursors, methylammonium bromide (CH<sub>3</sub>NHBr) and lead bromide (PbBr<sub>2</sub>) in the presence of oleic acid (OAc) and octylamine (OA) in a suitable solvent. Upon addition of acetone to the hot mixture, the nanocrystals were precipitated. (Nie, Tsai et al. 2015)

(ii) *Ligand-assisted re-precipitation synthesis (LARP)*

In the LARP approach, perovskite precursors and n-octylamine and oleic acid were dissolved in polar solvent dimethylformamide (DMF) followed by dropwise addition of the antisolvent (poor solvent for the perovskites, e.g. toluene) under vigorous stirring conditions. (Prochazkova, Scharber et al. 2020). Another approach is the solution-processed, core-shell-type, mixed methylammonium-oleic acid lead bromide perovskite NPs ( $\approx 5\text{--}12$  nm). (Bhaumik, Veldhuis et al. 2016). The formation of core-shell-type NPs was achieved by altering the molar ratio of capping ligands, OABr and MABr.

(iii) *Hot Injection Method*

The hot injection method is one of the most commonly used synthesis methods for  $\text{CsPbX}_3$  NPs. A typical process involves the mixing of perovskite precursors,  $\text{PbX}_2$  ( $X = \text{I/Br/Cl}$ ) in octadecene (ODE) along with oleic acid and oleylamine at  $140\text{--}200$  °C followed by the quick injection of Cs-oleate (de Mello Donegá, Liljeroth et al. 2005; Kwon and Hyeon 2011; Pu, Cai et al. 2018).

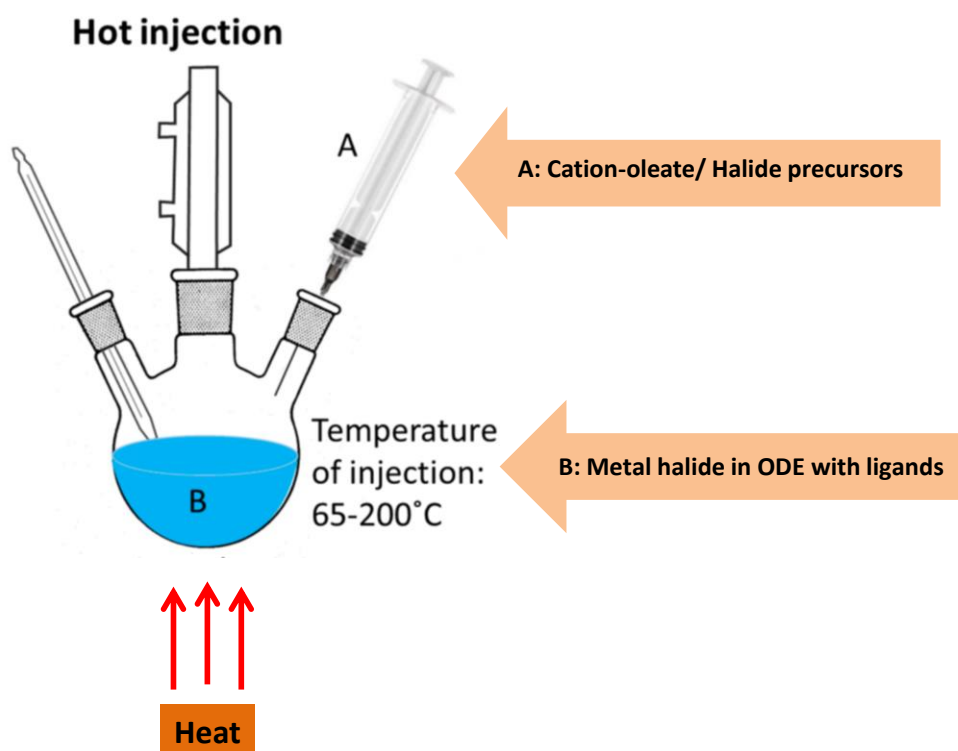


Figure 1.16 Schematic showing hot injection method for preparation of perovskite nanoparticles. (Haijiao et al. 2018)

#### **1.2.5.2 Template assisted synthesis**

In the template assisted approach, NPs formation is induced by the crystallization on a specific substrate that acts as a template (Shi, Ding et al. 2019). Mesoporous silica and aluminum oxide films are the commonly used templates.

#### **1.2.5.3 Thermal evaporation method**

In the thermal evaporation method, both single source and co-evaporation are envisaged for synthesizing hybrid perovskites with good crystallinity. The major limitation of co-evaporation method is that it needs precise control on the flow rate of the precursors, which is a great challenge due to their high vapour pressure. Mixed halide perovskites with smooth surface and small grain size have been achieved by a low temperature, vapour-assisted, solution processing technique. (Liu, Johnston et al. 2013).

#### **1.2.5.4. Chemical vapour deposition (CVD)**

CVD has been reported as an effective means for fabricating low-dimensional perovskites by different steps. The reaction steps of CVD include vapor-based reagents generation, reactant transport, chemical reaction and reaction by-product removal. The equipment used in CVD method possesses a gas source control unit, deposition reaction chamber, deposition temperature control unit and vacuum unit, including exhaust and pressure control unit. The growth of nanocrystals of perovskites can be effectively tuned by optimising the temperature and pressure conditions.

Nanowires and nanoplatelets of methylammonium lead halide perovskite were synthesised by the CVD method as shown in figure 1.17 (Liu, Cao et al. 2019).

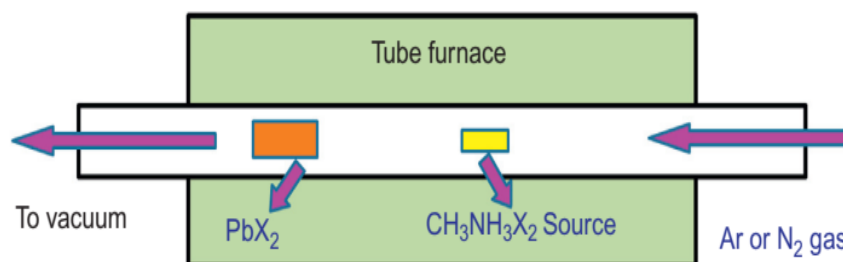


Figure 1. 17 Scheme showing the chemical vapour deposition method for hybrid perovskite synthesis. Using a single-zone heating tube furnace, there are 20 ° C temperature differences between the location of  $\text{PbI}_2$  substrate (130 ° C ) and MAI precursor (150 ° C) (Kim, An et al. 2019).

### 1.2.6. Applications of hybrid perovskites

Hybrid perovskites are a class of semiconductor materials inspiring researchers in the hopes of developing highly efficient, low-cost and stable energy conversion devices. Their salient features, such as strong photoluminescence, low nonradiative recombination rates and long carrier lifetime, and tunable absorption and emission properties render the hybrid perovskites suitable for various optoelectronic devices. Figure 1.18 shows the various potential applications of hybrid perovskites.

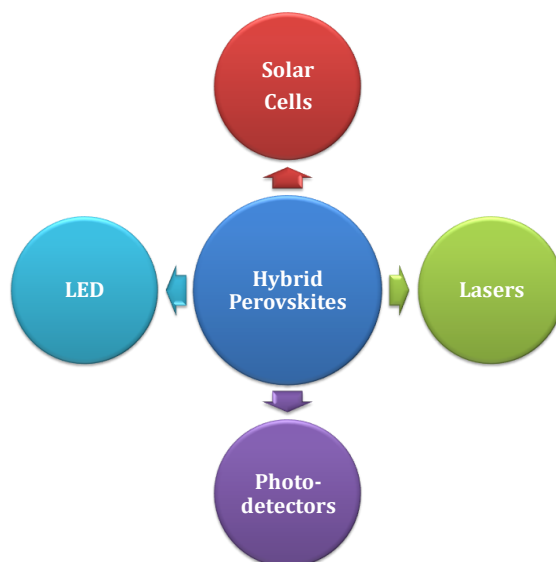


Figure 1. 18. Potential applications of hybrid organic/inorganic perovskites (HOPs)

### 1.2.6.1 Perovskite photovoltaics

State-of-the-art silicon based solar cells are costly and they encounter difficulty in fabrication. To overcome these challenges, second (inorganic thin film solar cells) and third generation (DSSC, organic solar cells, perovskites solar cells) solar cells also have emerged.

Recently, hybrid organic/inorganic perovskites have attracted enormous attention in photovoltaic technology due to their unique light harvesting capability, ease of fabrication and low cost. The precursors are also readily available. Initially,  $\text{CH}_3\text{NH}_3\text{PbBr}_3$  and  $\text{CH}_3\text{NH}_3\text{PbI}_3$  were reported as light harvesting materials with power conversion efficiency (PCE) of 2.6% and 3.8%, respectively by Kojima et al. in 2009. In 2012, the first solid-state hybrid metal halide perovskite solar cells with a PCE of  $\sim 9.7\%$  have been reported with  $\text{CH}_3\text{NH}_3\text{PbI}_3$  as the active material. Presently it reaches  $\sim 21.2\%$  (Yoo, Seo et al. 2021). Tunable band gap, high absorption coefficient, low exciton binding energy, easy processing and excellent charge carrier mobility are the attractive properties of metal halide perovskites, rendering them a promising candidate for the high efficiency solar cells

### 1.2.6.2 LEDs

Light-emitting diodes (LEDs) have revolutionised the lighting industry by replacing incandescent and fluorescent lightings. LED is a semiconductor device that emits visible light when an electric current passes through it. The output from a LED can range from red (wavelength  $\sim 700$  nm) to blue-violet (about 400 nm). Some LEDs emit infrared (IR) energy (830 nm or longer). An LED consists of a p-type semiconductor and n-type semiconductor. When they are placed in direct contact, a p-n junction is formed, which emits light when activated. (Parola, Julián-López et al. 2016).

LEDs are based on direct bandgap semiconductors; device fabrication is not an easy task as they are processed at high temperatures and vacuum. Perovskites that are direct-bandgap semiconductors can be used as an active material for LED fabrication. These materials also emit light very strongly, which makes them very suitable for making LEDs. The light emitted by the perovskites

can be easily tuned and fabricated make them ideal material for LEDs (Liu, Xu et al. 2020).

### **1.2.6.3. Lasers**

Lasers find tremendous applications in different fields like lighting, telecommunications, displays, optical fibers, etc. But the integration of high performance semiconductors into the silicon substrate and the high temperature process are major limitations. Perovskite-based lasers are reported at low temperatures (40K) in the early 1990s where layered structures  $(\text{C}_6\text{H}_{13}\text{NH}_3)_2\text{PbI}_4$  are used. Many efforts are taken worldwide to develop hybrid organometallic perovskite-based lasing materials.  $\text{CH}_3\text{NH}_3\text{PbI}_3$  single crystals showed room temperature lasing property over wide range of wavelengths (Zhang, Su et al. 2017). The working range of lasers is varied by changing the halides ions hence by tuning the bandgap in the mixed halide materials. Furthermore, optically pumped lasing has also been demonstrated at room temperature using  $\text{CH}_3\text{NH}_3\text{PbI}_3$ -based systems. It is also reported that better lasing action can be achieved in nanostructured perovskites (Tang, Hu et al. 2017).

### **1.2.6.4 Photodetector**

Photodetectors are widely used in fibre optic communication systems, process control, environmental sensing, safety and security and defence-related applications. Photodetectors employ semiconductor materials having significant absorption, extinction coefficient and highly mobile charge carriers.  $\text{CH}_3\text{NH}_3\text{PbI}_3$  perovskite exhibits significant light-absorption properties and long-lived photogenerated carriers, which results in high quantum yield and high gain in photoconductivity. Xie et al. reported a wide range of photoresponse from 780 to 310 nm, about 3.49 A/W photoresponse and external quantum efficiency (EQE) of  $1.19 \times 10^3 \%$  at 365 nm for a flexible  $\text{CH}_3\text{NH}_3\text{PbI}_3$  film photodetector. Hybrid perovskite ( $\text{CH}_3\text{NH}_3\text{PbI}_3\text{Cl}_x$ ) based photodetectors with an inverted device structure are reported by (Xia, Tong et al. 2018).

## 1.3 Scope and Objectives

Perovskite technology is less explored and offers high potential for various applications such as solar cells, photodetectors, LEDs, etc. Recently, HOPs have attracted attention as an active material for photovoltaic applications. However, their poor environmental stability remains a major challenge and concern. Numerous research works are going on towards addressing such issues. Although extensive studies are in progress on developing perovskite-based devices, the fundamental properties of these materials remain to be fully understood, making them an active topic of research. The present research thesis focuses on the synthesis and characterisation of different HOPs using various approaches and systematic studies of their structural, photo-physical, optical and morphological features.

### **Objectives:**

- Synthesis and characterization of hybrid organic/inorganic perovskites of less explored perovskites based on lead, tin and copper cations and ionic liquids and halides as anions
- Systematic studies on structural, photo-physical, optical and morphological features and correlate to the chemical structure and composition.
- Tuning the morphology and composition of perovskites to suit various applications
- Evaluation of photovoltaic properties and correlation to composition, morphology and construction of the device

# CHAPTER 2

## MATERIALS AND METHODS

### 2.1 Materials

The chemicals used for the synthesis of perovskites have been purchased from Sigma Aldrich, stored under a glove box and used as received. Some of the chemicals are listed below.

#### 2.1.1 Inorganic halides

Lead (II) chloride ( $\text{PbCl}_2$ ), lead (II) bromide ( $\text{PbBr}_2$ ), tin (II) bromide ( $\text{SnBr}_2$ ), copper (II) chloride ( $\text{CuCl}_2$ )

#### 2.1.2 Ionic liquids

Methylimidazoliumchloride ( $\text{MimCl}$ ), 1-ethyl-3-ethylimidazoliumchloride ( $\text{C}_2\text{mimCl}$ ), 1-butyl-3-methylimidazolium chloride ( $\text{C}_4\text{mimCl}$ ) and 1-hexyl-3-methylimidazolium chloride ( $\text{C}_6\text{mimCl}$ ).

#### 2.1.3 Organic halides

Methylammonium bromide ( $\text{MABr}$ )

#### 2.1.4 Azo dye sensitizer

di-tetrabutylammonium cis-bis(isothiocyanato)bis(2,2-bipyridyl-4,4-dicarboxylato)ruthenium(II) (N719 dye)

#### 2.1.5 Polymeric encapsulant

The oligomer used was polysilsesquioxanes (molecular weight, MW ~1200), functionalised with epoxy and amine groups - synthesised in-house.

#### 2.1.6 Coatings and solvents

Titanium diisopropoxidebis(acetylacetonate) (75%), lithium bis-(trifluoromethylsulphonyl)imide, hydrogen peroxide ( $\text{H}_2\text{O}_2$ ) 30%, butanol, dimethylformamide (DMF) 99%, toluene (99%) chlorobenzene and acetonitrile

### **2.1.7 Solar cell substrates and electron transport layer**

Fluorine-doped tin oxide (FTO) glass substrate 15 Ohm/Sq (Dyesol), mesoporous titanium dioxide (Dyesol)-electron transport layer

## **2.2 Characterisation Methods**

### **2.2.1 Fourier transform infrared (FTIR) spectroscopy**

FTIR spectrum primarily gives information about functional groups and identifying different kinds of chemical bonds present in a molecule. The wavelength of light absorbed is characteristic of the chemical bond present in the molecule. FTIR analysis was performed using a Nicolet iS50 FTIR spectrometer at a resolution of 4  $\text{cm}^{-1}$ . The spectra have been collected in the wavelength range of 400-4000  $\text{cm}^{-1}$  and averaged for 16 scans. The spectra are recorded in transmission mode using KBr pellets.

### **2.2.2 Raman spectroscopy**

The Raman spectra were recorded using a WITec alpha 300R confocal Raman microscope with an excitation wavelength of 532 nm by accumulating 5 spectra with an integration time of 1 s. Laser power at the sample was 25 mW.

### **2.2.3 X-ray Diffraction**

X-ray diffraction studies can be done for single crystals or powder samples. Single-crystal XRD gives absolute structure determination of a material. With single-crystal XRD data, the exact atomic positions can be observed, and thus bond lengths and angles can be determined. This technique provides the structure within a single crystal, which does not necessarily represent the bulk of the material. Therefore, additional bulk characterisation methods must be utilised to prove the identity and purity of a compound. Single crystal XRD data were collected using a BRUKER D8 VENTURE SC-XRD with Mo- and Cu-radiation. Crystal cell constants were calculated by Full-matrix least-squares on F2 and the structures were solved by direct methods using SHELXS (graphical user interface for the structure refinement program)

The powder pattern provides information about the phase (polymorph) and crystallinity of the material. Powder X-ray diffraction (XRD) studies were performed in a Bruker D8 Discover diffractometer using Cu K $\alpha$  radiation (0.154 nm) at a scan rate of 4.8°/min at 2 $\theta$ = 10°-70. Crystallite size was measured by the Debye-Scherrer equation as given in equation 2.1. This equation gives the relationship between diffraction peak broadening ( $\beta$ ) and crystallite size (D).  $\theta$  represents the angle of diffraction and  $\lambda$  is the wavelength of X-ray used

$$D = 0.94\lambda / \beta \cos \theta \text{-----}(2.1)$$

#### **2.2.4 X-ray photoelectron spectroscopy (XPS)**

X-ray photoelectron spectroscopy (XPS) is a quantitative spectroscopic technique based on the photoelectric effect used to identify the elements and the chemical state. X-ray photoelectron spectroscopy (XPS) analysis was carried out with Multilab 2000 (Thermo Fisher Scientific) using a polychromatic Al-K $\alpha$  radiation ( $h\nu = 1486.6$ ). The samples were drop-casted on a sample stub and dried before doing the measurements.

#### **2.2.5 Inductively coupled plasma atomic emission spectroscopy ICP-AES**

Inductively coupled plasma atomic emission spectroscopy (ICP-AES) is an emission spectroscopy technique in which the interaction of the material with plasma causes ionisation of the material to atoms or ions and emits electromagnetic radiation at wavelengths characteristic of a particular element. ICP-AES analysis, the solid samples were digested in con. HNO<sub>3</sub> to convert all the lead to lead nitrate. This solution was further diluted and then injected into the plasma (the detection limit of Al in ICP-AES is 0.1 ppm) in a Perkin Elmer Optima 4300 V (USA) instrument.

#### **2.2.6 UV-Visible spectroscopy**

Ultraviolet-visible spectroscopy (UV-Vis or UV/Vis) refers to absorption spectroscopy or reflectance spectroscopy uses ultraviolet and the visible regions of the electromagnetic spectrum to excite a molecule and undergo

electronic transitions (HOMO to LUMO). The UV-Visible spectra were recorded using a Perkin Elmer Lambda 950 UV-Visible spectrometer. Powder samples were characterised using the solid-state diffuse reflectance spectra (DRS) mode. The wavelength range used was from 250-800 nm with a resolution of 1 nm. The band gap of the material was calculated using the Tauc plot. The relation used for the Tauc plot is

$$(h\nu\alpha)^{1/n} = A(h\nu - E_g) \text{-----}(2.2)$$

Where ‘ $h\nu$ ’ represents the photon energy,  $\alpha$  is the absorption coefficient of the material,  $E_g$  is the bandgap and  $A$  is the absorbance of the material. By extrapolating this linear region to the abscissa yields the energy of the optical bandgap of the amorphous material (Hafdallah, Yanineb et al. 2011).

$n = 1/2$  for direct allowed transitions

$n = 3/2$  for direct forbidden transitions

$n = 2$  for indirect allowed transitions

$n = 3$  for indirect forbidden transitions

### **2.2.7 Fluorescence spectroscopy**

Fluorescence measurements were done using a FluoroMax-4C Spectrofluorometer (Horiba Instruments, USA) using an appropriate excitation wavelength with an integration time of 0.1 s. Excitation and emission slit widths were kept at 5 nm. Time-resolved fluorescence measurements were done using time-correlated single-photon counting (TCSPC). The laser used is a picosecond diode laser, with 1 nm excitation band-pass and 9.5 nm emission band-pass (Horiba Instruments, USA).

### **2.2.8 Differential scanning calorimetry (DSC)**

Differential scanning calorimetry (DSC) measures the enthalpy changes of material that arises due to changes in the physical and chemical properties as a function of temperature or time. DSC was performed using a TA Q20 calorimeter and the measurements started from room temperature to 200 °C at a heating rate of 5 °C/min.

### **2.2.9 Thermogravimetric analysis (TGA)**

Thermogravimetric analysis or thermal gravimetric analysis (TGA) is a method of thermal analysis in which the sample is heated in a controlled atmosphere at a specific heating rate and the mass change of a sample is measured as a function of time or temperature. The TGA measurements were carried out using Perkin Elmer Pyris 1 in N<sub>2</sub> atmosphere at a heating rate of 10 °C/min from 30 °C to 800 °C.

### **2.2.10 Atomic force microscopy (AFM)**

The AFM is based on the interaction of cantilever/tip (probe) assembly with the sample. The movement of the AFM probe above the sample surface is by a raster scanning motion. The raster motion of the AFM tip above the sample surface is monitored through a laser beam reflected off the cantilever. This reflected laser beam is tracked by a position sensitive photo-detector (PSPD) that picks up the vertical and lateral motion of the probe. The deflection sensitivity of these detectors has to be calibrated in terms of how many nanometers of motion corresponds to a unit of voltage measured on the detector. The AFM imaging was carried out using an Agilent 5500 instrument in contact mode using a silicon nitride tip. Samples were dispersed in solvent and drop casted on a silicon substrate and dried under vacuum and used for analysis. The roughness parameter was calculated from surface topography images using 'PicoView' software.

### **2.2.11 Field emission scanning electron microscope (FE-SEM)**

In FE-SEM high-energy beams of electrons are liberated by a field emission source used to scans the sample surface in a raster scanning pattern. The FE-SEM of the sample are carried out using a FEI GEMINI 500 FE-SEM and a Carl Zeiss Sigma HD (Germany) FE-SEM instruments. The acceleration voltage was ~10 kV. Energy dispersive X-ray Spectroscopy (EDS) of gold-coated powder samples were recorded using an Oxford Inca (UK) energy dispersive X-ray spectrometer.

### **2.2.12 Transmission electron microscopy (TEM)**

Transmission electron microscopy (TEM) is a microscopy technique that uses the beam of electrons to transmit through the sample and interacts with the sample to form an image. The TEM images were obtained using a JEOL 3010 UHR instrument. Samples were dispersed in toluene by ultrasonication method and drop-casted on a carbon-coated copper grid and dried under vacuum at room temperature. The electron beam voltage was reduced to 200 kV and the images were recorded with a minimum exposure time to avoid sample damage.

### **2.2.13 Cyclic voltammetry (CV)**

Cyclic Voltammetry (CV) is an electrochemical technique that measures the current that develops in an electrochemical cell under conditions where voltage is in excess of that predicted by the Nernst equation. CV is performed by cycling the potential of a working electrode and measuring the resulting current. Cyclic voltammetry takes the three-electrode setup, where the working electrode reaches a set potential, the ramp is inverted. This inversion can happen multiple times during a single experiment. The current at the working electrode is plotted versus the applied voltage to give the cyclic voltammogram.

Cyclic voltammetry (CV) was done in three-electrode configuration using CHI7014E potentiostat. The HOMO level of the oligomer was predicted using Gaussian 09 software. The perovskite solution was coated on a fluorine-doped tin oxide (FTO) glass as the working electrode, Ag/AgCl as the reference electrode and Pt wire as the counter electrode. The electrolyte consisted of a solution containing 0.1 g AgCl and 0.01 g of tetraethylammonium perchlorate dissolved in dry acetonitrile solvent.

The highest occupied molecular orbital (HOMO) represents the energy required to extract an electron from a molecule (oxidation process) and LUMO is the energy necessary to inject an electron into a molecule (reduction process). These processes can be measured using the cyclic voltammetry method by

measuring the redox potentials  $E_{\text{red}}$  and  $E_{\text{ox}}$ . Ferrocene is used as a known reference to calculate the energy of the HOMO and LUMO levels, including the ferrocene value of -4.4 eV. The energy levels were calculated using the following empirical Bredas et al. equations (Leonat, Sbarcea et al. 2013):

$$E(\text{HOMO}) = -e [E_{\text{oxonset}} + 4.4], \text{-----(2.3)}$$

$$E(\text{LUMO}) = -e [E_{\text{redonset}} + 4.4] \text{-----(2.4)}$$

#### **2.2.14 Photocurrent measurement**

Perovskite solution was coated on a fluorine-doped tin oxide (FTO) glass slide and was irradiated using a 354 nm band-pass filter ( $\lambda$  band-pass=354±20 nm, LOT Oriel 200 W high-pressure mercury lamp) and the dark and light currents were measured. To investigate the photo-response, UV irradiation experiments were carried out and the photocurrents were monitored.

#### **2.2.15 Impedance spectroscopy**

The electrical measurements were performed using an electrochemical workstation (M/s. BioLogic, Model: VMP3). The impedance spectroscopy measurements were carried out in dark conditions under the applied DC voltage of 0 V to the sample. A small AC modulation of 10 mV with frequency ranges from 10 mHz–1MHz was applied. The measurements were carried out without any mask on the samples for comparing impedance data. The total area of the solar cell is 1 cm<sup>2</sup>. At each frequency, DC, DC voltage and time were recorded for analysing the impedance data. The impedance data were analysed using the BioLogic ‘EC-Lab’ software with in-built impedance simulation and fitting functions.

#### **2.2.16 Computational methods**

The interactions of ILs and PbCl<sub>2</sub> were analysed using B3LYP (Becke 1996) level of the method using 6-31+G (d, p) basis set. All DFT calculations were performed by using the molecular theory package Gaussian 09 (Frisch, Trucks et al. 2009). The molecular level interactions are studied using ILs-PbCl<sub>2</sub> systems where the stable conformation of hexacoordinate geometries of PbCl<sub>2</sub>

was considered. Optimisation of N 719 dye, MAPbBr<sub>3</sub> and oligomer molecule were done using the semiempirical method.

To explore the crystal structure of hybrid organic/inorganic perovskites , density functional theory (DFT) calculations were done using the Vienna ab initio simulation package (VASP) with the projector augmented wave (PAW) methods (Blöchl 1994), (Kresse and Furthmüller 1996). Perdew–Burke–Ernzerhof (PBE), under the generalised gradient approximation (GGA) as the exchange-correlation functional was used (Perdew, Burke et al. 1996). The cutoff energy of the plane wave function was set to 500 eV.

# CHAPTER 3

## IONIC LIQUID BASED HYBRID PEROVSKITES: SYNTHESIS, CHARACTERISATION AND EVALUATIONS

### 3.1 Introduction

The hybrid organic-inorganic materials constitute an interesting class of materials with well-defined molecular architecture and tunable properties (Faustini, Nicole et al. 2018; Saveleva, Eftekhari et al. 2019). These hybrid materials can exist as isolated complex anions (0D), as one-dimensional anions (1D), two-dimensional (2D) sheets and also as three-dimensional (3D) network structures (Dobrzycki and Woźniak 2008; Colodrero, Olivera-Pastor et al. 2010). The structural versatility of these materials is attributed to the different interactions leading to the polymerisation/organisation of the anions. Such 2D and 3D crystalline hybrid organic-inorganic materials possess structural features corresponding to perovskites (Zhang, Hejazi et al. 2013; Li, Wang et al. 2017).

2D layered materials have attracted a great deal of attention since they exhibit superior thermal stability and good resistance to moisture ingress (Tsai, Nie et al. 2016; Yang, Gao et al. 2018). Their versatility is attributed to their layered structure and the extra organic cation populating the interlayer space, which offers better synthetic flexibility and tunability in their properties. The choice of organic cations and their stoichiometry is the most influential parameters determining the conformation of the resultant hybrid frameworks (Stoumpos, Cao et al. 2016; Cortecchia, Neutzner et al. 2017; Chen, Sun et al. 2018).

The nature of metal cations can play a crucial role in the formation of H-bonding interactions, ionic interactions between cations and the anionic substructures, inert electron– pair effect, coordination environment of halide ions, steric factors, etc. which can determine the orientation, rigidity and conformation of the interlayer organic cations (Li, Lin et al. 2006; Chen, Sun et al. 2018). Lead is generally chosen as the metal cation owing to its flexible coordination sphere. Inert electron

pair and related effects, coordination environments of halide anions, steric and hydrogen bonding effects, etc., also play vital roles. Chloroplumbate (II) structures form 1D strands, 2D sheets of polyanions and low-dimensional crystalline materials that exhibit electro-optic characteristics such as photoluminescence (PL), electroluminescence and nonlinear optical properties. The choice of organic cations can influence both the dimensionality of the inorganic sheets and the crystallographic orientation of the inorganic framework by changing the desired properties. Most of the organic moieties used in the construction of ammonium salt-metal halides have non-functional groups such as alkyl chains that contribute a secondary role to improve the processability of the hybrids. To tune the electro-optic properties of these materials, attempts have been made to modify their solid-state structures by incorporating ionic liquids. Properties of ionic liquids (ILs) are dictated by various interactions between the cations and anions, i.e., coulombic interactions, dipole interactions, electron pair donor-acceptor interactions, and hydrogen bonds (Wilkes 2004; Feng, Zhao et al. 2010; Goossens, Lava et al. 2016). From the wide variety of ILs, those based on imidazolium are of interest due to various crystalline structures and properties derived thereof (Holbrey, Reichert et al. 2004; Wang, Sternberg et al. 2014).

In this chapter, we illustrate the synthesis and characterization of different layered hybrid perovskites formed by reactions of ILs; methylimidazolium chloride (MimCl) and alkylmethylimidazolium chlorides (AmimCl) viz., (i) 1-ethyl-3-methylimidazolium chloride ( $C_2\text{mimCl}$ ), (ii) 1-butyl-3-methylimidazolium chloride ( $C_4\text{mimCl}$ ) and (iii) 1-hexyl-3-methylimidazolium chloride ( $C_6\text{mimCl}$ ) with lead (II) chloride ( $\text{PbCl}_2$ ). Theoretical calculations were performed on the probable structure and geometry, which were validated by experimental techniques. To the best of our knowledge, this is the first systematic investigation on the influence of methyl imidazolium cation and substituted methyl imidazolium cations on the structure, optical and electronic properties of the ILs- $\text{PbCl}_2$  hybrid materials.

## 3.2. Synthesis of the Hybrid Perovskites

The chemical structures imidazolium compounds are given in Fig 3.1. Synthesis involves the reaction of the ILs and  $\text{PbCl}_2$  in the molar ratio of 40:60 in DMF, at 50 °C. The solvent was removed under vacuum at 90 °C. The products were purified using toluene, dried under vacuum, and used for characterisation.

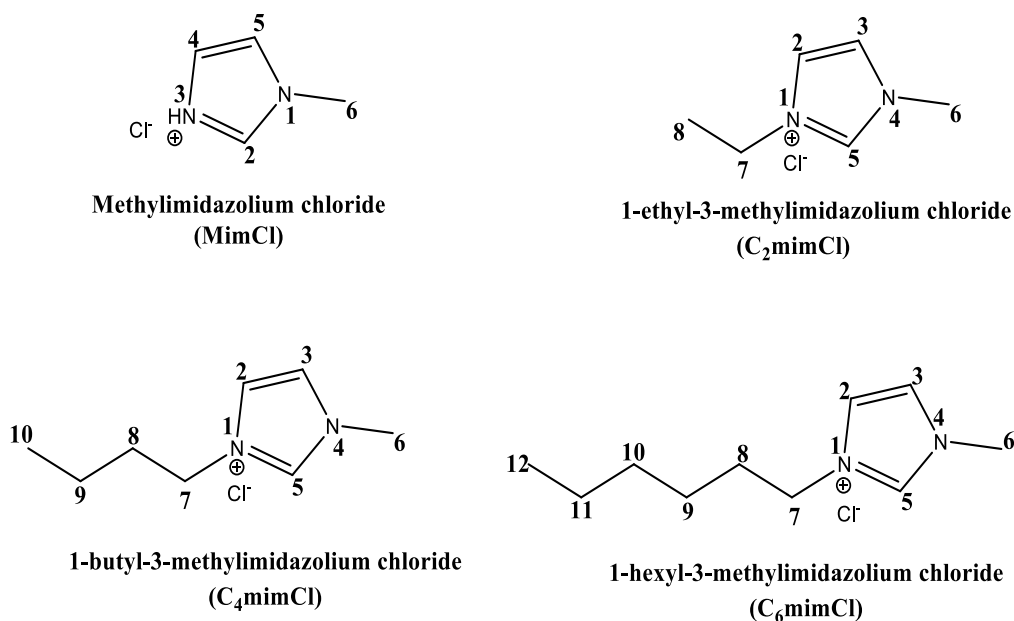


Figure 3.1. Chemical structures of ionic liquids (ILs), used in this study.

## 3.3. Results and Discussion

A series of ILs were reacted with  $\text{PbCl}_2$  for synthesising the ionic liquid-lead chloride hybrid perovskites. Starting from 10 mol% to 90 mol% of ILs with that of  $\text{PbCl}_2$  have been attempted to synthesise hybrid materials. The solid powders obtained by  $\text{PbCl}_2$ :ILs (60:40) reaction was used for detailed characterisations and further studies. Compositions of the synthesised products were deduced by elemental analyses using inductively coupled plasma – atomic emission spectroscopy (ICP-AES) and the results are summarised in Table 3.1. The data shows that Pb content is ~55 mol% in all ILs- $\text{PbCl}_2$  systems.

**Table 3.1.** Chemical composition of the synthesised perovskites obtained from ICP-AES analysis.

<b>Sample designation</b>	<b>PbCl<sub>2</sub></b> (mol%)	<b>Ionic liquid</b> (mol%)
MimCl-PbCl <sub>2</sub>	54	46
C <sub>2</sub> mimCl-PbCl <sub>2</sub>	55	45
C <sub>4</sub> mimCl-PbCl <sub>2</sub>	52	48
C <sub>6</sub> mimCl-PbCl <sub>2</sub>	55	45

### 3.3.1 Structural Characterisation

The hybrid materials were subjected to Raman spectroscopy, FTIR spectroscopy and XPS analysis to evaluate their structural characteristics. The results were then correlated with theoretical results. In general, the Raman spectrum of PbCl<sub>2</sub> exhibits a characteristic peak at 157 cm<sup>-1</sup> with shoulders at 133, 146 and 179 cm<sup>-1</sup>, which corresponds to A<sub>1g</sub>+B<sub>2g</sub>, B<sub>2g</sub> and B<sub>1g</sub> modes, respectively (Posypaiko and Alekseeva 1987). It is reported that the characteristic band of the Pb-Cl<sub>t</sub> (terminal) stretching frequencies fall in the range 200 and 300 cm<sup>-1</sup>, whereas the peak due to Pb-Cl<sub>b</sub> (bridging) appears at ~173 cm<sup>-1</sup> (Coleman, Feng et al. 2013). The lead (II) forms pentacoordinate plumbate systems with shorter bond length and hexacoordinated plumbate systems with longer bond length, respectively, owing to crystal polymorphism. The peak at 240 cm<sup>-1</sup> arises from Pb-Cl with a shorter bond length-pentacoordinatedplumbate-ILs structure, whereas the peaks at ~215 cm<sup>-1</sup> arise from Pb-Cl with longer bond length-hexacoordinated plumbate-ILs structure (Bonamartini Corradi, Ferrari et al. 2001). The chemical interactions between Pb and ILs have been explored using Raman spectra. Raman bands at ~220 cm<sup>-1</sup> and ~240 cm<sup>-1</sup> are attributed to hexacoordinated and pentacoordinated plumbate systems, respectively (Figure 3.2). The C<sub>2</sub>mimCl-PbCl<sub>2</sub> and C<sub>6</sub>mimCl-PbCl<sub>2</sub> showed Raman bands at 215 cm<sup>-1</sup> which is attributed to hexacoordinated plumbate systems, whereas C<sub>4</sub>mimCl-PbCl<sub>2</sub> gave rise to two different peaks at 215 cm<sup>-1</sup> and 243 cm<sup>-1</sup>. An additional peak at ~163 cm<sup>-1</sup> in the spectrum confirms the existence of hexacoordinated plumbate-ILs structure for C<sub>2</sub>mimCl-PbCl<sub>2</sub>, C<sub>4</sub>mimCl-PbCl<sub>2</sub> and C<sub>6</sub>mimCl-PbCl<sub>2</sub>.

In all these structures, the prevalence of a dense network of hydrogen bonds between the chloroplumbate (II) strands and the surrounding cations also is indicated. Thus, the formation of pentacoordinated and hexacoordinated plumbate structures form two different structural motifs, namely indefinite 1D strands and 2D sheets, respectively.

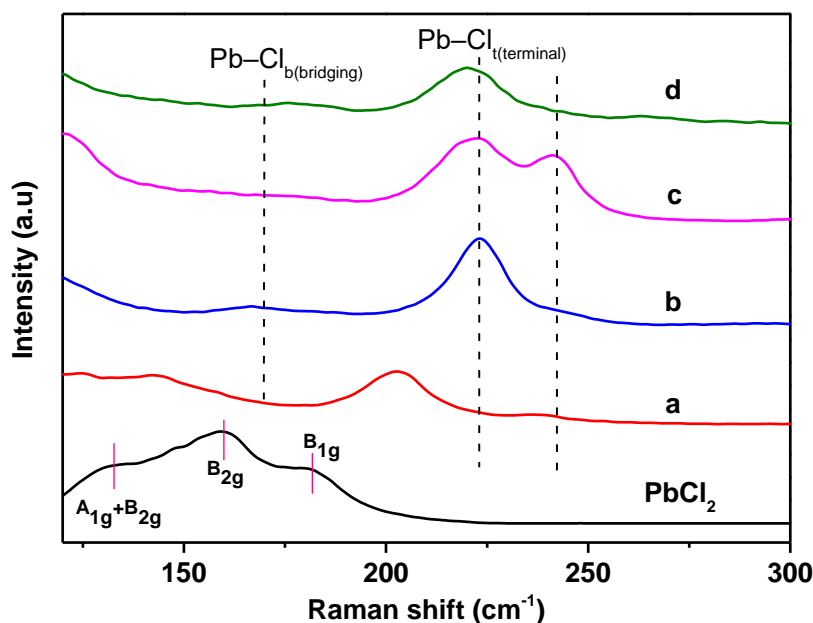


Figure. 3.2. Raman spectra of (a) MimCl-PbCl<sub>2</sub>, (b) C<sub>2</sub>mimCl-PbCl<sub>2</sub>, (c) C<sub>4</sub>mimCl-PbCl<sub>2</sub> and (d) C<sub>6</sub>mimCl-PbCl<sub>2</sub>. The A<sub>1g</sub>+B<sub>2g</sub>, B<sub>2g</sub> and B<sub>1g</sub> modes of vibrations are marked in the figure. The label Pb-Cl<sub>b</sub> represents bridging bonds and Pb-Cl<sub>t</sub> represents terminal bonds.

Note: ILs do not show any absorption in the range of 150 – 300 cm<sup>-1</sup> region and the individual ILs Raman spectra are omitted to avoid crowding.

XPS spectrum of Figure 3.3 A shows the binding energy corresponds to (C 1s), nitrogen (N 1s), chloride (Cl 2p), and lead (Pb 4f<sub>7/2</sub>) orbitals. The binding energy of Pb<sup>0</sup> is in the range of 136.3-136.9 eV. In PbCl<sub>2</sub>, binding energies of 4f<sub>7/2</sub> and 4f<sub>5/2</sub> are estimated to be 138.80 eV and 143.66 eV, respectively. However, in C<sub>2</sub>mimCl -PbCl<sub>2</sub>, Pb 4f core level binding energy shifts to 137.8 eV and 142.8 eV, corresponding to Pb 4f<sub>7/2</sub> and 4f<sub>5/2</sub>, respectively (Figure 3.3B). This shift to lower values implies that charge transfer occurs between Pb and Cl species to form donor-acceptor complexes.

For MimCl-PbCl<sub>2</sub>, the difference in binding energy for the 4f (4f<sub>7/2</sub> and 4f<sub>5/2</sub>) peak of Pb<sup>2+</sup> was ~0.2 eV. For C<sub>2</sub>mimCl-PbCl<sub>2</sub> the shift was ~0.9 eV while C<sub>4</sub>mimCl-PbCl<sub>2</sub> and C<sub>6</sub>mimCl-PbCl<sub>2</sub>, the difference was ~0.5 eV and ~0.4 eV, respectively. These differences in binding energy are due to the polymorphic structures formed between Pb<sup>2+</sup>, Cl<sup>-</sup> and imidazolium cation. The chloride anions with lower binding energy (Figure 3.3C) indicate strong hydrogen bonding with imidazolium cations. Accordingly, the N 1s orbital binding energy shifts toward the higher side as the side chain length of Amim<sup>+</sup> increases due to the increase in the alkyl chain attached to the N atom (Figure 3.3 C). The peak positions for C 1s were centered on 286.7 eV (redox state +1), for N 1s at 401.3 eV (redox state +1), and for Cl 2p<sub>3/2</sub> at 197.6 eV (redox state -1).

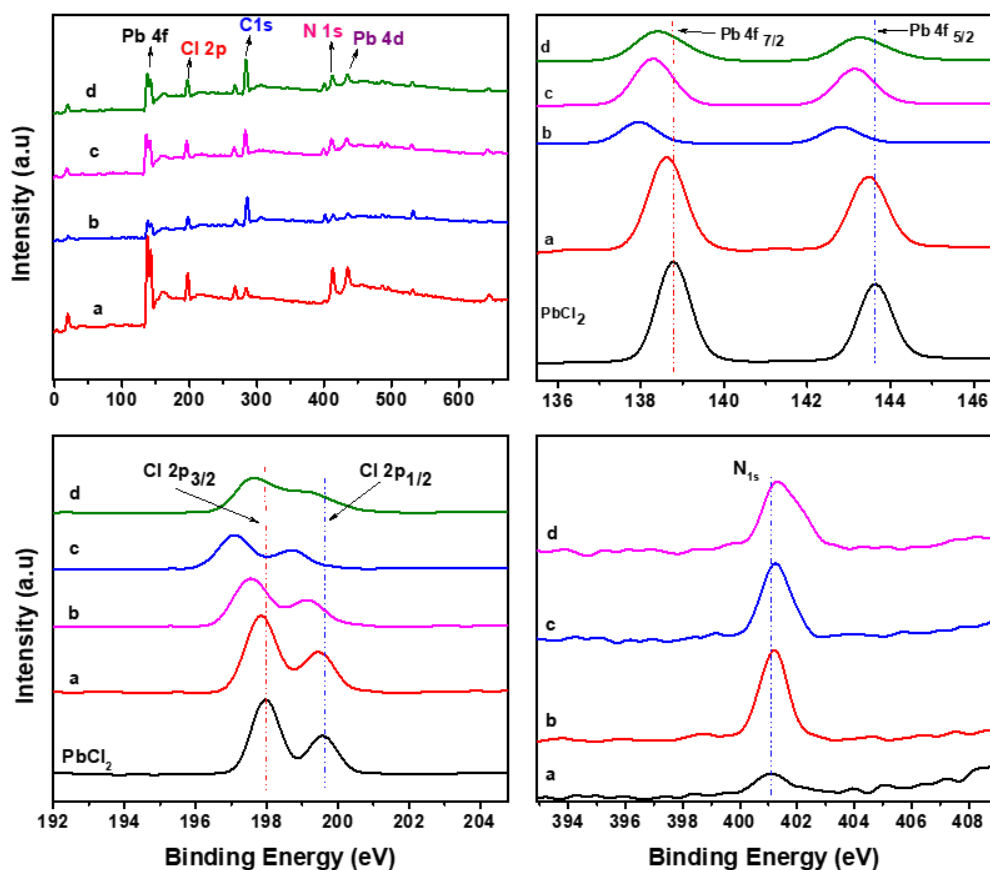


Figure 3.3. (A) shows survey scan spectrum and (B), (C) and (D) shows high resolution XPS spectra of Pb 4f, Cl 2p and N 1s region. In (A) – (D): (a) is MimCl-PbCl<sub>2</sub>, (b) is C<sub>2</sub>mimCl-PbCl<sub>2</sub>, (c) is C<sub>4</sub>mimCl-PbCl<sub>2</sub> and (d) is C<sub>6</sub>mimCl-PbCl<sub>2</sub>.

The crystalline nature of the materials was studied using X ray diffraction analysis.  $\text{PbCl}_2$  exist in orthorhombic (Figure 3.4B) form and the ILs are amorphous. The products exhibited well-defined peaks in the XRD. Figure 3.4A gives the XRD patterns of the raw materials and the synthesised products. The peaks corresponding to orthorhombic  $\text{PbCl}_2$  precursor material are absent/shifted in the products, XRD pattern indicating that  $\text{PbCl}_2$  have reacted with ILs. The XRD peak at  $2\theta$  of  $11^\circ$  is attributed to the ordered arrangement formed by the ILs.

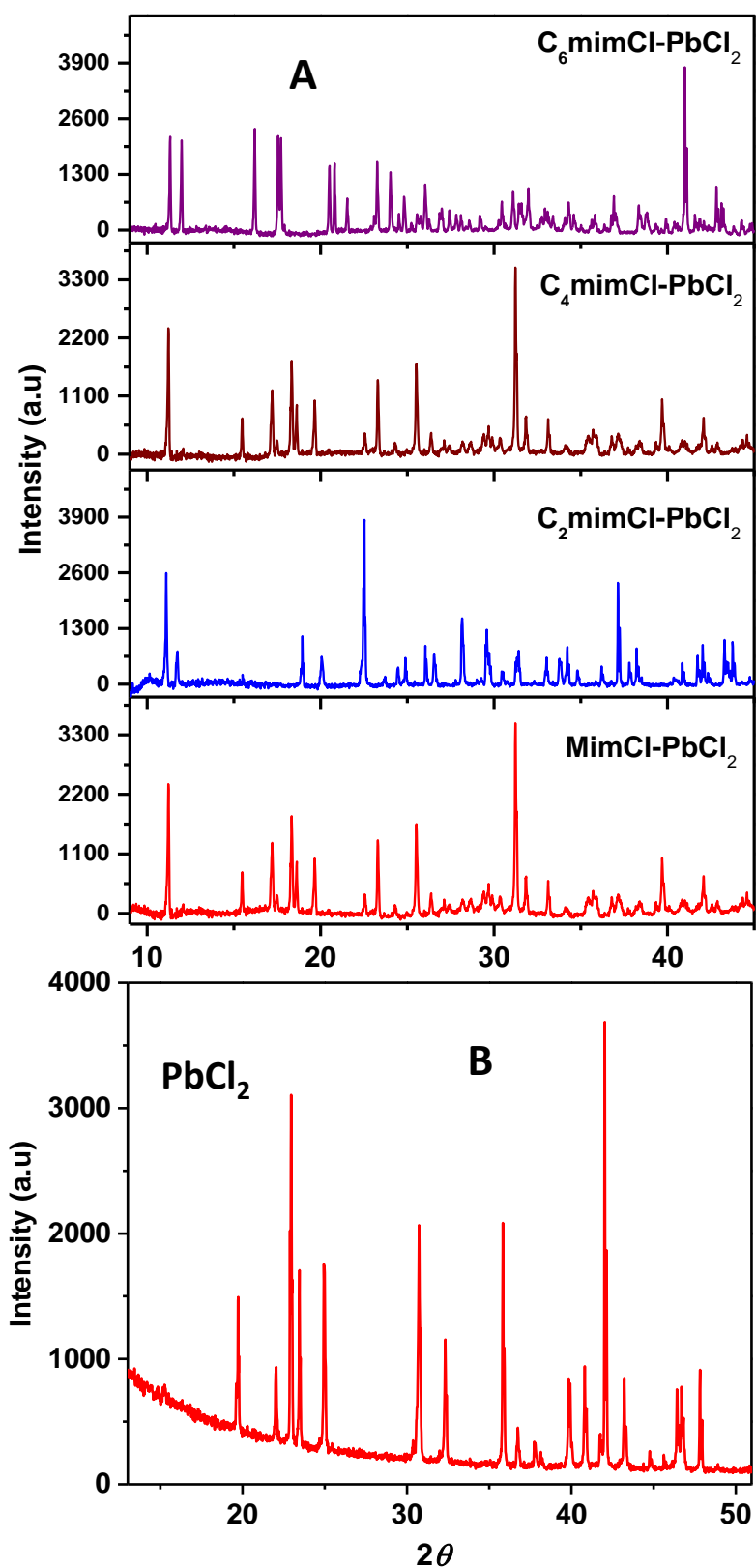


Figure 3. 4. (A) The XRD spectra of various ILs -  $\text{PbCl}_2$  systems. The names of the hybrid materials are given as Figure legend. (B) XRD pattern of  $\text{PbCl}_2$

Single crystal XRD could provide insight into the lattice information of the crystalline materials. Several trials have been made to grow the single crystals via the anti-solvent vapour assisted crystallisation method. A 0.1mM solution of PbCl<sub>2</sub> and C<sub>2</sub>mimCl was dissolved in DMF and kept in a closed vial for ~3 months without disturbing. The single crystals were grown in the DMF solvent and taken for characterisation. A photograph of single crystals grown from C<sub>2</sub>mimCl-PbCl<sub>2</sub> system and the arrangement of atom present in the crystal is represented in Figure 3.5 A and B, respectively. Table 3.2. shows the cell parameters elucidated from the single crystal XRD analysis. Figure 3.5A shows that C<sub>2</sub>mimCl-PbCl<sub>2</sub> exhibits 2D layered structure.

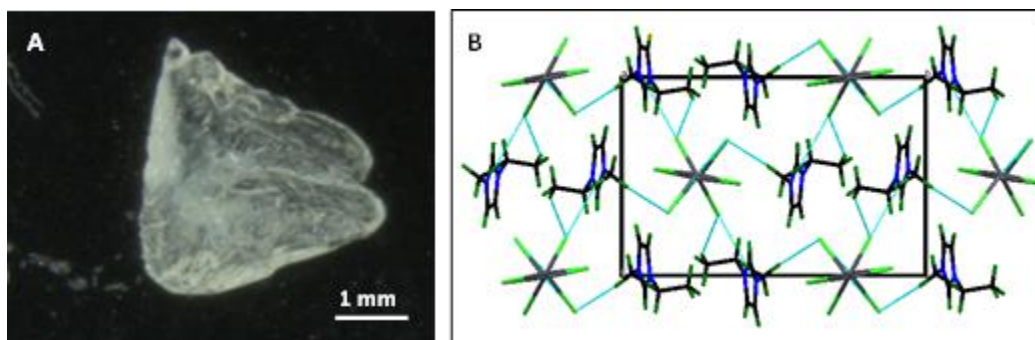


Figure 3.5 (A) Optical image of a single crystal of C<sub>2</sub>mimCl-PbCl<sub>2</sub>, (B) 2D layered structure of C<sub>2</sub>mimCl-PbCl<sub>2</sub> elucidated from single crystal XRD data

Table 3.2 Crystal structure data derived from single crystal analysis

<b>Empirical formula</b>	C <sub>6</sub> H <sub>11</sub> Cl <sub>3</sub> Pb N <sub>2</sub>
<b>Formula weight</b>	424.71 amu
<b>Temperature</b>	296(2) K
<b>Wavelength</b>	0.71073 Å
<b>Crystal system</b>	Orthorhombic
<b>Space group</b>	P 21 21 21

<b>Unit cell dimensions</b>	a = 8.1776(2)Å	$\alpha = 90^\circ$
	b = 15.03690(10) Å	$\beta = 90^\circ$
	c = 9.3948(3) Å	$\gamma = 90^\circ$
<b>Volume</b>	1155.24(5) Å <sup>3</sup>	

### 3.3.1.1 Conformations in the hybrid perovskite

Alkylmethylimidazoliumchloride (AmimCl) based ILs are known to (Bonamartini Corradi, Ferrari et al. 2001) possess rotational isomerism around the C<sub>7</sub>-C<sub>8</sub> bond of the Amim<sup>+</sup> cation. The monoclinic crystals correspond to *trans* (AA) and the orthorhombic crystal belongs to the *gauche* (GA) conformation. Hayashi and co-workers (Hayashi, Ozawa et al. 2003) have demonstrated that the *gauche* and *trans* conformers of [C<sub>4</sub>mim]<sup>+</sup> can be distinguished by Raman spectroscopy. The characteristic wavenumbers in the Raman spectra were 625 and 730 cm<sup>-1</sup> for the *trans* conformer and 500, 600 and 701 cm<sup>-1</sup> for the *gauche* conformer (Katayanagi, Hayashi et al. 2004) (Fig 3.6 B). In MimCl<sup>+</sup>, C<sub>7</sub> and C<sub>8</sub> bonds are absent, so rotational isomers do not exist. Peaks at 625 and 730 cm<sup>-1</sup> in C<sub>2</sub>mimCl-PbCl<sub>2</sub> and in C<sub>6</sub>mimCl-PbCl<sub>2</sub> confirms that the [C<sub>2</sub>mim]<sup>+</sup> and [C<sub>6</sub>mim]<sup>+</sup> are in *trans* conformation. In C<sub>4</sub>mimCl-PbCl<sub>2</sub>, [C<sub>4</sub>mim]<sup>+</sup> shows peaks corresponding to both *trans* and *gauche* conformers. Further, the conformation of C<sub>4</sub>mim in the minimum energy structures of *gauche* and *trans* coordinated systems are observed in the Raman spectral analysis. This reinforces the possibility for the coexistence of 1D strands and 2D layered structures. FTIR spectra also complement the results of Raman studies. The existence of *trans* conformer is complimented by the presence of peaks at 625 and ~700 cm<sup>-1</sup> in the FTIR spectrum (Figure 3.6B). The presence of the *gauche* conformer in C<sub>4</sub>mimCl-PbCl<sub>2</sub> is corroborated by 600 cm<sup>-1</sup> absorption peak. Further, computational studies proved the existence of *trans* conformer for C<sub>2</sub>mim<sup>+</sup> and C<sub>6</sub>mim<sup>+</sup> cations for the optimised structures (whereas both *gauche* and *trans* conformers are present in the C<sub>4</sub>mim<sup>+</sup> cations).

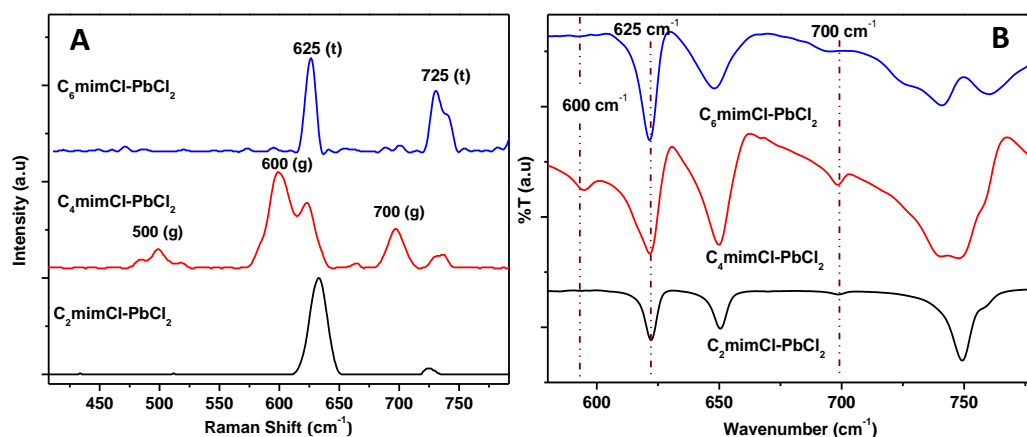


Figure 3.6 (A) represents the Raman spectra and (B) FTIR spectra showing the peaks corresponds to gauche (g) and trans (t) conformation of  $C_2\text{mimCl-PbCl}_2$ ,  $C_4\text{mimCl-PbCl}_2$  and  $C_6\text{mimCl-PbCl}_2$

The interaction of  $\text{PbCl}_2$  with different ILs was studied by computational chemistry methods using density functional theory (DFT). In the DFT method, electronic system energy is computed based on electron density calculation rather than wavefunction. The important advantage of using the electron density over wavefunction is that the dimensionality can be reduced. (see Figure 3.7). Major interaction sites involve C-H hydrogens attached to ring N atoms with terminal chloride ions of  $\text{PbCl}_2$ . The interaction distances range from 2.02 to 2.2 Å in  $\text{MimCl-PbCl}_2$  systems, which suggest strong hydrogen bonding present in the system. In the case of  $C_2\text{mimCl}$ , the interaction distances slightly elongated to the range from 2.15 to 2.33 Å. The angle of bridged chlorine atoms reduces  $\sim 5^\circ$ . When the alkyl chain length increases, the additional change in bond length is minimal. In parallel with the limited interactions of  $\text{PbCl}_2$  to  $C_4\text{H}$  of the alkyl chain, the interaction distances are similar in  $C_4\text{mim}$  and  $C_6\text{mim}$ . In all instances of minimum energy structures of the  $\text{PbCl}_2$ - ILs, the conformation of IL cation was in the *trans* form. In the case of 1-butyl-3-methylimidazolium-based ILs, gauche conformation was also modelled. The  $C_4\text{mimCl-PbCl}_2$  system with *trans* conformation was 10 kJ/mol more stable than the *gauche*  $C_4\text{mimCl-PbCl}_2$  system. Since the energy difference is minimal, it is inter-convertible and hence the presence of both the conformers in the Raman spectrum is rationalised (Figure 3.7 C and D).

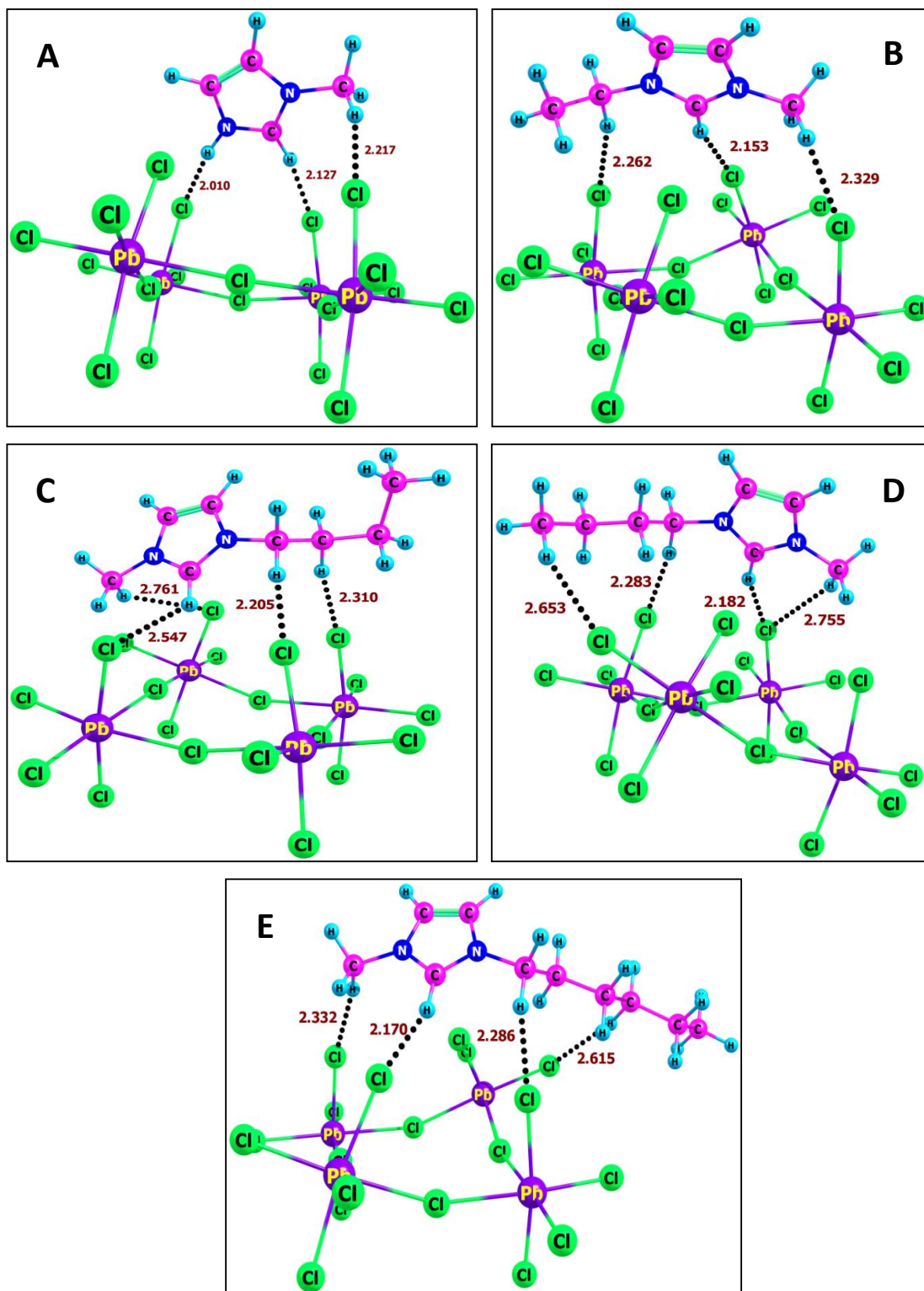


Figure. 3.7 Interaction of hexacoordinated  $\text{PbCl}_2$  with (A)  $\text{Mim}^+$ , (B)  $\text{C}_2\text{mim}^+$ , (D)  $\text{C}_4\text{mim}^+$  and (E)  $\text{C}_6\text{mim}^+$  cations and (C) interaction of pentacoordinated with  $\text{C}_4\text{mim}^+$ . These structures of the compounds were elucidated from Density Functional Theory (DFT) method

### 3.3.2 Morphological Characterisations

It is proved from the computational analysis that, unlike AmimCl, MimCl is having a highly acidic proton attached to the N atom and it forms a strong hydrogen bond with bridging chlorine atom. C<sub>2</sub>mimCl- PbCl<sub>2</sub>, C<sub>4</sub>mimCl- PbCl<sub>2</sub> and C<sub>6</sub>mimCl-PbCl<sub>2</sub> show layered morphologies as evident from AFM images (Figure 3.8 (1–8)). The AFM topography images show that the MimCl- PbCl<sub>2</sub> forming rod-shaped morphology is having a thickness of 0.1 μm. The rod shape morphology results from the prevalence of H-bonding interactions originating from the N atom of the imidazolium ring, promoting a linear growth. C<sub>2</sub>mimCl-PbCl<sub>2</sub> shows few layers having a thickness of (0.05–0.07 μm) and C<sub>4</sub>mimCl-PbCl<sub>2</sub> shows thickness of (0.06 μm). C<sub>6</sub>mimCl-PbCl<sub>2</sub> shows multiple layers stacked together and the total layer thickness reaches ~1 μm.

The TEM images of the materials were taken after dissolving in DMF (Figure 3.8 (9–12)). For MimCl-PbCl<sub>2</sub>, the particle size was in the range of (50–100 nm) which compliments the AFM topographic images. The TEM images depict the formation of layered structure for all ILs-PbCl<sub>2</sub> based organic/inorganic hybrid materials. The atomic fringes and the SAED patterns point represent the formation of the polycrystalline layered materials. The spectroscopic and micrograph data suggest that the crystals of lead chloride form distorted PbCl<sub>6</sub> octahedra, making the arrangement of 2D layers in a staggered manner. The alkylmethylimidazolium cations occupy the interlayer spacing and are linked to the adjacent inorganic layers via ionic interactions between the ‘-N<sup>+</sup>’ moieties and chloro ligands.

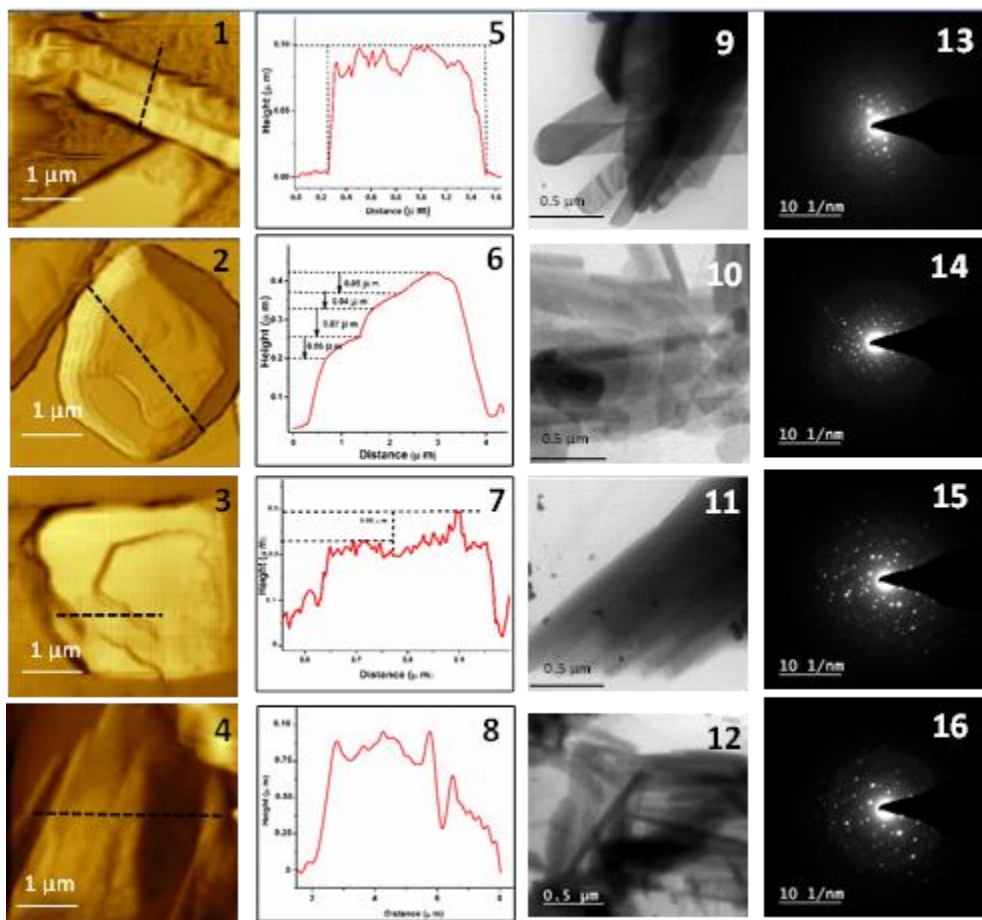


Figure 3.8. (1-4) : AFM images, (5-8) : height profile across the line drawn in Fig (1-4), (9-12) is the TEM images and (13–16) is SAED pattern of MimCl-PbCl<sub>2</sub>, C<sub>2</sub>mimCl-PbCl<sub>2</sub>, C<sub>4</sub>mimCl-PbCl<sub>2</sub> and C<sub>6</sub>mimCl-PbCl<sub>2</sub>, respectively.

### 3.3.3 Optical properties

The optical characterisation of the hybrid materials was conducted using UV–visible and fluorescence spectroscopy. ILs and PbCl<sub>2</sub> do not absorb in the range of 250–800 nm (Figure 3.9 A and B). However, unlike the precursors, the hybrid materials show absorption in the UV–visible range.

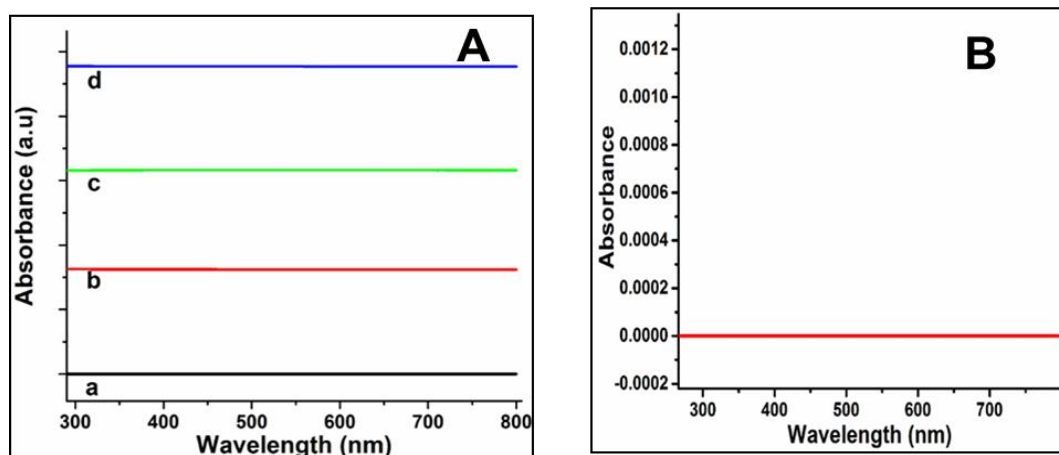


Figure 3.9 (A) shows UV-visible spectra (a) MimCl, (b) C<sub>2</sub>mimCl, (c) C<sub>4</sub>mimCl (d) C<sub>6</sub>mimCl and lead chloride, respectively. Absorption spectrum of PbCl<sub>2</sub> is given in (B).

MimCl-PbCl<sub>2</sub> shows a sharp absorption at 302 nm (Figure 3.10 A). The absorption of C<sub>2</sub>mimCl-PbCl<sub>2</sub> and C<sub>6</sub>mimCl-PbCl<sub>2</sub> at 345 nm confirms the existence of only hexacoordinated plumbate systems. This complements the observations from Raman and XRD spectral analysis.

In the case of C<sub>4</sub>mimCl, peaks observed at 320 nm and 345 nm are attributed to the pentacoordinated and hexacoordinated plumbate systems, respectively. Bandgaps were calculated from absorption edge appearing around 400 nm and it was in the range 3.0–3.3 eV for various ILs-PbCl<sub>2</sub> perovskites (Figure 3.10 A).

The photoluminescence (PL) spectra (Figure 3.10 B inset) were recorded by exciting the compounds with wavelengths ranging from 300 to 500 nm. The best emission was observed at 532 nm by excitation at 300 nm. All the materials showed luminescence and were having a large Stokes shift.

Charge carrier lifetime ( $\tau$ ) is one of the critical parameters that can influence the optoelectronic properties. To evaluate the lifetime ( $\tau$ ) of the excitons generated on exposure to light, time-correlated single-photon counting (TCSPC) studies were carried out (see Figure 3.10B). A bi-exponential fit with lifetimes of 10.7 ns (50% contribution) and 2.8 ns (50% contribution) is observed for MimCl-PbCl<sub>2</sub>. On the other hand, C<sub>2</sub>mimCl-PbCl<sub>2</sub>, C<sub>4</sub>mimCl-PbCl<sub>2</sub> and C<sub>6</sub>mimCl-PbCl<sub>2</sub>

gave tri-exponential fitted decay patterns attributed to three different exciton species. Lifetime of ~35 ns (90%), ~36 ns (~80%) and 38 ns (~93%) for the excitons in C<sub>2</sub>mimCl-PbCl<sub>2</sub>, C<sub>4</sub>mimCl-PbCl<sub>2</sub> and C<sub>6</sub>mimCl-PbCl<sub>2</sub>, respectively. Accordingly, the highest emission among the materials used in the present study was exhibited by C<sub>6</sub>mimCl-PbCl<sub>2</sub>.

A longer lifetime must be arising from the self-trapping of photogenerated carriers through excited-state-lattice distortions. Efficient charge separation and transportation can be expected in compounds with more open structures due to their stronger internal electric field caused by larger lattice distortion. The framework constituted by (PbCl<sub>6</sub>)<sup>4-</sup> octahedra is responsible for the longer life of the excited species. There will be slight distortions in the inorganic lattice of hybrid materials due to the difference in the organic cations, giving rise to change in the lifetime of the charge carriers.

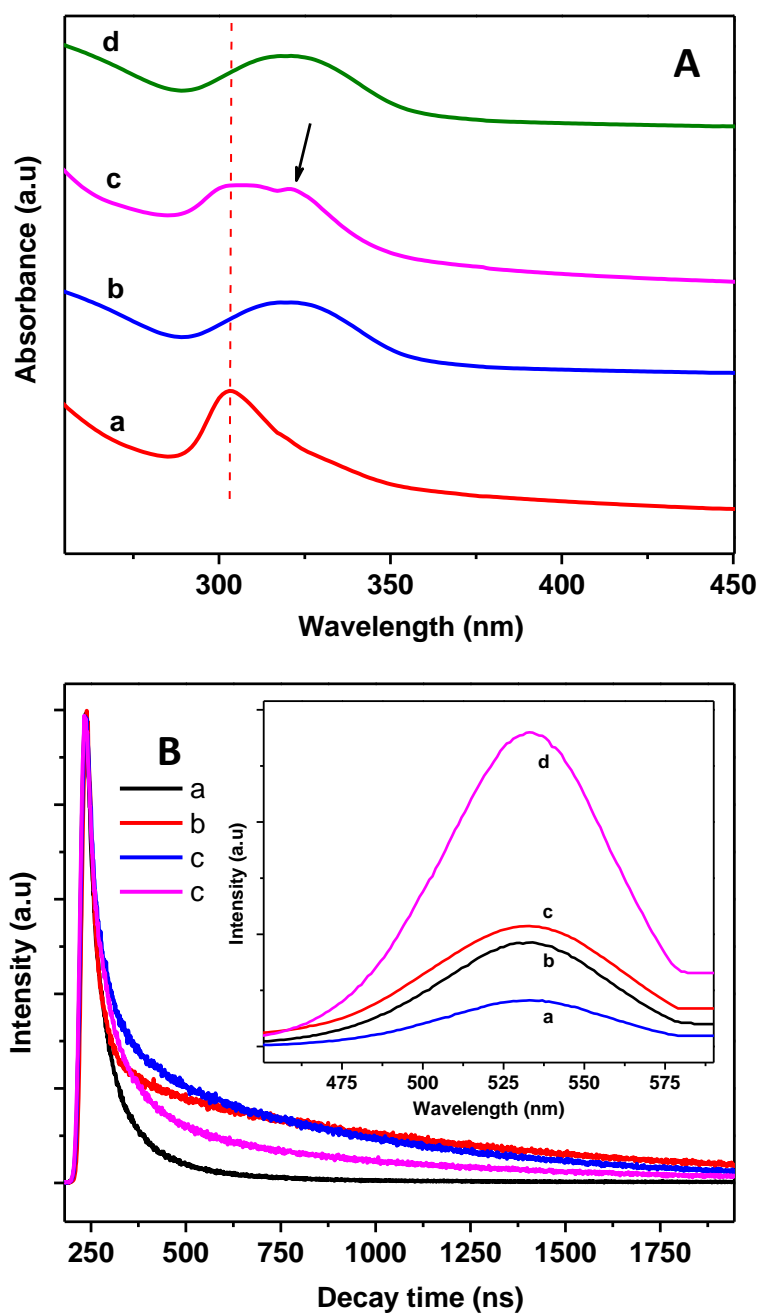


Figure 3. 10. (A) shows UV–visible absorption spectra and (B) shows lifetime curves of (a) MimCl- PbCl<sub>2</sub>, (b) C<sub>2</sub>mimCl-PbCl<sub>2</sub>, (c) C<sub>4</sub>mimCl-PbCl<sub>2</sub> and (d) C<sub>6</sub>mimCl-PbCl<sub>2</sub>. The UV–visible absorption spectra of the same ILs-PdCl<sub>2</sub> systems are given as the inset of (B)

The energy band diagram provides more profound perceptions of the charge transfer dynamics of these hybrid systems (see Figure 3.11 E). The cyclic voltammetry (CV) curves of the materials are shown in (Figure 3.11 A, B, C and

D). According to the onset potential of the reduction peaks, the lowest unoccupied molecular orbit (LUMO) and highest occupied molecular orbital (HOMO) are estimated and compiled in Table 3.3 show the HOMO and LUMO levels of the materials.

Table 3.3 HOMO and LUMO levels of the hybrid perovskite materials

<b>Sample name</b>	<b>HOMO (eV)</b>	<b>LUMO (eV)</b>
MimCl-PbCl <sub>2</sub> ,	-6.29	-2.89
C <sub>2</sub> mimCl-PbCl <sub>2</sub>	-7.15	-3.95
C <sub>4</sub> mimCl-PbCl <sub>2</sub>	-7.06	-3.96
C <sub>6</sub> mimCl-PbCl <sub>2</sub>	-7.14	-3.94

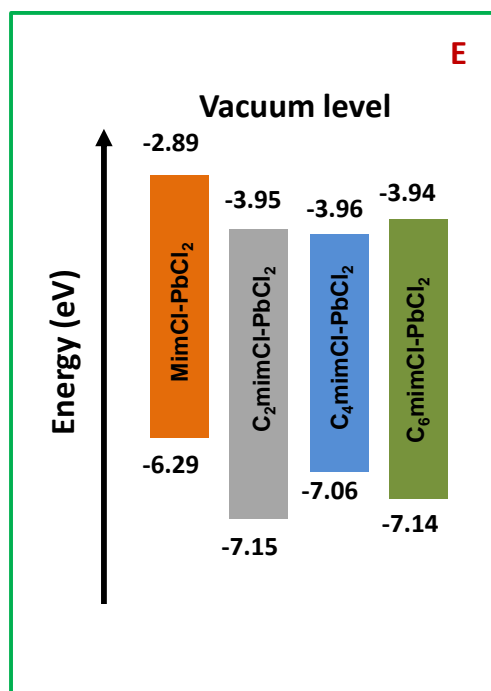
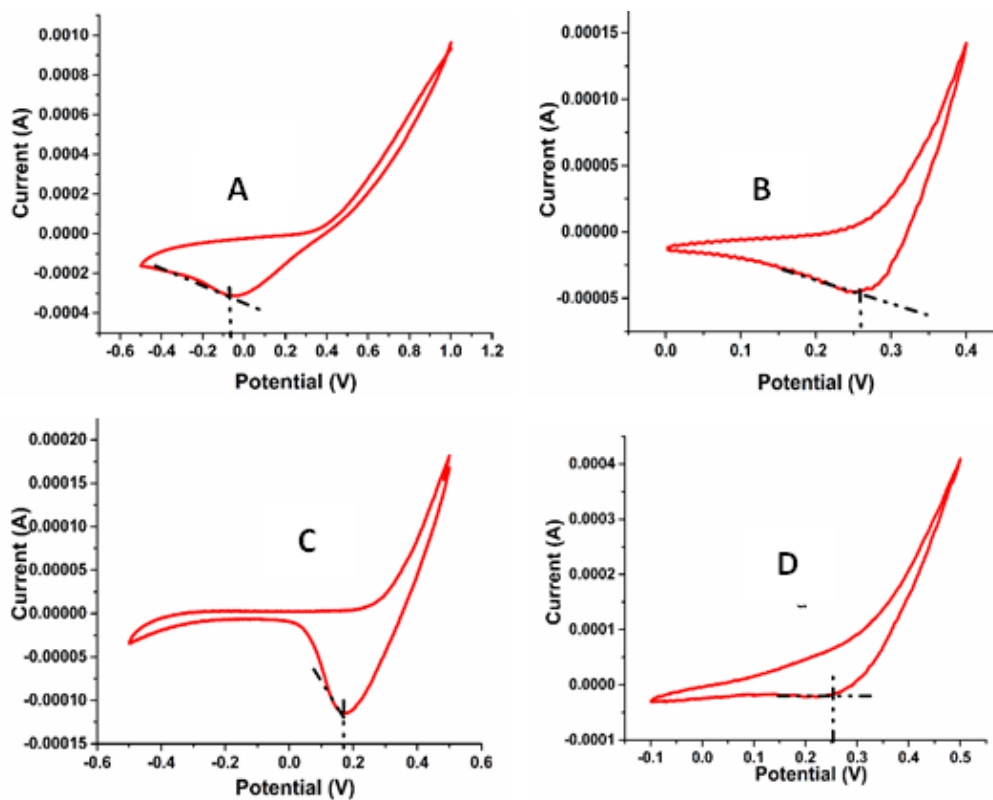


Figure 3. 11 (A), (B), (C) and (D) represents cyclic voltammetry curve and (E) energy band diagram of (a) MimCl- PbCl<sub>2</sub>, (b) C<sub>2</sub>mimCl-PbCl<sub>2</sub>, (c) C<sub>4</sub>mimCl-PbCl<sub>2</sub> and (d) C<sub>6</sub>mimCl-PbCl<sub>2</sub> respectively.

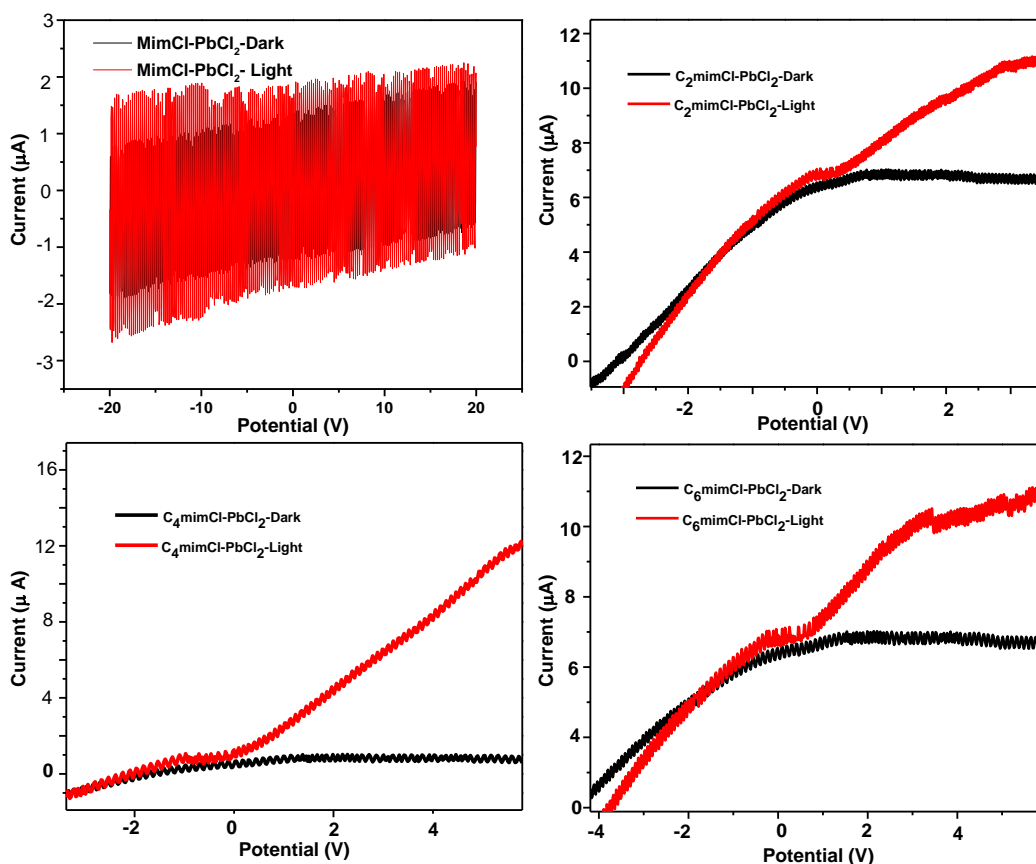


Figure 3.12 Dark and light current measured for MimCl- PbCl<sub>2</sub>, C<sub>2</sub>mimCl-PbCl<sub>2</sub>, C<sub>4</sub>mimCl-PbCl<sub>2</sub> and C<sub>6</sub>mimCl-PbCl<sub>2</sub>

### 3.3.4. Photoconductivity studies

Photoconductivity of the materials was measured in the absence (dark) and in the presence of light (see Figure 3.12). While MmimCl-PbCl<sub>2</sub> did not show any appreciable photocurrent, the other three materials exhibited photocurrent in the range of 1–10 μA. Comparing with the dark current, the photocurrent intensity was higher (μA), indicating that more electron-hole pairs are generated/excited by the photon irradiation. It is also clear that photocurrent and the dark current increase with the voltage as more electron-hole pairs are separated by the increase of electric field intensity.

### 3.3.4 Thermal Properties

The thermogram of all the present hybrid perovskite materials exhibits a multiple-step decomposition pattern (Figure 3.13A). The thermal decomposition of  $\text{MimCl-PbCl}_2$  starts at  $\sim 230^\circ\text{C}$ , corresponding to the decomposition of  $\text{MimCl}^+$ . It also shows a three-step decomposition pattern, while the other three systems showed a two-step decomposition. The onset of decomposition in  $\text{C}_4\text{mimCl-PbCl}_2$  and  $\text{C}_6\text{mimCl-PbCl}_2$  is around  $350^\circ\text{C}$ , starting from the decomposition of ILs. The second stage decomposition starting at  $\sim 580^\circ\text{C}$  corresponds to the decomposition of  $\text{PbCl}_2$ .

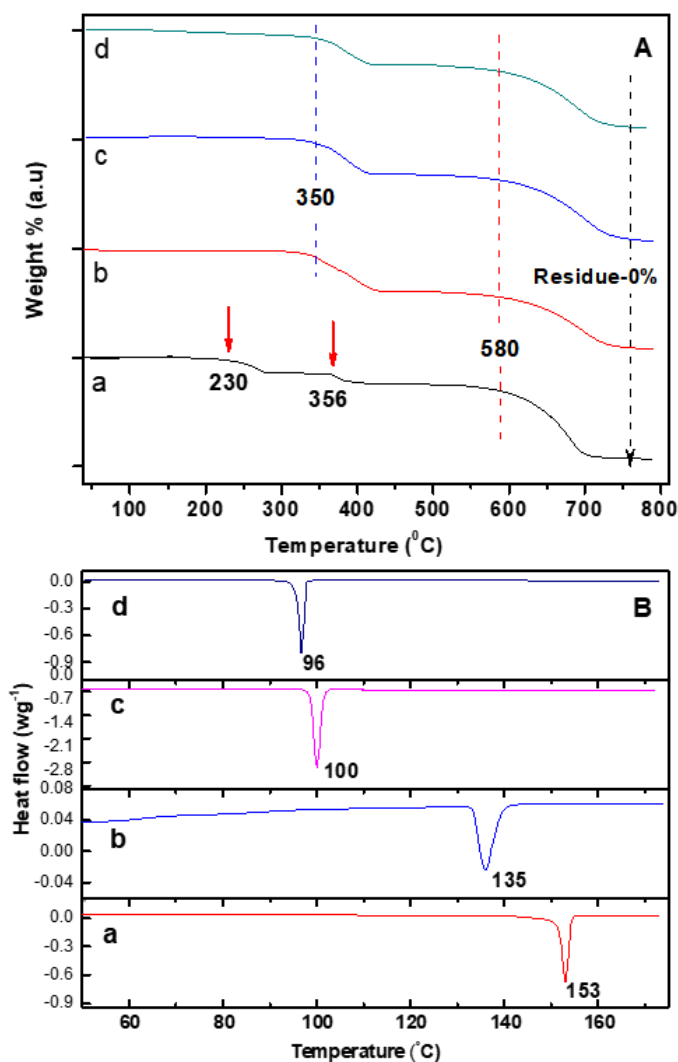


Figure 3. 13. (A) shows TGA and (B) shows DSC curves of (a)  $\text{MimCl-PbCl}_2$ , (b)  $\text{C}_2\text{mimCl-PbCl}_2$  (c)  $\text{C}_4\text{mimCl-PbCl}_2$  and (d)  $\text{C}_6\text{mimCl-PbCl}_2$

The differential scanning calorimetry (DSC) curve exhibits endothermic transitions due to melting followed by phase transition (Figure 3.13B). As the chain length of the imidazolium part increases, the melting point falls from  $\sim 153$  °C (Figure 3.13B) to lower values as the long-range order is disturbed.

It is noteworthy that, unlike other reported compounds of lead,  $C_2mimCl-PbCl_2$ ,  $C_4mimCl-PbCl_2$  and  $C_6mimCl-PbCl_2$  show 2D layered morphology and they are not hygroscopic. The non-hygroscopic nature can be inferred by comparing the FTIR spectra of the  $-OH$  region, taken after one month of synthesis and storage under ambient conditions (Figure 3.14). The  $-OH$  absorption peaks characteristic moisture has not appeared in the IR spectra of new materials after one month. These are very interesting attributes, highly desirable for their application in optoelectronic devices.

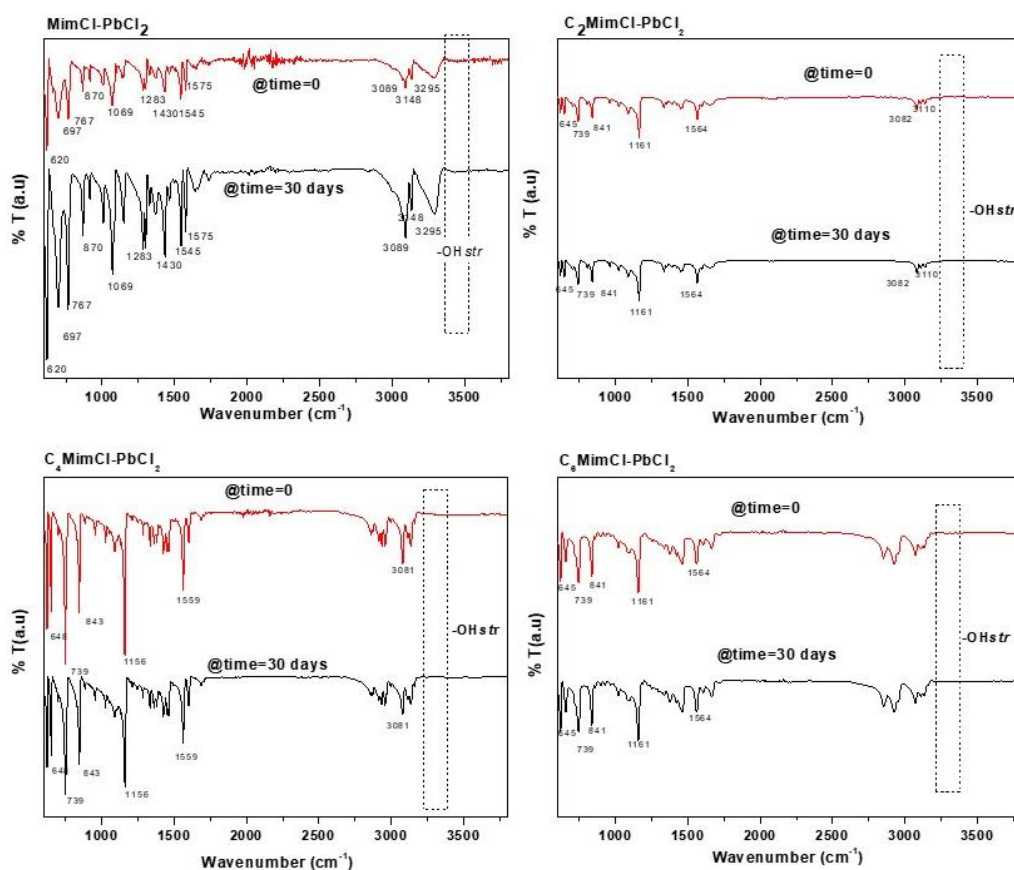


Figure 3.14. FTIR spectra of MimCl- PbCl<sub>2</sub>, C<sub>2</sub>mimCl-PbCl<sub>2</sub>, C<sub>4</sub>mimCl-PbCl<sub>2</sub> and C<sub>6</sub>mimCl-PbCl<sub>2</sub> after storage at ambient conditions for 1 months. Important peaks and the  $-OH$  stretching region is marked.

### 3. 4. Conclusions

A new series of imidazolium-based ILS-PbCl<sub>2</sub> compounds belonging to the family of 2D hybrid perovskites were synthesised and characterised. The detailed spectroscopic and microscopic analysis suggest that MimCl-PbCl<sub>2</sub>, C<sub>2</sub>mimCl-PbCl<sub>2</sub> and C<sub>6</sub>mimCl-PbCl<sub>2</sub> form a 2D structure while C<sub>4</sub>mimCl-PbCl<sub>2</sub> was forming two different 2D and 1D structures. The interaction sites and possible structures were predicted by theoretical methods were in good agreement with experimental results. AFM and TEM confirmed layered morphology of ILS-PbCl<sub>2</sub> systems. C<sub>2</sub>mimCl-PbCl<sub>2</sub>, C<sub>4</sub>mimCl-PbCl<sub>2</sub> and C<sub>6</sub>mimCl-PbCl<sub>2</sub> yielded good emission properties as well as longer exciton lifetimes. C<sub>2</sub>mimCl-PbCl<sub>2</sub>, C<sub>4</sub>mimCl-PbCl<sub>2</sub> and C<sub>6</sub>mimCl-PbCl<sub>2</sub> showed superior thermal and environmental stability. The systems exhibited a bandgap of 3.0-3.30 eV. Photocurrent measurement suggests the suitability of the synthesised compounds as light absorber material for optoelectronic applications.



## CHAPTER 4

# DYE-SENSITISED METHYLAMMONIUM LEAD BROMIDE PEROVSKITE: SYNTHESIS, CHARACTERISATION AND EVALUATIONS

### 4.1 Introduction

Methylammonium lead iodide ( $\text{MAPbI}_3$ ) is the most popular hybrid perovskite, investigated for photovoltaic applications (Roldán-Carmona, Malinkiewicz et al. 2014). However, due to its high sensitivity to moisture and poor environmental stability, researchers are looking for more stable systems to achieve better long term performance (Niu, Guo et al. 2015). Among the halide perovskites, methylammonium lead bromide ( $\text{CH}_3\text{NH}_3\text{PbBr}_3$ ) is more stable as the bromide anion has a smaller Bohr radius and higher binding energy compared to the iodide based perovskites (Sheng, Ho-Baillie et al. 2015). However, a higher bandgap of bromide anion is a major limiting factor for its application in solar cells. Composition engineering to tune the bandgap of the halide based perovskites could be a possible solution (Albero, Asiri et al. 2016). Supramolecular compounds have been used to improve the optoelectronic properties and stability of halide perovskites (Gao, Ji et al. 2021). Perovskite films have been treated with organic halide salts such as phenethylammonium iodide for the passivation of surface defects and suppress the non-radiative recombinations (Zhuang, Mao et al. 2019). Additives such as thiophene, ammonium halides, potassium salts, chloronaphthalene, ammonium chloride,  $\gamma$ -butyrolactone, etc. are also employed to improve/fine-tune the properties (Dubey, Adhikari et al. 2018; Zhang and Zhu 2020). Successful utilisation of dyes to co-sensitise and enhance the light absorption capability of perovskites is also reported (Kakiage, Aoyama et al. 2014). (McFarlane, De Castro et al. 2019).

This chapter investigates interactions between the di-tetrabutylammonium cis-bis(isothiocyanato)bis(2,2'-bipyridyl-4,4'-dicarboxylato)-ruthenium(II) (N719 dye) and methylammonium lead bromide perovskite. N 719

is a popular ruthenium-based organometallic dye that has been widely used in dye sensitised solar cells, offering superior performance (Portillo-Cortez, Martínez et al. 2019). The effect of the dye on the crystal structure, morphology and optical properties of the perovskite was evaluated. This study contributes to the fundamental understanding of the interactions between dye molecules and halide perovskite materials, which can benefit the studies and applications in the pertinent area.

## 4.2 EXPERIMENTAL

### 4.2.1 Materials and Synthesis

An equimolar ratio of  $\text{CH}_3\text{NH}_3\text{Br}$  and  $\text{PbBr}_2$  is dissolved in DMF (Weber 1978). Dye was dissolved in DMF solution at concentrations ranging from 0.2-1.5 ppm and added to the perovskite solution at 30 °C, under magnetic stirring. The clear solution obtained was evaporated under vacuum at 90 °C for 30 minutes. Orange-brown crystals obtained were characterised. To remove the solvent, the crystals were washed with toluene to remove any unreacted  $\text{CH}_3\text{NH}_3\text{Br}$  and dried under vacuum at 60 °C.

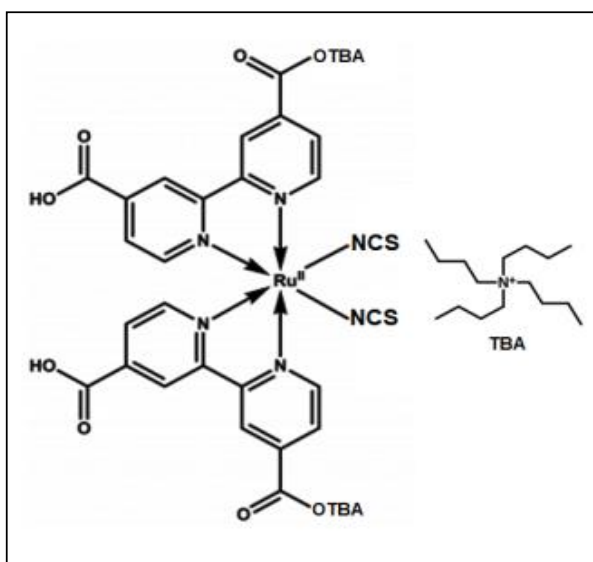


Figure 4.1 Structure of N719 dye

## 4. 3 RESULTS AND DISCUSSION

### 4.3.1 Structural Properties

The synthesised perovskite material is characterised by various spectroscopic and microscopic methods. The results were systematically analysed. The FTIR absorption peaks corresponding to  $\text{-NCS}$  and  $\text{C=O}$  of N 719 are observed at  $2100\text{ cm}^{-1}$  and  $1701\text{ cm}^{-1}$ , respectively. Peaks at  $1371\text{ cm}^{-1}$  and  $1231\text{ cm}^{-1}$  are attributed to  $\text{-COO}$  stretching and  $\text{C-O}$  stretching of dye molecule (Hirose, Shikaku et al. 2010). All the peaks corresponding to  $\text{-CH}$  and  $\text{-NH}$  vibrational modes are observed in the IR spectrum of both  $\text{CH}_3\text{NH}_3\text{PbBr}_3$  and dye-sensitised  $\text{CH}_3\text{NH}_3\text{PbBr}_3$ . No peak shifts are observed in the absorptions for  $\text{-NCS}$  and  $\text{-COOH}$  groups in dye sensitised  $\text{CH}_3\text{NH}_3\text{PbBr}_3$ . These observations confirm that there is no chemical interaction with the dye and perovskite molecule. (Figure 4.2).

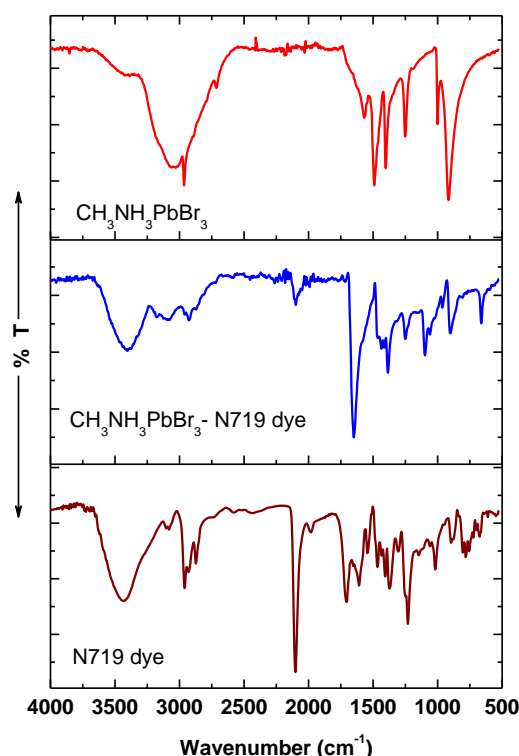


Figure. 4.2. FTIR spectra of N719 dye,  $\text{CH}_3\text{NH}_3\text{PbBr}_3$  and the dye sensitised  $\text{CH}_3\text{NH}_3\text{PbBr}_3$

The crystal structure of the perovskite and the dye-sensitised perovskite have been investigated using powder XRD and single crystal XRD analysis. The major planes of  $\text{CH}_3\text{NH}_3\text{PbBr}_3$  i.e. (100) and (200) are unaltered in dye sensitised  $\text{CH}_3\text{NH}_3\text{PbBr}_3$  proves that there is no crystal structure deviation observed after dye sensitization (Ding, Zhao et al. 2017). Crystal structure of both  $\text{CH}_3\text{NH}_3\text{PbBr}_3$  and dye sensitised  $\text{CH}_3\text{NH}_3\text{PbBr}_3$  shows cubic geometry (Ref: JCPDS file no. 00-010-0737). The presence of N 719 dye has not influenced the original crystal structure and morphology of the perovskite (Figure 4.3A).

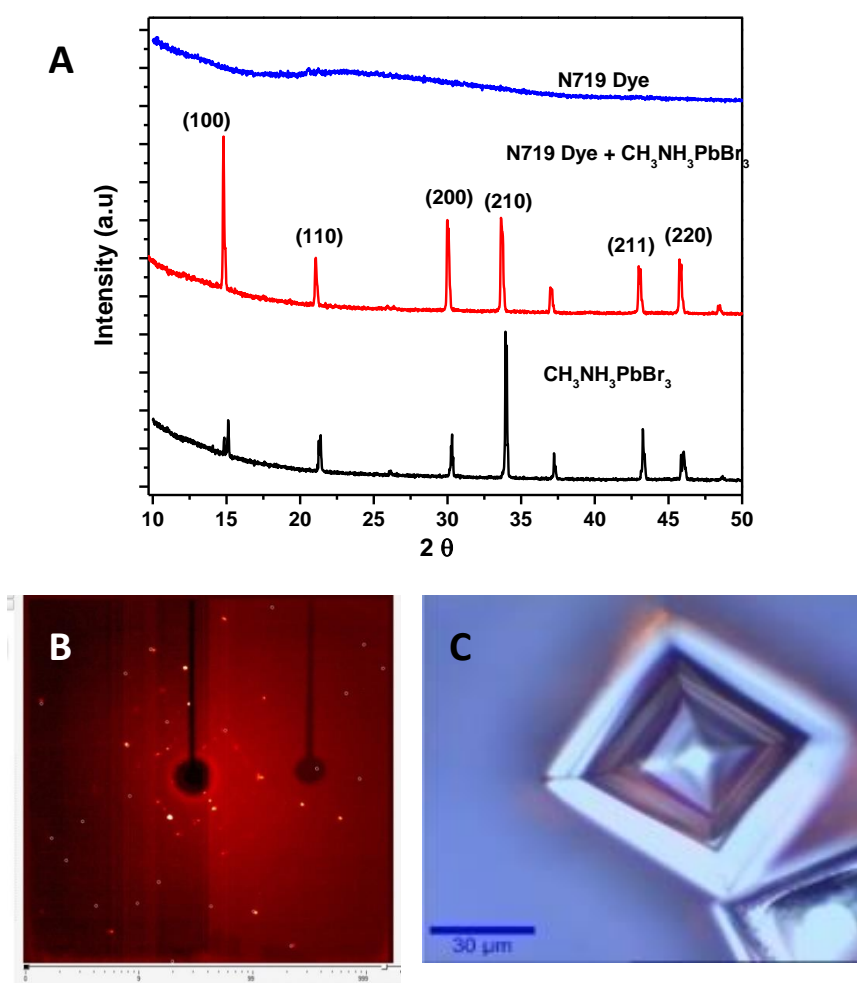


Figure. 4.3. (A) XRD pattern of dye,  $\text{CH}_3\text{NH}_3\text{PbBr}_3$  and dye sensitised  $\text{CH}_3\text{NH}_3\text{PbBr}_3$ , (B) single crystal XRD reflections of dye sensitised  $\text{CH}_3\text{NH}_3\text{PbBr}_3$  and (C) Optical image of single crystal of dye sensitised  $\text{CH}_3\text{NH}_3\text{PbBr}_3$

Table 4.1 Unit cell parameters derived from single crystal XRD reflection of N 719 dye +  $\text{CH}_3\text{NH}_3\text{PbBr}_3$

Empirical formula	$\text{CH}_3\text{NH}_3\text{PbBr}_3$	
Temperature	296(2) K	
Wavelength	0.71073 Å	
Crystal system	Cubic	
Space group	P	
Unit cell dimensions	a= 5.93 Å b= 5.93 Å b= 5.93 Å	$\alpha= 90^\circ$ $\beta= 90^\circ$ $\gamma= 90^\circ$
Volume	209 Å <sup>3</sup>	

The chemical state of the Ru in the dye before and after the incorporation into the perovskite structure has been evaluated using XPS analysis. XPS analysis of the dye sensitised  $\text{CH}_3\text{NH}_3\text{PbBr}_3$  also aimed to examine the oxidation state of Pb. Binding energies of Ru ( $3d_{3/2}$  and  $3d_{5/2}$ ) is (280.8 eV & 284.0 eV) and Pb ( $4f_{7/2}$  and  $4f_{5/2}$ ) is (138.80 eV & 146.66 eV), respectively. From the XPS spectra (Figure 4.3), it is clear that there is no change in the binding energy with respect to the 4f orbitals of Pb and 3d orbital of Ru in dye +  $\text{CH}_3\text{NH}_3\text{PbBr}_3$ . This observation confirms that no chemical reaction takes place between dye and  $\text{CH}_3\text{NH}_3\text{PbBr}_3$  molecule.

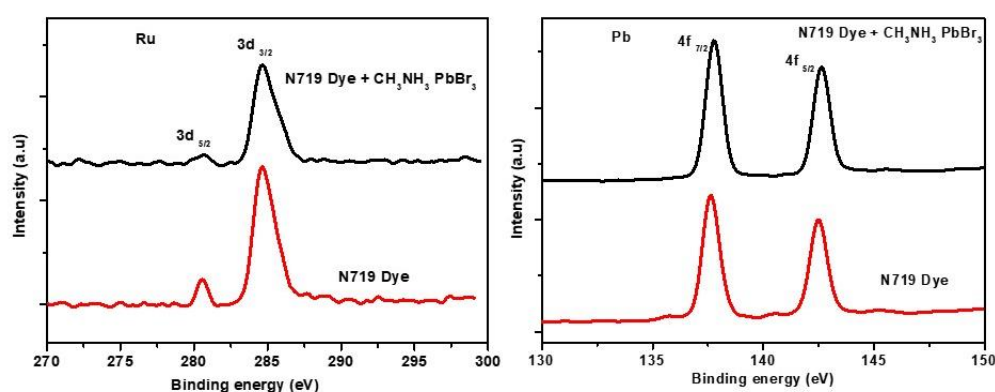


Figure. 4.4 (A) High-resolution XPS spectra showing the 3d orbital of Ru and (B) 4f orbital of Pb

The probable interaction between the dye molecule and MAPbBr<sub>3</sub> was simulated using computational analysis to validate the experimental results. The structure was optimised using PM6 level of the semi-empirical method. The semi-empirical method was chosen because of the non-availability of the basis set for heavy atoms like ruthenium. The interaction sites were studied from the optimized structure. Two carboxylate anions are present in the 2, 2'-bipyridyl-4,4'-dicarboxylato ligand of the N719 dye molecule. It forms hydrogen bonds between the di-tetrabutylammonium cations (proton of the butyl chain) with a bond distance is (~1.787 Å & 1.763 Å) and (1.890 Å & 1.809 Å). See Figure 4.5A.

In N 719 + MAPbBr<sub>3</sub> molecule, the corresponding bond length increased to (1.903 Å & 2.033 Å) and (1.919 & 2.084 Å). The increase in bond length can be attributed to the modification of molecular arrangement in the N719 dye due to the presence of MAPbBr<sub>3</sub>. As the bond length increases, energy decreases and there will be a shift in wavelength towards the lower region in the IR spectrum. This observation was proved by IR analysis, as there is a shift in –OH stretching peaks to lower wavelength in N719 + MAPbBr<sub>3</sub>.

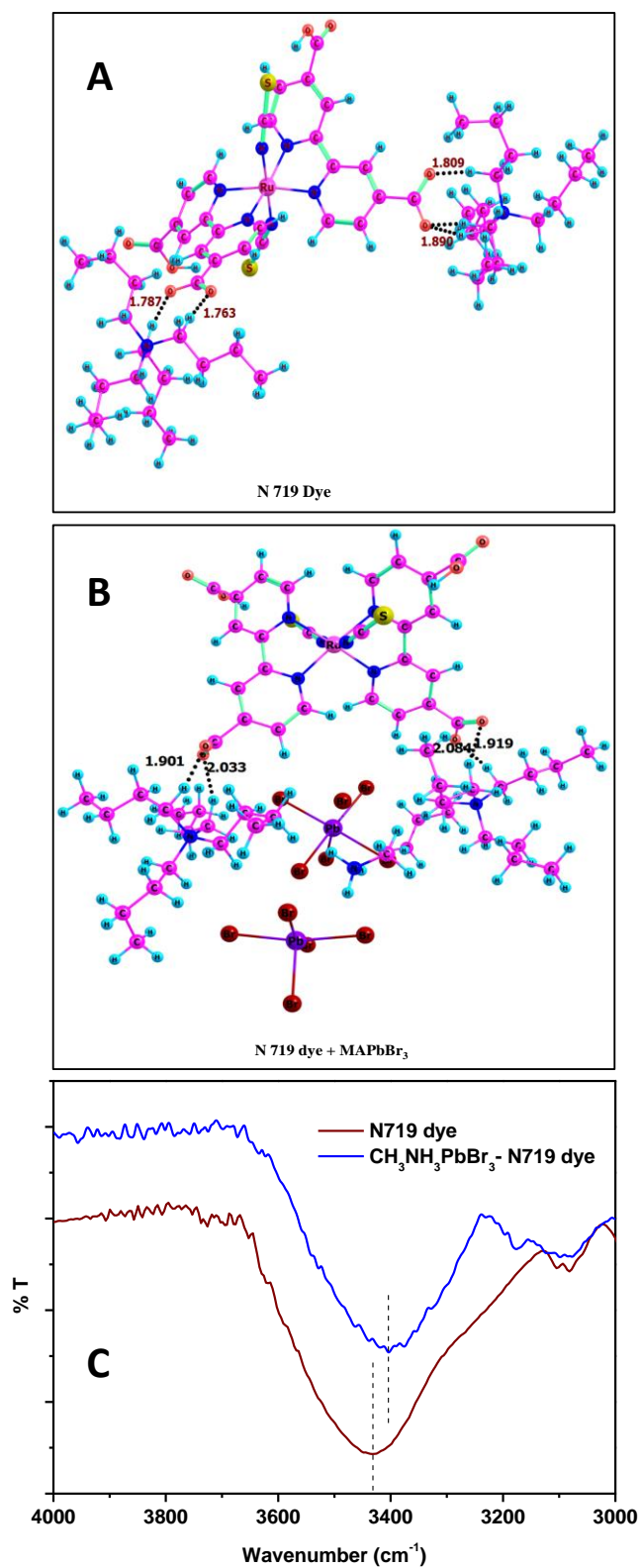


Figure. 4.5 (A) and (B) shows the optimised structure obtained from computational analysis using PM6 level of semi-empirical method and (C) Zoomed region of -OH stretching peak observed in FTIR spectra

### 4.3.2 Optical Properties

$\lambda_{\max}$  of MAPbBr<sub>3</sub> is slightly shifted to higher wavelength in dye + CH<sub>3</sub>NH<sub>3</sub>PbBr<sub>3</sub> Figure 4.6A. The PL emission of CH<sub>3</sub>NH<sub>3</sub>PbBr<sub>3</sub> is at 545nm, additional peaks observed at ~575 and 690 nm in dye + MAPbBr<sub>3</sub> are attributed to changes in energy level. This may be due to the defect state present in the composite. The energy band diagram of dye + MAPbBr<sub>3</sub> reveals a shift in the HOMO and LUMO levels facilitating electron transfer mechanisms.

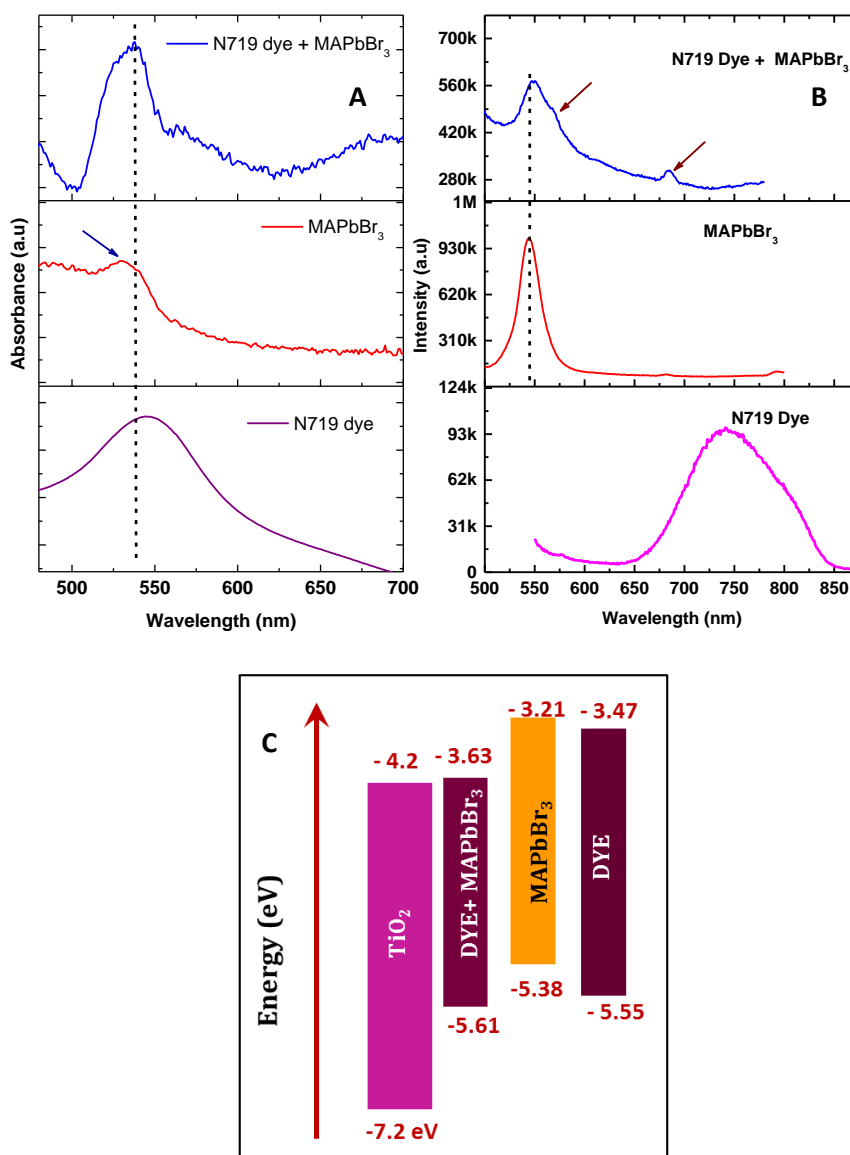


Figure. 4.6 (A) UV-visible spectra, (B) Photoluminescence spectra of CH<sub>3</sub>NH<sub>3</sub>PbBr<sub>3</sub> and dye + CH<sub>3</sub>NH<sub>3</sub>PbBr<sub>3</sub> and (C) Energy band diagram of CH<sub>3</sub>NH<sub>3</sub>PbBr<sub>3</sub> and dye + CH<sub>3</sub>NH<sub>3</sub>PbBr<sub>3</sub>

### 4.3.3 Morphological Properties

The morphological characterisation is performed using SEM images. SEM images given in Figure 4.7 show a cube like morphology for dye +  $\text{CH}_3\text{NH}_3\text{PbBr}_3$ . The  $\text{CH}_3\text{NH}_3\text{PbBr}_3$  show irregular morphology and shape (Figure 4.7A). The crystal shape is getting altered while collecting the image as it interacts with the electron beam. However, the dye+ $\text{CH}_3\text{NH}_3\text{PbBr}_3$  crystals did not change their shape, proving their stability towards the electron beam.

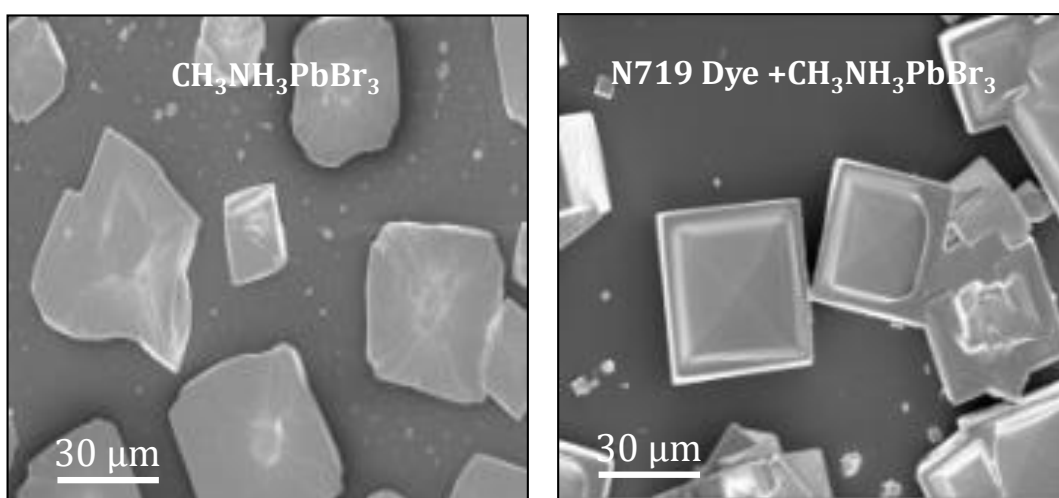


Figure. 4.7 (A) FE-SEM images of  $\text{CH}_3\text{NH}_3\text{PbBr}_3$  and dye +  $\text{CH}_3\text{NH}_3\text{PbBr}_3$

The TEM images and SAED pattern of dye+ $\text{CH}_3\text{NH}_3\text{PbBr}_3$  and  $\text{CH}_3\text{NH}_3\text{PbBr}_3$  are shown in Figure 4.8. From the SAED pattern, the  $d$ -spacing of (200) plane of dye +  $\text{CH}_3\text{NH}_3\text{PbBr}_3$  was calculated. The values are found to be comparable for dye +  $\text{CH}_3\text{NH}_3\text{PbBr}_3$  and  $\text{CH}_3\text{NH}_3\text{PbBr}_3$ . This observation further supports that dye did not affect the perovskite crystal structure.

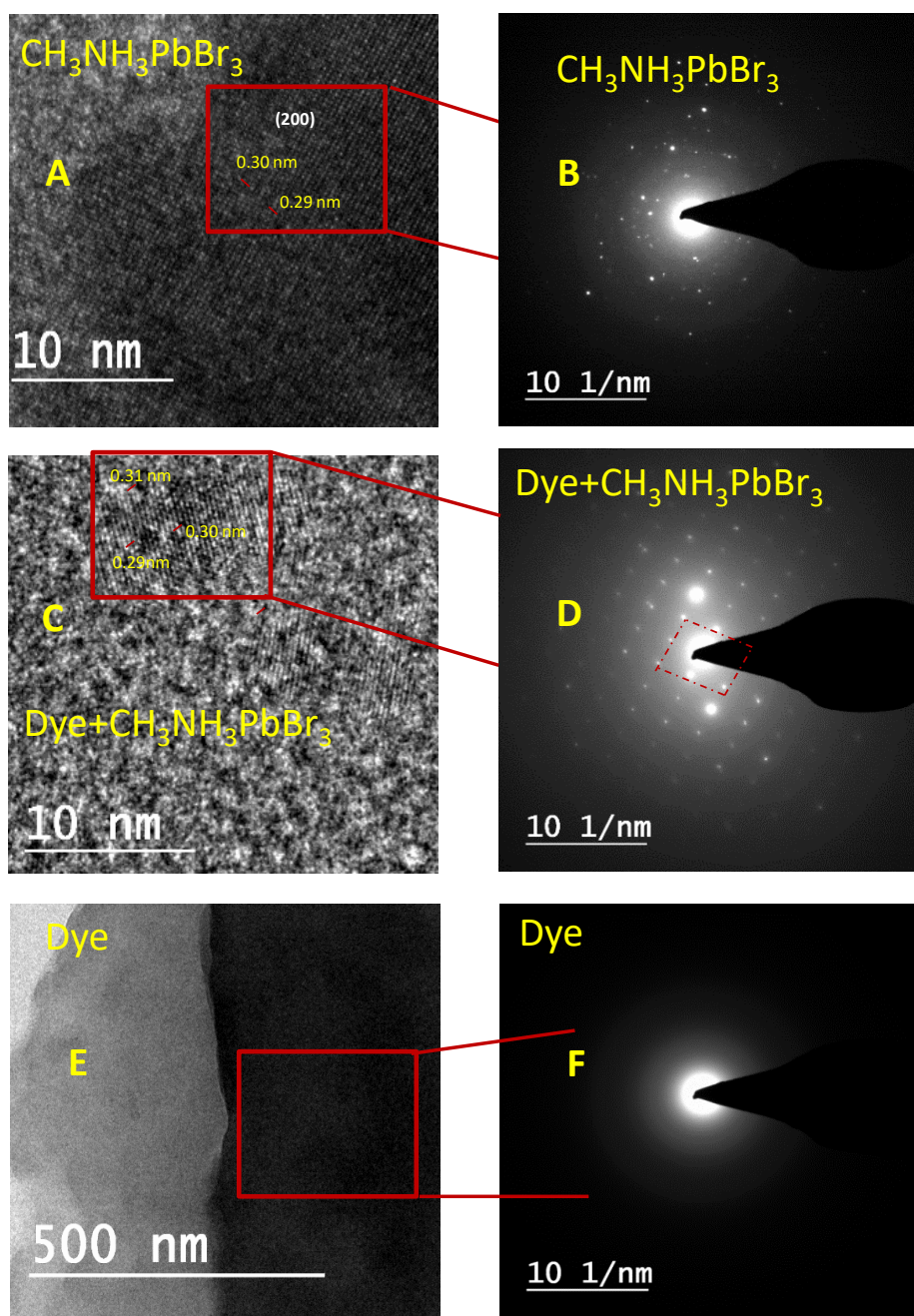


Figure 4.8 (A), (C) and (E) are the HR-TEM Images and (B), (D) and (F) shows the SAED patterns of  $\text{CH}_3\text{NH}_3\text{PbBr}_3$ , N 719 dye +  $\text{CH}_3\text{NH}_3\text{PbBr}_3$  and N719 dye, respectively

## 4.4. Conclusions

$\text{CH}_3\text{NH}_3\text{PbBr}_3$  perovskites were sensitised with N 719 dye to realise stable perovskite materials with improved optical properties. Crystal structure of N719 dye sensitised  $\text{CH}_3\text{NH}_3\text{PbBr}_3$  shows 3D cubic perovskite structure. The crystal

parameters of  $\text{CH}_3\text{NH}_3\text{PbBr}_3$  did not change in the N719 dye +  $\text{CH}_3\text{NH}_3\text{PbBr}_3$ , as evidenced from single crystal XRD analysis and HR-TEM. The dye molecule forms good physical interactions with the perovskite crystal, as observed from the FTIR analysis. Interaction of the dye molecule with  $\text{CH}_3\text{NH}_3\text{PbBr}_3$  has also been studied using the computational method. Dye sensitized  $\text{CH}_3\text{NH}_3\text{PbBr}_3$  shows changes in the UV-Visible absorption and the fluorescence emission properties indicating changes in HOMO-LUMO energy levels in dye sensitized  $\text{CH}_3\text{NH}_3\text{PbBr}_3$ . Thus a new and simple approach to improve the properties of the  $\text{CH}_3\text{NH}_3\text{PbBr}_3$  is demonstrated.



# CHAPTER 5

## ENVIRONMENTALLY STABLE TIN-HALIDE PEROVSKITES: OLIGOMER MEDIATED SYNTHESIS AND CHARACTERISATION

### 5. 1 Introduction

Lead based perovskites are well studied for solar cell applications (Boix, Agarwala et al. 2015). Even though lead-based perovskites are showing good photovoltaic performance, the toxicity of lead is a crucial inhibiting factor. Poor environmental stability of perovskites further complicates their commercialisation. They can undergo hydrolysis, giving rise to changes in morphology, crystal structure, optical absorption and deterioration of electrical properties. To overcome these, alterations in lead-based perovskites' chemical composition are attempted through the substitution of lead with other divalent elements such as tin (Serrano-Lujan, Espinosa et al. 2015). Thus, methylammonium tin halides ( $\text{MASnX}_3$ ) were explored for photovoltaic applications.  $\text{MASnX}_3$  is reported to exhibit more optimal bandgap (1.2-1.4 eV) than  $\text{MAPbX}_3$  (1.6-1.8 eV) (Konstantakou and Stergiopoulos 2017).

Perovskites are affected by environmental factors such as moisture, light, oxygen and temperature (Yuan, Li et al. 2017), (Diau, Jokar et al. 2019). Krishnan, Kaur et al. 2019). Upon contact with air,  $\text{MASnX}_3$  suffers from fast degradation due to instability of the Sn(II) state which easily gets oxidised to Sn(IV) iodide ( $\text{SnI}_4$ ) (Ava, Al Mamun et al. 2019). Insertion of ions to achieve a more stable crystal structure is another approach (Wei, Huang et al. 2018). The addition of water-soluble polymer in the perovskite precursor solution (Sun, Wu et al. 2017), employment of buffer layers between perovskite films and electron or hole selective layers (Wei, Guo et al. 2018) and substitution of the hole transport layer by more hydrophobic hole selective material also are reported.

It has been reported that the addition of polymeric materials into the precursors imparted enhanced properties to the perovskite films with desirable

morphology and crystallinity (Han, Lee et al. 2019). Long-chain polymers serve to form a crystalline network structure, creating compact films. Polymers containing S, N and O atoms with lone pairs of electrons were useful in passivating trap states in the perovskite layer for improved charge transfer and collection (Jiang, Wang et al. 2018). Zhang et al. successfully demonstrated improved device performance by employing semiconducting polymers (Ji, Peng et al. 2018). Chemically inert polymers were used for effective charge transport and better performance (Fakharuddin, Seybold et al. 2018). Insulating polymers have been doped with fullerene derivatives for better-conducting channels and to support charge transfer (Li, Chueh et al. 2013). The literature on systematic, in-depth studies are scarce and are needed to address the major inconsistency of the efficient charge transfer at the perovskite/polymer interface.

Herein, we report a facile synthesis of  $\text{MASnX}_3$  perovskite, achieved via a proprietary electrically conducting polysilsesquioxanes (PSQ) oligomer. The electrical and optical properties of the oligomer have been examined to check its adaptability for photovoltaic applications. Energy levels of the PSQ were determined theoretically and validated with experiments. The role of the PSQ in enhancing the stability of the perovskites and improving the optical properties was established. The PSQ can act as a hole transporting layer on the photovoltaic cell. The formation of  $\text{MASnX}_3$  crystals in the presence of the PSQ oligomer system is being reported for the first time.

## **5.2 Preparation of PSQ-Perovskite films**

Polysilsesquioxanes (PSQ) oligomer was synthesised by the hydrolysis and condensation of 3-glycidoxypropyltrimethoxysilane (GPTMS) and (3-aminopropyl)triethoxysilane (APTES) in an acidic medium.

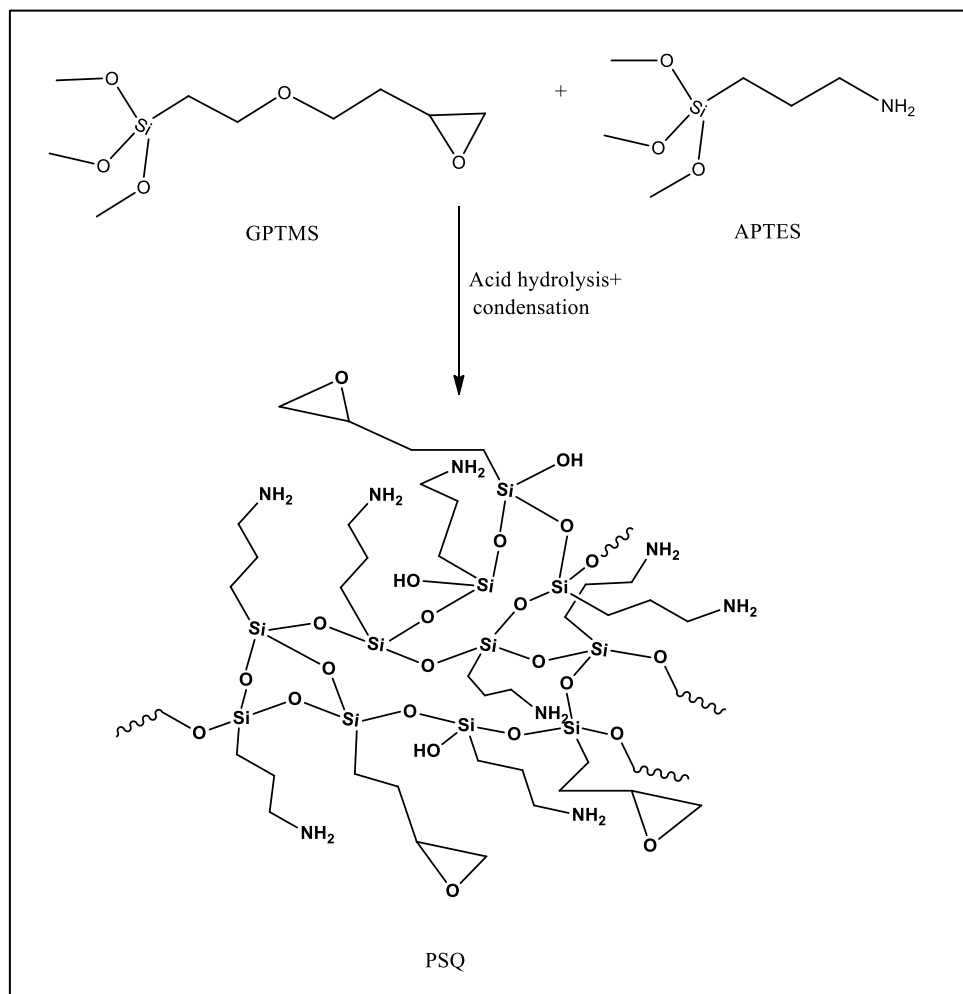


Figure 5.1 Scheme showing the synthetic route of polysilsesquioxanes (PSQ)

To make thin films of modified perovskite, dilute solutions of oligomers were prepared with concentrations ranging from 1 ppm to 5 ppm oligomer in DMF solvent. Better dispersion of  $\text{MASnBr}_3$  is obtained for the oligomer concentration of 1 ppm and is used for further studies.  $\text{MABr}$  and  $\text{SnBr}_2$  are taken in 1:1 mole ratio in the oligomer solution in DMF and mixed well using a mechanical stirrer for 5 minutes. The solution was coated on a glass substrate and heated to 110 °C for 10-15 minutes. These processes have been performed inside a glove box to avoid contamination from lab atmosphere. Oligomer solution (without any other components) was also coated on a glass substrate to evaluate the oligomer properties. The films were characterised using various analytical techniques.

## 5.3 RESULTS AND DISCUSSION

### 5.3.1 Structural characterisation

The oligomer PSQ was characterised using FTIR spectroscopy. The amine group in the oligomer exists as ammonium cation and chloride anion, as evident from the FTIR spectrum (Figure 5.2). The peaks at 1642 and 1570  $\text{cm}^{-1}$  correspond to the  $-\text{NH}_3^+$  asymmetric/symmetric stretching vibrations, respectively and the peak at 1489  $\text{cm}^{-1}$  corresponds to its bending vibration (Abhilash, Deepthi et al. 2015). Other prominent peaks appear at 1100 and 1023  $\text{cm}^{-1}$ , corresponding to the Si-O-Si linkages of caged and network structures of PSQ and the peak at 910  $\text{cm}^{-1}$  is due to the epoxy ring stretching vibrations. PSQ shows low volume resistivity in the order of  $2 \times 10^3 \Omega \text{ cm}$  making it a suitable electrically conductive layer. The possible interaction between the PSQ and  $\text{CH}_3\text{NH}_3\text{SnBr}_3$  perovskite crystals are analysed by FTIR analysis (Figure 5.2). FTIR spectrum of PSQ +  $\text{CH}_3\text{NH}_3\text{SnBr}_3$  shows peaks corresponding to Si-O-Si vibrations (1100 and 1023  $\text{cm}^{-1}$ ) and epoxy (910  $\text{cm}^{-1}$ ) of the PSQ. However, the  $-\text{NH}_3^+$  vibrations and C-H vibration of both  $\text{CH}_3\text{NH}_3\text{SnBr}_3$  and PSQ are not affected. These observations suggest the absence of any chemical interaction between the PSQ and the perovskite.

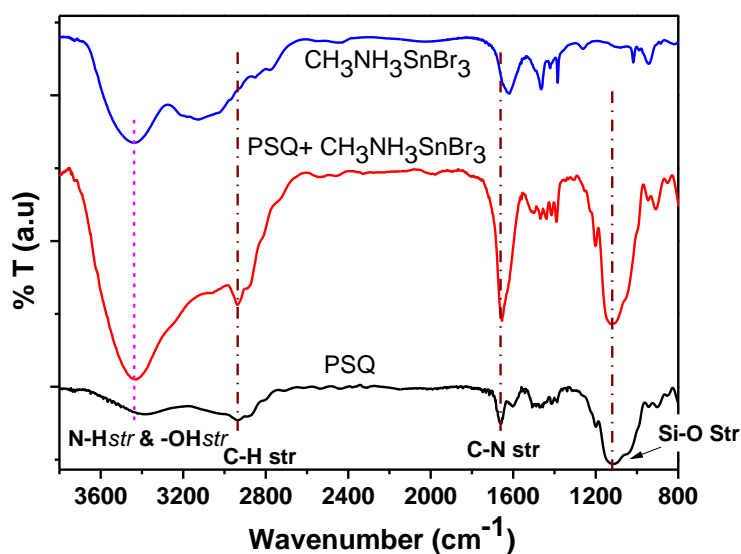


Figure 5.2. FTIR spectra of PSQ, PSQ+ $\text{CH}_3\text{NH}_3\text{SnBr}_3$  and the  $\text{CH}_3\text{NH}_3\text{SnBr}_3$ . The important features are marked.

The pure perovskite, PSQ and the perovskite- PSQ film were subjected to XRD analysis. The diffraction peaks at  $15^\circ$  and  $30^\circ$  are assigned to the planes (001) and (002) of the  $\text{CH}_3\text{NH}_3\text{SnBr}_3$ , indicating the formation of perovskite structure (Figure 5.3A). While cured films of PSQ show amorphous nature, the PSQ + perovskite films retained the crystallinity of  $\text{CH}_3\text{NH}_3\text{SnBr}_3$ . The crystallite size of  $\text{CH}_3\text{NH}_3\text{SnBr}_3$  is calculated from the peaks corresponding to the (001) and (002) planes of the XRD pattern using the Scherer equation. The values are  $\sim 89.5$  nm and  $\sim 85.6$  nm, respectively. The PSQ +  $\text{CH}_3\text{NH}_3\text{SnBr}_3$  show a crystallite size of  $\sim 38.2$  nm and  $\sim 34.3$  nm. The results showed that the crystallite size of PSQ +  $\text{CH}_3\text{NH}_3\text{SnBr}_3$  is less compared to that of  $\text{CH}_3\text{NH}_3\text{SnBr}_3$  because the polymer can affect crystal growth.

To study the effect of PSQ as an encapsulating layer to improve the stability of perovskite material, XPS analysis of the coated film which was exposed to relative humidity; RH 80% for 24 hours. The survey scan XPS shows the peaks of C, N, Sn, Si, Br, Cl and O (Figure 5.3B). The crystal structure of  $\text{CH}_3\text{NH}_3\text{SnBr}_3$  is getting altered due to the oxidation of  $\text{Sn}^{2+}$  to  $\text{Sn}^{4+}$ . This is evident in the high-resolution XPS spectra (Figure 5.3 C and D). The  $\text{CH}_3\text{NH}_3\text{SnBr}_3$  shows mainly  $\text{Sn}^{4+}$  state (486.7 and 495.1 eV for  $3d_{5/2}$  and  $3d_{3/2}$ , respectively), whereas the  $\text{CH}_3\text{NH}_3\text{SnBr}_3$  encapsulated with PSQ shows predominantly  $\text{Sn}^{2+}$  state (see Figure 5.3 D). These results suggest that the presence of PSQ prevents fast oxidation of  $\text{Sn}^{2+}$  in  $\text{CH}_3\text{NH}_3\text{SnBr}_3$  and stabilises the perovskite structure.

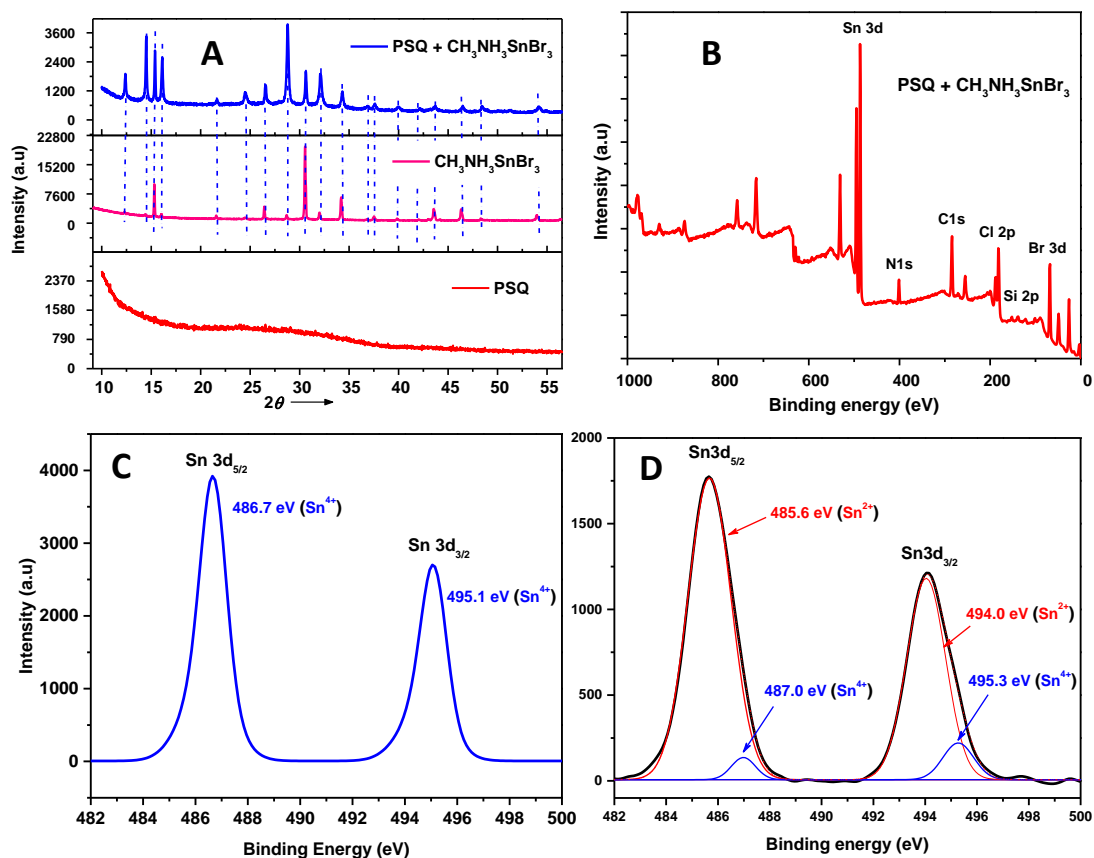


Figure 5.3. (A) XRD pattern of the PSQ,  $\text{CH}_3\text{NH}_3\text{SnBr}_3$  and  $\text{PSQ}+\text{CH}_3\text{NH}_3\text{SnBr}_3$ . (B) XPS survey scan spectrum. (C) the deconvoluted spectrum of Sn 3d peak of  $\text{CH}_3\text{NH}_3\text{SnBr}_3$  and (D) deconvoluted spectrum of Sn 3d peak of  $\text{PSQ} + \text{CH}_3\text{NH}_3\text{SnBr}_3$ .

Note that in (C), the deconvolution did not result in any peak split.

### 5.3.2 Optical characterisation

We checked the optical transparency of the film in the visible region of the electromagnetic spectrum. An adequately transparent film is required for photovoltaic applications. An excellent transparent film was obtained by coating the PSQ solution on a glass plate after heating at 90 °C. These films showed ~100% transmittance in the UV-Visible region (Figure 5.4), whereas the perovskite material shows absorption in the visible region (see in Figure 5.4A).

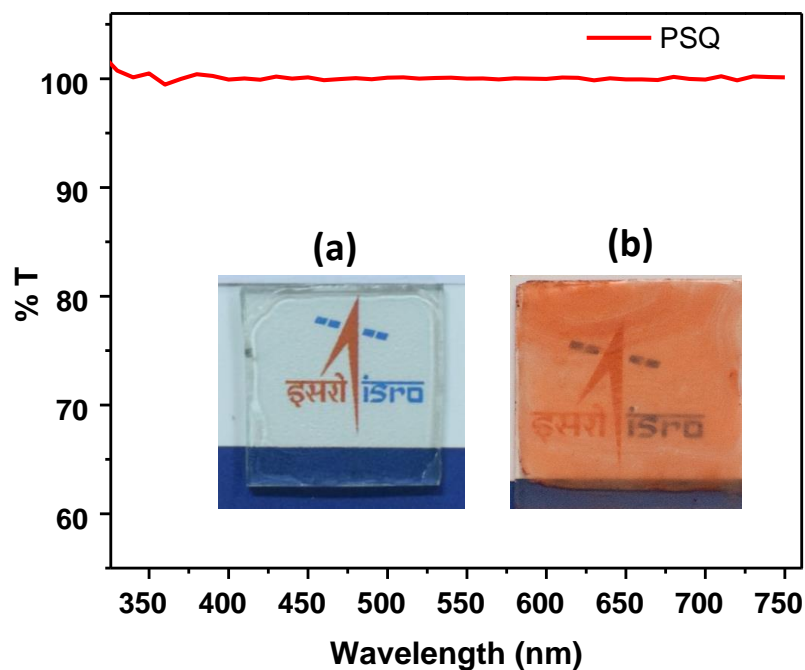


Figure. 5. 4. The transmittance (%) of the PSQ film in the UV-Visible region. *Insets:* glass slide coated with (A) PSQ and (B) PAQ+  $\text{CH}_3\text{NH}_3\text{SnBr}_3$

The optical properties of the materials were evaluated by measuring the UV-visible absorption and photoluminescence. At ambient conditions, the PSQ coated  $\text{CH}_3\text{NH}_3\text{SnBr}_3$  appears as crystals, but they deteriorate very fast. Because of this reason, only a weak absorption and emission of  $\text{CH}_3\text{NH}_3\text{SnBr}_3$  could be obtained (Figure 5.5 A). The  $\text{CH}_3\text{NH}_3\text{SnBr}_3$  materials incorporated in the PSQ film appear stable in the atmosphere and show excellent absorption characteristics in the visible range. It is noteworthy that  $\text{CH}_3\text{NH}_3\text{SnBr}_3$  crystals formed within the film show emission at 650 nm, attributed to the stable perovskites (Figure 5.5B). The bandgap evaluated from the absorption edge for  $\text{CH}_3\text{NH}_3\text{SnBr}_3$  and PSQ +  $\text{CH}_3\text{NH}_3\text{SnBr}_3$  are  $\sim 2.18$  eV and  $\sim 2.29$  eV, respectively.

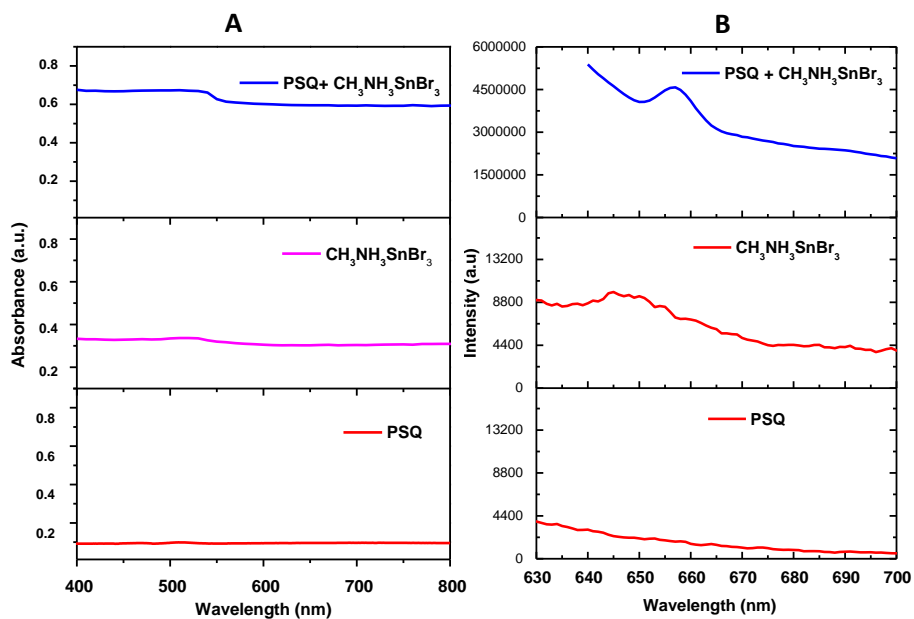


Figure 5.5. (A) UV-visible absorption spectra (B) Photoluminescence spectra of the PSQ,  $\text{CH}_3\text{NH}_3\text{SnBr}_3$  and  $\text{PSQ}+\text{CH}_3\text{NH}_3\text{SnBr}_3$ .

### 5.3.3 Morphological characterisation

Figure. 5.6 shows AFM images (Figure 5.6A and B) of the cured PSQ film and  $\text{PSQ}+\text{CH}_3\text{NH}_3\text{SnBr}_3$  film. The height profile of the  $\text{PSQ}+\text{CH}_3\text{NH}_3\text{SnBr}_3$  film is shown in Figure 5.6 C.

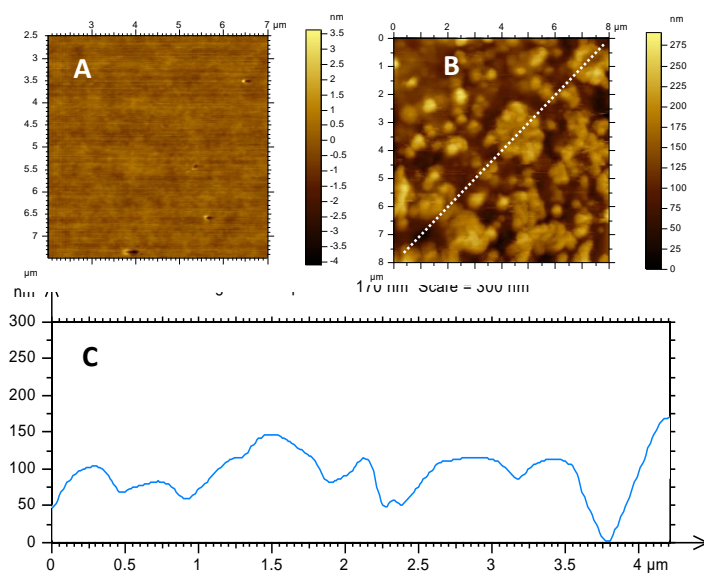


Figure. 5. 6. (A) The AFM images of PSQ and (B)  $\text{PSQ}+\text{CH}_3\text{NH}_3\text{SnBr}_3$ . The height profile of a line drawn in (B) is shown as (C)

SEM images (Figure 5.7 A, B and C) shows the formation of good films, embedding the high-quality crystals, which help improve the light-harvesting capability of the crystals formed within the PSQ matrix. Fabrication of devices with a high-quality perovskite layer under ambient conditions with good distribution is one of the most significant challenges in getting good efficiency. The roughness of the film helps to improve the external quantum efficiency. The EDS spectrum (Figure 5.7 D, E and F) showing the peaks corresponding to the elements; carbon, oxygen, bromine, silicon, tin and chlorine from  $\text{CH}_3\text{NH}_3\text{SnBr}_3$  and oligomer confirms the presence of  $\text{CH}_3\text{NH}_3\text{SnBr}_3$  within the PSQ films.

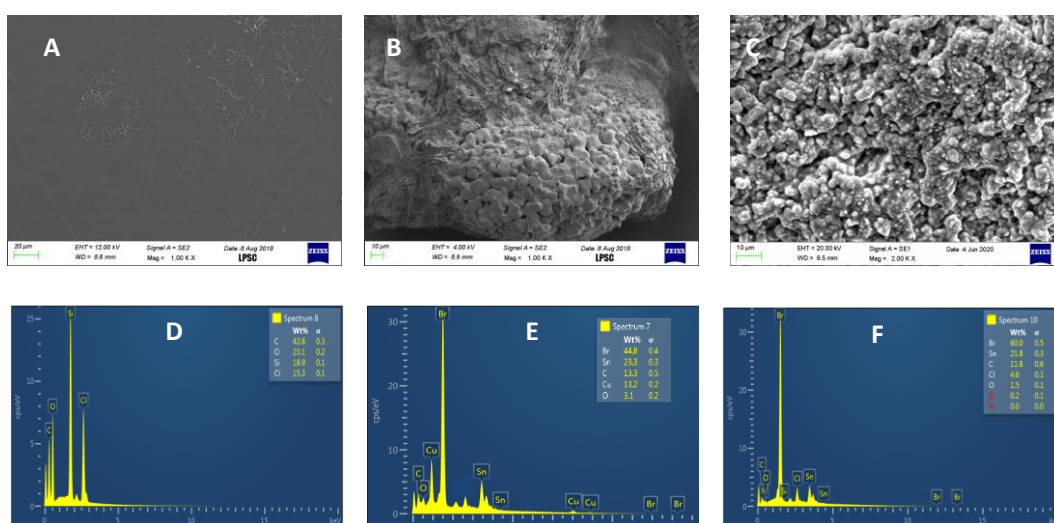


Figure 5.7. FE-SEM images of (A) PSQ, (B)  $\text{CH}_3\text{NH}_3\text{SnBr}_3$  and (c) PSQ+ $\text{CH}_3\text{NH}_3\text{SnBr}_3$  films. (D) EDS spectrum of PSQ, (E)  $\text{CH}_3\text{NH}_3\text{SnBr}_3$  and (F) PSQ +  $\text{CH}_3\text{NH}_3\text{SnBr}_3$

### 5.3.4 Electrical characterisation

The HOMO levels of the PSQ were calculated experimentally using cyclic voltammetry (Figure 5.8) and theoretically using Gaussian 09. The structure of the PSQ is optimised and the HOMO level was calculated. The values range from -5.2 eV to -5.6 V, which are comparable to the HOMO levels of the conventional hole transporting layer (HTM) (-5.00 to -5.50 eV) and compliments well with the energy levels of the prepared perovskite  $\text{CH}_3\text{NH}_3\text{SnBr}_3$ , indicating that they can be used as suitable HTMs for perovskite solar cell.

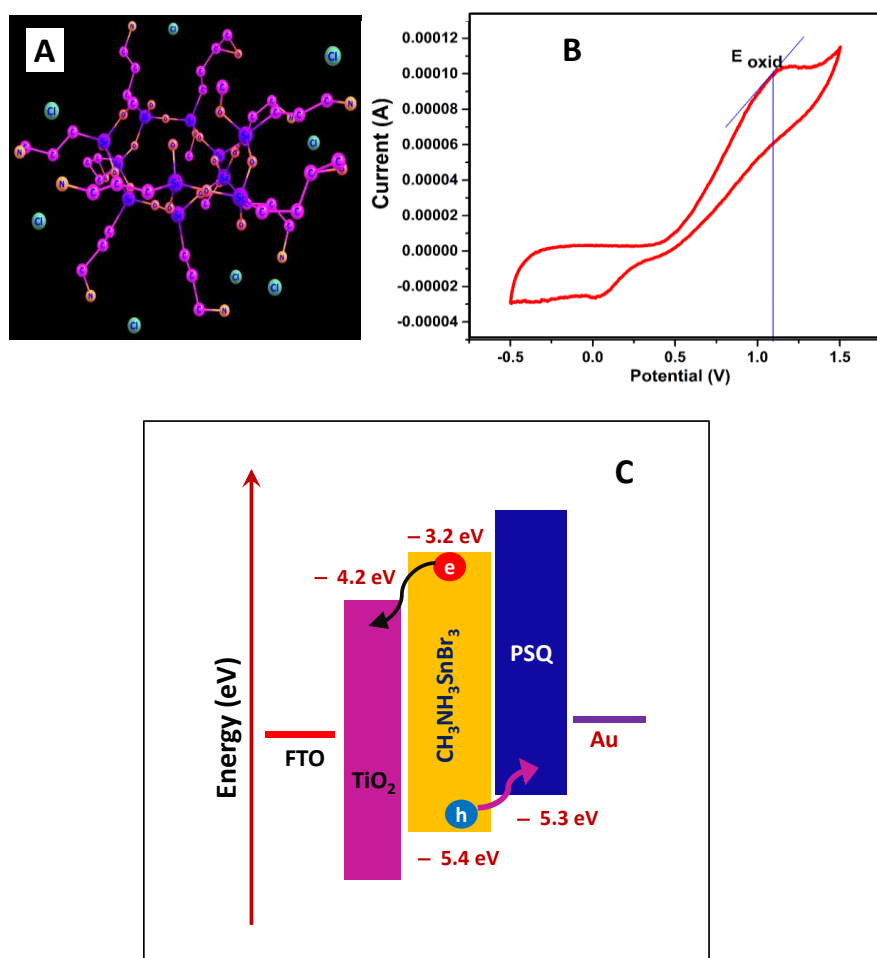


Figure 5.8 (A) Optimised structure of the PSQ using Gaussian 09 software, (B) Cyclic voltammogram of PSQ and (C) Energy bands diagram of the materials employed for the preparation of the cell.

### 5.3.5 Ageing studies

The stability of the perovskite embedded film has been monitored. The FTIR, XRD and UV-visible spectroscopy analysis of PSQ+ $CH_3NH_3SnBr_3$  film after six months of storage in the ambient atmosphere were recorded. (Figure 5.9). In the FTIR spectrum, the characteristic peaks of  $CH_3NH_3SnBr_3$  are found intact. The UV-visible absorption spectrum shows no change in the absorption region and the bandgap remained the same for  $CH_3NH_3SnBr_3$  (2.18 eV) and PSQ +  $CH_3NH_3SnBr_3$  (2.29 eV). From the XRD pattern, the major planes corresponding to the  $CH_3NH_3SnBr_3$  are unaffected. These results show that the PSQ can act as a protective layer to prevent the degradation of  $CH_3NH_3SnBr_3$ .

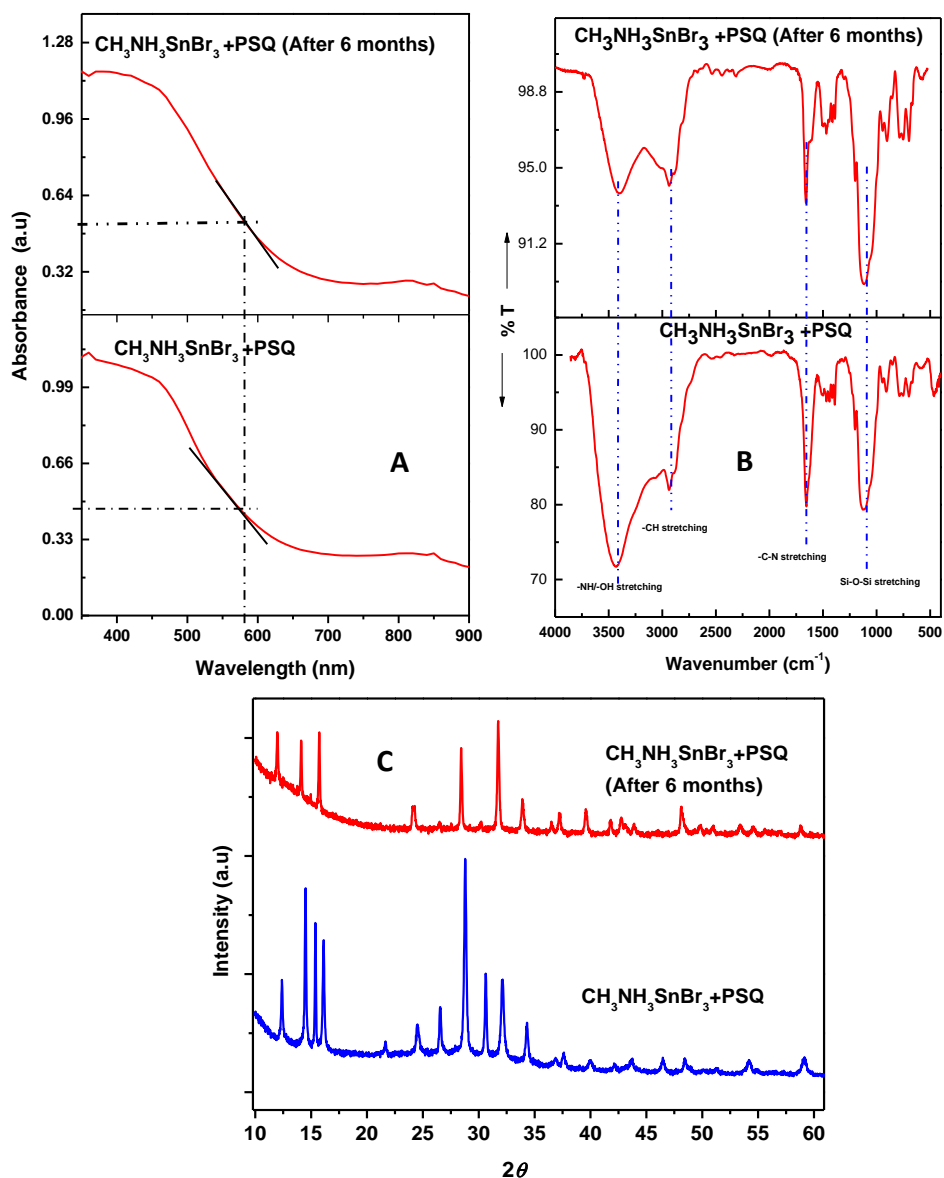


Figure 5.9 (A) UV-Visible spectra, (B) FTIR spectra and (C) XRD patterns of  $\text{CH}_3\text{NH}_3\text{SnBr}_3$  and  $\text{PSQ} + \text{CH}_3\text{NH}_3\text{SnBr}_3$ .

## 5.4 CONCLUSION

A novel, oligomeric silsesquioxane (PSQ) was synthesised and used for the encapsulation of  $\text{CH}_3\text{NH}_3\text{SnBr}_3$  perovskites. The PSQ demonstrates appropriate energy levels, good solubility for perovskite precursors, easy fabricability and excellent transparency in the UV-Visible and NIR regions which

are the essential factors influencing the performance of photovoltaic devices.  $\text{CH}_3\text{NH}_3\text{SnBr}_3$  perovskites grown within the PSQ films show better environmental stability by preventing oxidation than  $\text{CH}_3\text{NH}_3\text{SnBr}_3$  alone. Hence, the PSQ can act as a protective layer; and also a hole transporting layer in the photovoltaic devices, making them very attractive encapsulants. The PSQ oligomer and the processing method adopted is a facile and new approach for fabricating efficient perovskite-based photovoltaic devices.

# CHAPTER 6

## STABLE, MIXED METAL (Sn-Cu) HALIDE PEROVSKITES

### 6.1 Introduction

Solar cells based on lead-halide perovskites are being extensively studied due to their high power conversion efficiency, and these are widely explored for commercialisation (Correa-Baena, Abate et al. 2017). However, the toxicity of lead (Pb) is a significant challenge that hinders its practical applications. Due to Pb-perovskites' high environmental sensitivity, there is a pressing need to replace Pb with other environmentally benign alternatives (He, Liu et al. 2014; Babayigit, Ethirajan et al. 2016; Ju, Dai et al. 2017; Quan, Rand et al. 2019).

Tin (Sn) is considered an effective option to replace the Pb in perovskite materials envisaged for solar cell applications due to its desirable bandgap of  $\sim 1.3$  eV, close to the peak of the solar spectrum. Hence, efforts have been made by different research groups to exploit the potential of Sn-based perovskites (Chen, Wang et al. 2012; Chen, Yu et al. 2012; Abdelhady, Saidaminov et al. 2016). Methylammonium tin halide ( $\text{MASnX}_3$ ) perovskite shows an identical crystal structure to methylammonium lead halide ( $\text{MAPbX}_3$ ). However, similar to lead-based systems, their poor environmental stability limits the application of Sn-perovskite also. Sn-perovskites are highly sensitive to oxygen and moisture since the  $\text{Sn}^{2+}$  rapidly oxidises to  $\text{Sn}^{4+}$ . This oxidation can lead to structural changes and deteriorate the photovoltaic performance (Lee, Stoumpos et al. 2014; Zhang, Mao et al. 2019).

Researchers have made several attempts to improve the stability of Sn based systems. The concept of cations to alter properties of perovskites have been reported by many researchers (Cheng and Lin 2010; Eperon and Ginger 2017; Tang, Xu et al. 2017; Dawson, Ribeiro et al. 2021). It is reported that metal cations such as cobalt ( $\text{Co}^{2+}$ ) and bismuth ( $\text{Bi}^{2+}$ ) can act as effective dopants to stabilise Sn-perovskites (Yuan, Li et al. 2017; Song, Jiang et al. 2018). The

stability of  $\text{Cu}^{2+}$  and its ability to form compounds with large absorption coefficients in the visible region makes Cu a potential candidate for the partial replacement of Sn (Willett, Place et al. 1988). Cheng et al. reported using Cu as a second cation in the Pb-perovskite systems (Greenwood and Earnshaw 2012). Here, Cupric ion ( $\text{Cu}^{2+}$ ), having a small ionic radius, formed layered perovskites instead of 3D structures (Willett, Place et al. 1988). Prevalence of Jahn–Teller distortion in  $\text{Cu}^{2+}$  systems also offers higher flexibility to the structure, facilitating broader tunability in properties (Cortecchia, Dewi et al. 2016).

This chapter discusses the synthesis of methylammonium bimetallic perovskites based on Sn and Cu of the general formula  $\text{MeNH}_3\text{Br}(\text{SnBr}_2)_{1-x}(\text{CuCl}_2)_x$  (Jahandar, Heo et al. 2016). The mixed perovskite has been prepared using methylammonium bromide,  $\text{SnBr}_2$  and  $\text{CuCl}_2$  and their structure, stability and optoelectronic properties were thoroughly investigated. Here we focus on the systematic studies to develop non-toxic and stable organic-inorganic hybrid materials for photovoltaic applications.

## 6.2. Synthesis methods

MABr,  $\text{SnBr}_2$  and  $\text{CuCl}_2$  were taken in various mole ratios (shown in Table 6.1) in DMF and stirred well until it dissolved completely in DMF. These solutions were heated in an air oven at 110 °C for 30 min to form perovskite crystals. The obtained crystals were washed with toluene to remove any excess MABr and vacuum dried. Good crystals were obtained for the mole ratio  $\text{Sn}_1:\text{Cu}_0$ ,  $\text{Sn}_{0.5}:\text{Cu}_{0.5}$  and  $\text{Sn}_0:\text{Cu}_1$  and were taken for further characterisation.

Table 6. 1. Proportion of  $\text{CH}_3\text{NH}_3\text{Br}:\text{SnBr}_2:\text{CuCl}_2$  used for the synthesis

Sample Name	The mole ratio of $\text{CH}_3\text{NH}_3\text{Br}:\text{SnBr}_2:\text{CuCl}_2$
$\text{Sn}_1:\text{Cu}_0$	1: 1: 0
$\text{Sn}_{0.75}:\text{Cu}_{0.25}$	1: 0.75:0.25
$\text{Sn}_{0.5}:\text{Cu}_{0.5}$	1: 0.5: 0.5
$\text{Sn}_{0.25}:\text{Cu}_{0.75}$	1: 0.25:0.75
$\text{Sn}_0:\text{Cu}_1$	1: 0: 1

## 6.3 Result and Discussion

### 6.3.1 Structural characterisation

Pure and mixed metal perovskite crystals of Sn and Cu were synthesised as described in Section 6.2 and characterised using spectroscopic and microscopic methods. The motivation to chose copper chloride as the precursor over copper bromide is that  $\text{Cl}^-$  improves the stability of material against the reduction of Cu. Moreover, it helps to enhance crystallisation of the perovskite (Tsai, Wu et al. 2016; Kim, Kim et al. 2019; Yang, Choi et al. 2021).

The XRD pattern (Figure 6.1A) of the Sn-perovskite (termed as  $\text{Sn}_1:\text{Cu}_0$  for discussion) shows the planes viz., (001), (011), (111), (002), (012), (112), (022), and (122) matching with those of 3D perovskites;  $\text{CH}_3\text{NH}_3\text{SnBr}_3$ . The presence of these peaks depicts the formation of a normal 3D perovskite structure for the material formed during the reaction of the  $\text{Sn}_1:\text{Cu}_0$  system. The unlabelled peaks correspond to unreacted  $\text{SnBr}_2$  (Dimesso, Mayer et al. 2018). The XRD spectra of the  $\text{CuCl}_2$ ,  $\text{SnBr}_2$  and  $\text{MABr}$  are given in Figure 6.1B for reference.

The XRD pattern of the compound formed from the reaction of  $\text{CuCl}_2$  with methylammonium bromide (termed as  $\text{Sn}_0:\text{Cu}_1$ ) shows the crystalline phases of  $(\text{CH}_3\text{NH}_3)_2\text{CuCl}_2\text{Br}_2$  (Elseman, Shalan et al. 2018). The crystal structure consists of a 3D ‘perovskite cage’ and is limited by the geometric considerations of the empirical Goldschmidt tolerance factor ( $t$ ),  $t = \frac{r_A+r_X}{\sqrt{2}(r_B+r_X)}$  and octahedral factor ( $\mu$ ),  $\mu = \frac{r_B}{r_X}$ , in which  $r_A$ ,  $r_B$ , and  $r_X$  are the effective radii of  $\text{A}^+$ ,  $\text{B}^{2+}$ , and  $\text{X}^-$  ions, respectively (Travis, Glover et al. 2016). Tolerance factor,  $t$ , assess whether A cation can stabilise the  $\text{BX}_3$  framework of corner-sharing octahedral (Xiao and Yan 2017). Generally, a stable 3D perovskite structure is formed when  $t$  and  $\mu$  in the range of  $0.8 \leq t \leq 1$  and  $0.414 \leq \mu < 0.592$ . In the case of  $(\text{CH}_3\text{NH}_3)_2\text{CuCl}_2\text{Br}_2$ , which shows the values of  $t > 1$  and  $\mu < 0.41$ , can crystallise in lower dimensionality (data in Table 6.1 is used for the calculations). The smaller ionic radii of  $\text{Cu}^{2+}$  cation than  $\text{Sn}^{2+}$ , leads to an arrangement of  $\text{Cu}^{2+}$  in a layered configuration rather than a 3D structure.

The material with mole ratio  $\text{Sn}_{0.5}:\text{Cu}_{0.5}$  shows the planes of both  $\text{CH}_3\text{NH}_3\text{SnBr}_3$  and  $(\text{CH}_3\text{NH}_3)_2\text{CuCl}_2\text{Br}_2$  with a shift in the  $2\theta$  values (Table 6.2). The d-spacing corresponding to the major plane of the 3D perovskite structure is decreased, while there is an increase in d-spacing observed for 2D planes. This observation depicts that the compound formed will have both 2D structure and 3D structure with considerable change in the lattice spacing compared to the single metal perovskites.

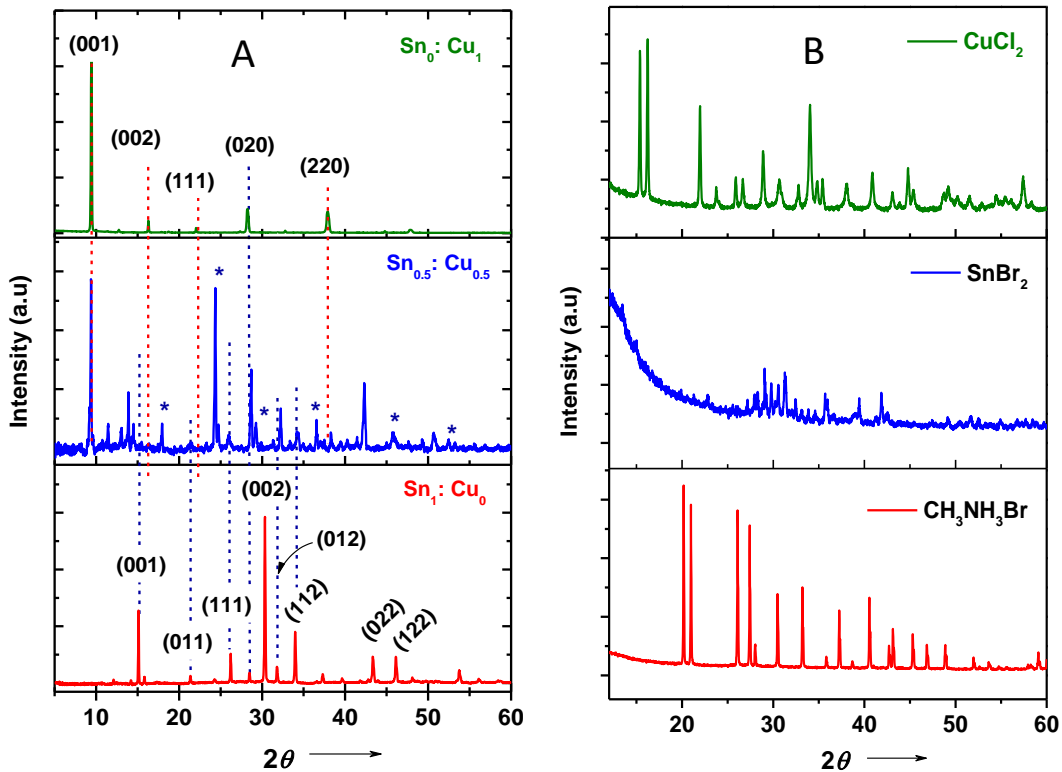


Figure 6.1 The XRD pattern of perovskite (A) and precursor materials (B) used for synthesizing various perovskites. The name of perovskite and the precursor is given in each spectrum. The \* peaks in the middle pane of (A) depict the presence of layered structure (Willett, Place et al. 1988)

Table 6.1 Calculation of stability factors of 3D perovskites

$r_A$ (pm)	$r_B$ (pm)	$r_X$ (pm)	Goldschmidt tolerance factor ( $t$ ),	
			$t = \frac{r_A + r_X}{\sqrt{2} (r_B + r_X)}$	Octahedral factor ( $\mu$ ), $\mu = \frac{r_B}{r_X}$
217	Cu <sup>2+</sup> (73)	Cl <sup>-</sup> (181)	1.11	0.40
217	Cu <sup>2+</sup> (73)	Br <sup>-</sup> (196)	1.09	0.37
217	Sn <sup>2+</sup> (112)	Cl <sup>-</sup> (181)	0.96	0.61
217	Sn <sup>2+</sup> (112)	Br <sup>-</sup> (196)	0.94	0.57

Table 6.2 Diffraction angle and the calculated d-spacing values from XRD data. Cu K $\alpha$  radiation was used at a scan rate of 4.8°/min. In right-side columns, the diffraction peaks of Sn<sub>0.5</sub>:Cu<sub>0.5</sub> are segregated for 2D and 3D.

Sn <sub>1</sub> :Cu <sub>0</sub>		Sn <sub>0.5</sub> :Cu <sub>0.5</sub>	
$2\theta$	d-spacing (Å)	$2\theta$	d-spacing (Å)
15.082	5.869	15.933	5.558
26.227	3.395	27.643	3.224
30.346	2.943	31.590	2.829
Sn <sub>0</sub> :Cu <sub>1</sub>			
$2\theta$	d-spacing (Å)		
9.428	9.373	9.191	9.614
28.226	3.159	27.643	3.224
37.913	2.371	37.913	2.421

The FTIR spectra (Figure 6.2) of the materials show a peak at 3033 cm<sup>-1</sup>, corresponding to the asymmetric stretching vibration of NH<sub>3</sub><sup>+</sup>. The NH<sub>3</sub><sup>+</sup> bending vibration of MABr was observed at ~1570 cm<sup>-1</sup>. While in the case of perovskite materials, this band is blue-shifted to ~1620 cm<sup>-1</sup>. The large shift; ~50 cm<sup>-1</sup> implies the restricted vibration in the crystal lattice and the cation charge density is centred towards the N atom. Hence, N-H protons will strongly affect the dipole moment compared to C-H protons, resulting in strong IR activity. Due to the

stronger bonds, their frequencies are blue-shifted in the perovskite structure (Brivio, Frost et al. 2015). For the samples of  $\text{Sn}_1:\text{Cu}_0$  and  $\text{Sn}_0:\text{Cu}_1$ , the broad peak at  $3440\text{ cm}^{-1}$  is due to the absorbed moisture. This band is very minimal in  $\text{Sn}_{0.5}:\text{Cu}_{0.5}$  perovskite, indicating less moisture content in the sample.

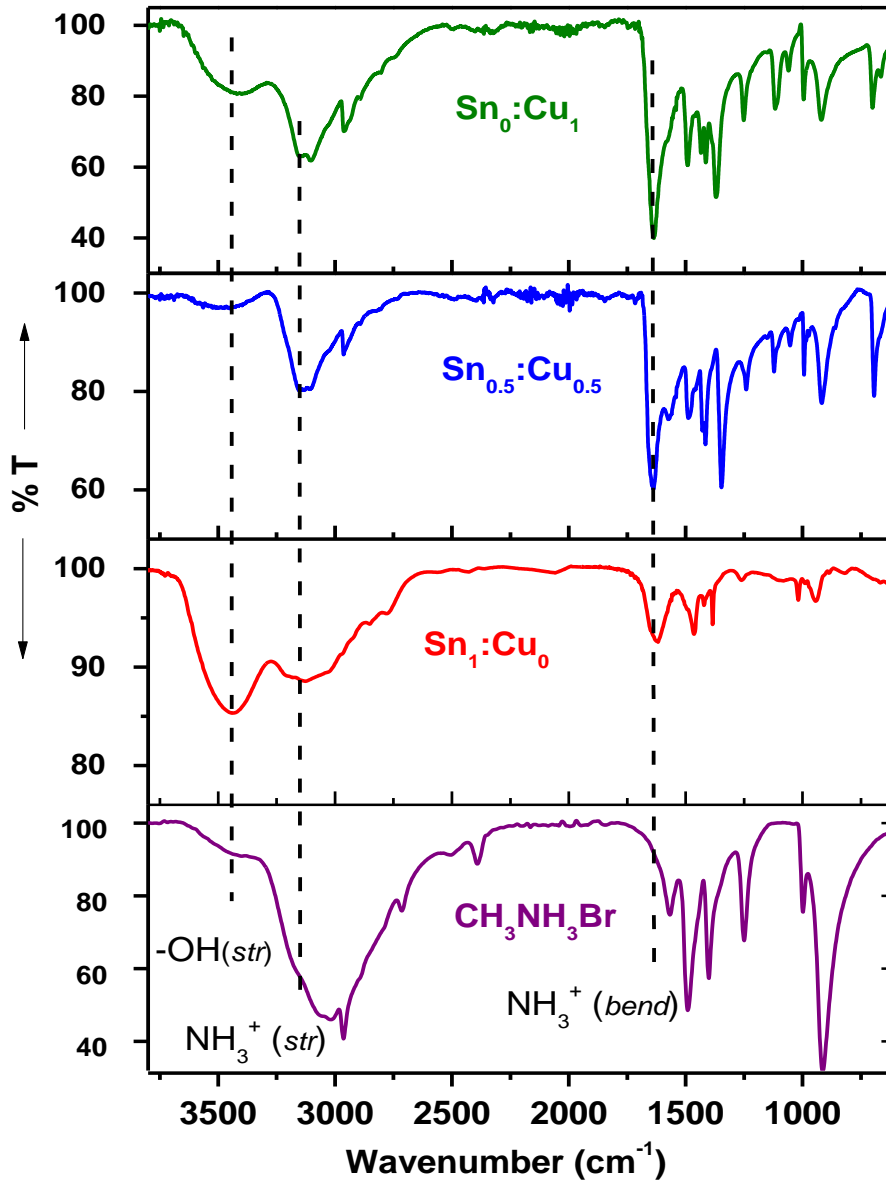


Fig. 6.2 FTIR spectra of perovskites (labelled in each spectrum) and MABr spectrum is given in the bottom pane for comparison. The position of  $-\text{OH}_{str}$ ,  $-\text{NH}_3^+_{str}$  and  $-\text{NH}_3^+_{bend}$  vibrations is marked with dotted lines

X-ray photoelectron spectroscopy (XPS) was carried out to investigate the chemical state of Sn and Cu in the present perovskites (Figure 6.3A and B).

The binding energy values of  $3d_{5/2}$  and  $3d_{3/2}$  peaks of  $\text{Sn}^{2+}$  generally appear at  $\sim 485.6$  eV and  $\sim 494.0$  eV, respectively (Xia, Wang et al. 2014). But, for  $\text{Sn}_1:\text{Cu}_0$  sample, the binding energy values were 486.6 eV ( $3d_{5/2}$ ) and 495.0 ( $3d_{3/2}$ ). These higher binding energy values indicate the presence of  $\text{Sn}^{4+}$  oxidation state rather than  $\text{Sn}^{2+}$  (See Figure 6.3A). The full width at half maximum (FWHM) of these peaks suggests the presence of only one oxidation state, which is  $\text{Sn}^{4+}$ . This observation proposes the complete oxidation of  $\text{Sn}^{2+}$  state to  $\text{Sn}^{4+}$  in the  $\text{Sn}_1:\text{Cu}_0$  perovskite. XRD analysis shows the disappearance of major crystalline planes of  $\text{Sn}_1:\text{Cu}_0$  sample taken after a week. This is due to the change in the crystal structure of the perovskite due to oxidation of  $\text{Sn}^{2+}$  to  $\text{Sn}^{4+}$ , supports the XPS data. The sample was stored in ambient conditions for one week so that complete oxidation occurs.

In the  $\text{Sn}_{0.5}:\text{Cu}_{0.5}$  sample, the binding energy values match the  $\text{Sn}^{2+}$  state (485.6 eV and 494.0 eV) (Figure 6.3B). We can infer that the  $\text{Sn}^{2+}$  in the  $\text{Sn}_{0.5}:\text{Cu}_{0.5}$  perovskite was stable towards oxidation, compared to  $\text{Sn}_1:\text{Cu}_0$  perovskite, which was oxidised entirely to  $\text{Sn}^{4+}$ . The XPS spectrum of the Cu region (Figure 6.3C) shows that Cu exhibits both +2 and +1 oxidation states in  $\text{Sn}_{0.5}:\text{Cu}_{0.5}$ . However, in the  $\text{Sn}_0:\text{Cu}_1$  system, Cu exists in +2 oxidation state. The presence of  $\text{Br}^-$  is responsible for the  $\text{Cu}^{2+}$  reduction to  $\text{Cu}^{1+}$ . The XPS spectrum proves the considerable change in the electronic structure of  $\text{Sn}_{0.5}:\text{Cu}_{0.5}$  crystal system compared to the single metal perovskites.

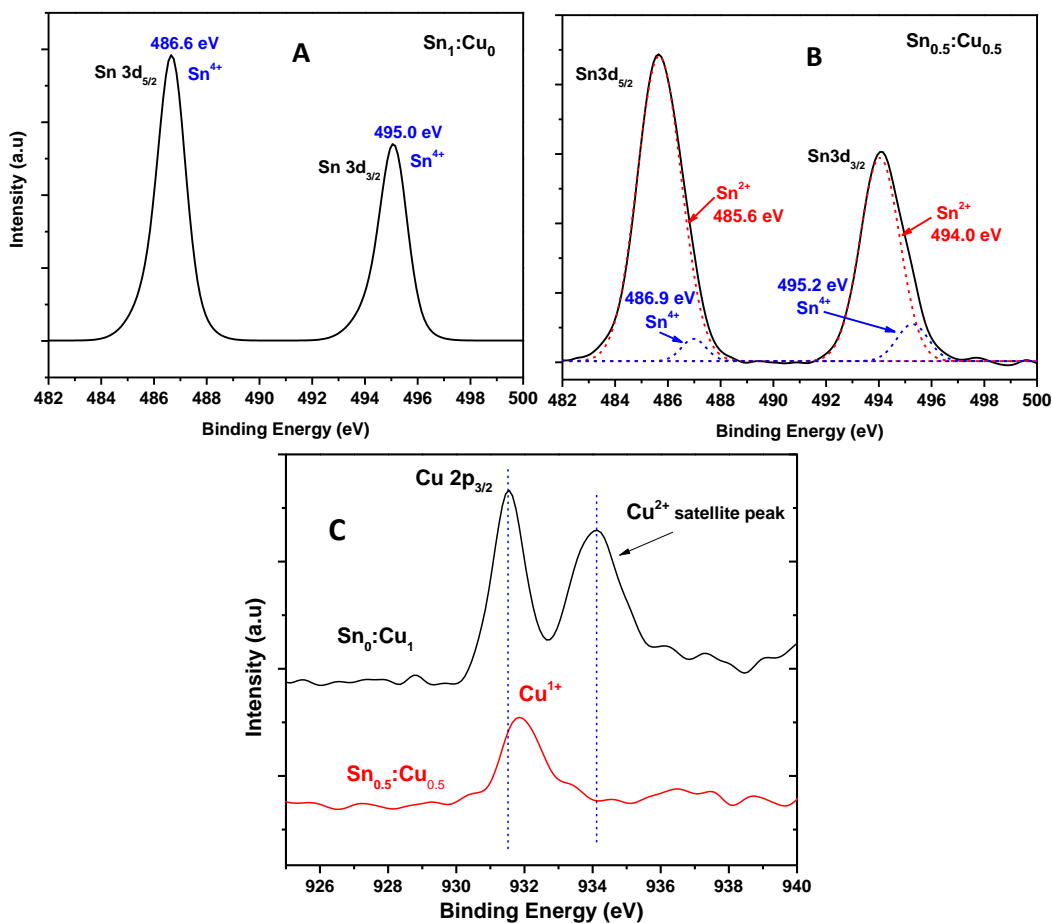


Fig. 6.3 High-resolution XPS spectra of Sn 3d peaks of (A) Sn<sub>1</sub>:Cu<sub>0</sub> (B) Sn<sub>0.5</sub>:Cu<sub>0.5</sub> and in (C), the Cu 2p peaks are shown. Sn<sub>1</sub>:Cu<sub>0</sub> material shows only Sn<sup>4+</sup> oxidation state (A), whereas Sn<sub>0.5</sub>:Cu<sub>0.5</sub> material is dominated with Sn<sup>2+</sup> oxidation state (B) and high-resolution XPS spectra showing the binding energy values of Cu 3P<sub>3/2</sub>.

The effect of Cu on the energy levels of the two- Cu containing materials (Sn<sub>0.5</sub>:Cu<sub>0.5</sub>, Sn<sub>0</sub>:Cu<sub>1</sub>) was evaluated using ultraviolet photoelectron spectroscopy (UPS). The valence band edge (Figure 6.4A) obtained from the UPS spectra (Figure 6.4B) of Sn<sub>1</sub>:Cu<sub>0</sub> and Sn<sub>0.5</sub>:Cu<sub>0.5</sub> were analysed. From the intersection of the linear parts of the UPS spectrum, the values of E<sub>onset</sub> was calculated. Further, the valence band maximum (VBM) was calculated from the onset of the UPS spectrum and tabulated in Table 6.2.

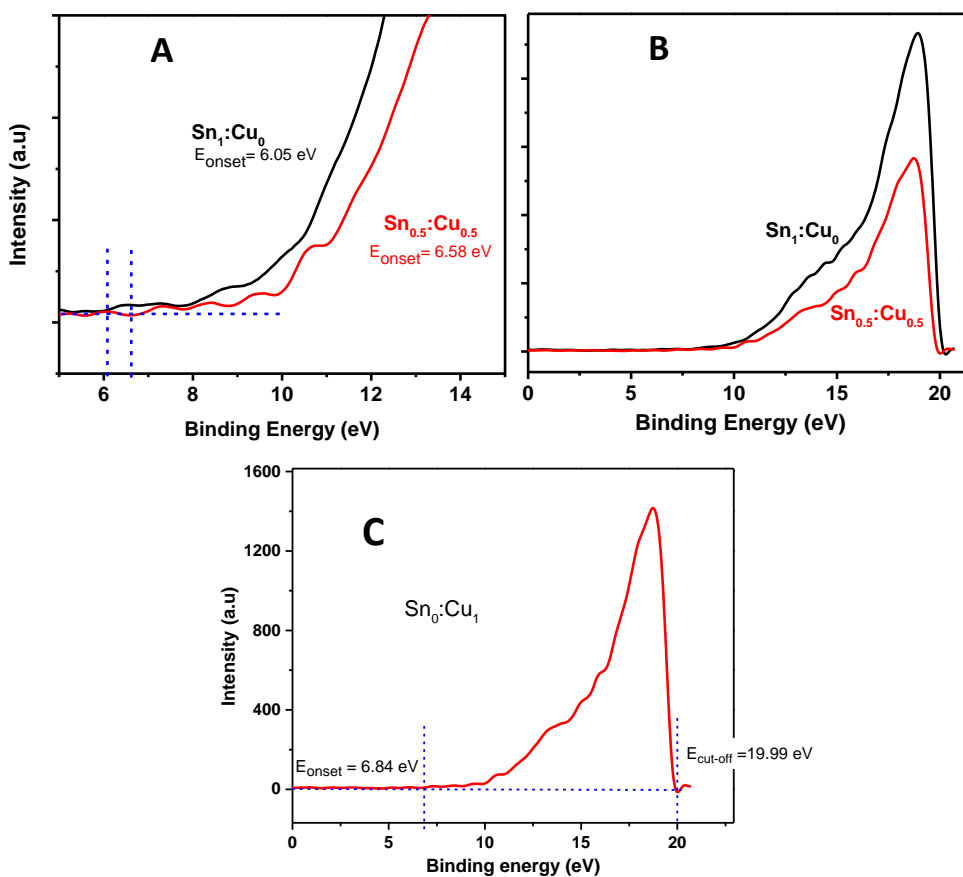


Figure 6.4 Different regions of the UPS spectra of the perovskite materials (A:  $\text{Sn}_1:\text{Cu}_0$ , B:  $\text{Sn}_{0.5}:\text{Cu}_{0.5}$  and C:  $\text{Sn}_0:\text{Cu}_1$ ).

Table 6.3. Valence band maxima obtained from UPS spectra in Fig 6.4

Sample Name	Valence band maximum (VBM) in eV
$\text{Sn}_1:\text{Cu}_0$	6.05
$\text{Sn}_{0.5}:\text{Cu}_{0.5}$	6.58
$\text{Sn}_0:\text{Cu}_1$	6.84

The thermal stability of the materials was studied using thermogravimetric analysis (TGA). The TGA experiments were done at a heating rate of  $10\text{ }^\circ\text{C}/\text{min}$  from  $30$  to  $700\text{ }^\circ\text{C}$ . The onsets of weight loss started below  $100\text{ }^\circ\text{C}$  for the  $\text{Sn}_1:\text{Cu}_0$  and  $\text{Sn}_0:\text{Cu}_1$  systems (Figure 6.5A). This decomposition is

mainly due to the absorbed moisture. The presence of moisture is clearly visible in the FTIR spectra (Figure 6.5B). For  $\text{Sn}_{0.5}\text{:Cu}_{0.5}$ , the decomposition starts from  $\sim 200\text{ }^\circ\text{C}$ , which confirms the non-hygroscopic nature and environmental stability of the material. To explain the moisture stability of the  $\text{Sn}_{0.5}\text{:Cu}_{0.5}$  system, material kept under ambient conditions for 1 month (RH < 60 %) was subjected to FTIR and UV analysis. The -OH absorption was unaffected even after one month (Figure 6.5B). In Figure 6.5B, initial spectra are taken on the same day of synthesis and the spectrum (black traces) was recorded after keeping the sample in normal atmospheric conditions. In the FTIR spectra (B), the -OH<sub>str</sub> region (marked) appears in similar intensities shows the same moisture content. The absorbance of the two samples is comparable in the visible region (C).

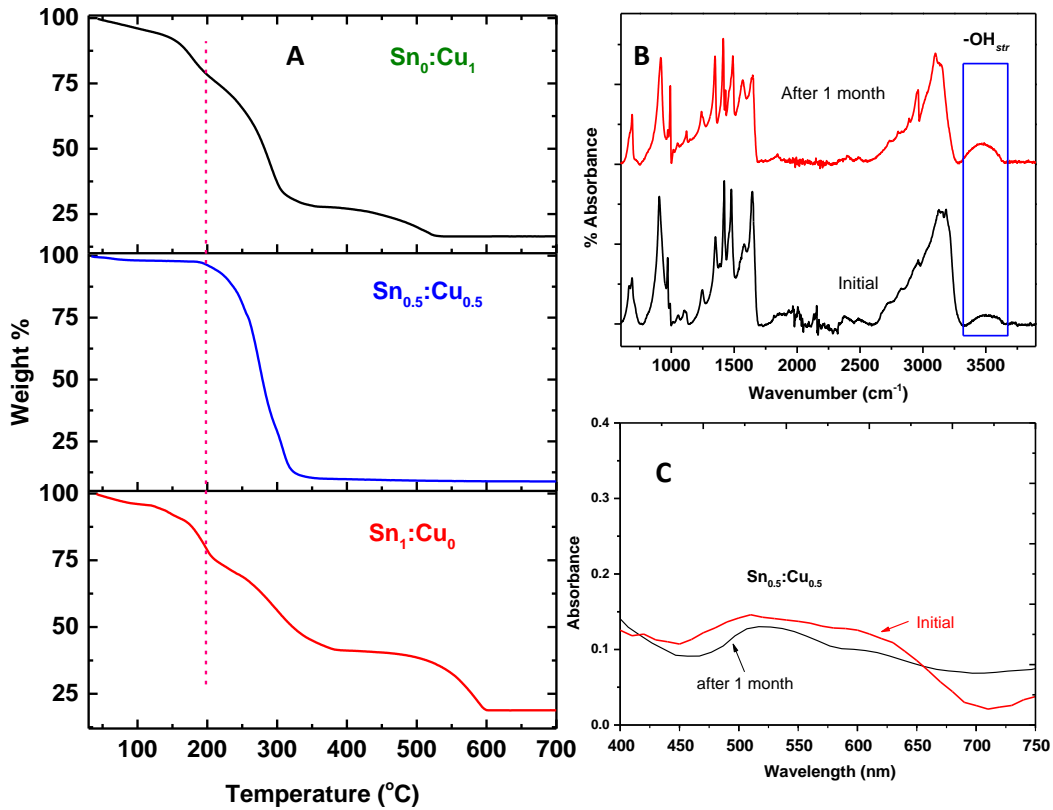


Figure. 6.5 (A) Thermogram of  $\text{Sn}_1\text{:Cu}_0$ ,  $\text{Sn}_{0.5}\text{:Cu}_{0.5}$  and  $\text{Sn}_0\text{:Cu}_1$ . The dotted line represents the onset of weight loss for  $\text{Sn}_{0.5}\text{:Cu}_{0.5}$ , (B) FTIR spectrum and (C) UV-visible spectrum of  $\text{Sn}_{0.5}\text{:Cu}_{0.5}$  material.

### 6.3.2 Optical characterisation

Figure 6.6 A shows the UV-visible absorption spectra of  $\text{Sn}_1\text{:Cu}_0$ ,  $\text{Sn}_{0.5}\text{:Cu}_{0.5}$  and  $\text{Sn}_0\text{:Cu}_1$ . The addition of  $\text{CuCl}_2$  into the  $\text{MASnBr}_3$  system exerts significant influence on the optical properties. In the  $\text{Sn}_{0.5}\text{:Cu}_{0.5}$  composition, the absorption edge is red-shifted compared to tin- and copper- alone systems. The bandgaps of the materials were calculated from the Tauc plot (insets of Figure 6.6A) and found to be 2.05 eV, 1.80 eV and 2.53 eV for  $\text{Sn}_1\text{:Cu}_0$ ,  $\text{Sn}_{0.5}\text{:Cu}_{0.5}$  and  $\text{Sn}_0\text{:Cu}_1$ , respectively. The reduction in the bandgap of  $\text{Sn}_{0.5}\text{:Cu}_{0.5}$  with that of  $\text{Sn}_1\text{:Cu}_0$  is attributed to the lattice size contraction (Prasanna, Gold-Parker et al. 2017). It is clear from Table 6.2 that d-spacing have been decreased for  $\text{Sn}_{0.5}\text{:Cu}_{0.5}$  implying the lattice contraction.

The electronic structure is administered by the chemical composition and crystal structure of the materials and determines the photoluminescence emission features. In perovskite materials, alteration in the B site significantly modifies the bandgap and creates the energetic states deep in the bandgap. Such trap states vary the photoluminescence property by the nonradiative recombination process. The halide ions and metal cation substitution in any site of halide perovskites could alter its bandgap (Lu, Biesold-McGee et al. 2020).

The photoluminescence spectra of  $\text{Sn}_1\text{:Cu}_0$  and  $\text{Sn}_{0.5}\text{:Cu}_{0.5}$  at an excitation wavelength of  $\lambda_{\text{exc}} = 550$  nm show emission at 650 nm and 710 nm (Figure 6.7 A). Copper-based perovskite ( $\text{Sn}_0\text{:Cu}_1$ ) is not exhibiting luminescence at an excitation wavelength of  $\lambda_{\text{exc}} = 550$  nm. It is showing only feeble emission for the excitation at  $\lambda_{\text{exc}} = 450$  nm. From the literature, it was verified that the A-site cations ( $\text{CH}_3\text{NH}_3^+$ ) do not directly affect the bandgap because they form bonding states deep in the VBM and do not involve in the hybridisation with  $\text{BX}_6^{2-}$  octahedra near VBM or conduction band minimum (CBM). In the present case, the spectroscopic transitions were altered in such a way as to yield higher emission intensity. Thus, modification of B site with Sn contributes to the emissions at 650 and 710 nm (Lu, Biesold-McGee et al. 2020),(Goetz, Taylor et al. 2020), (Wang, Zhang et al. 2018).

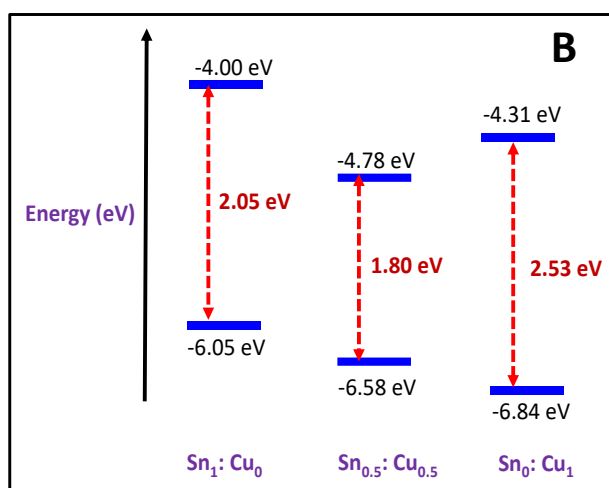
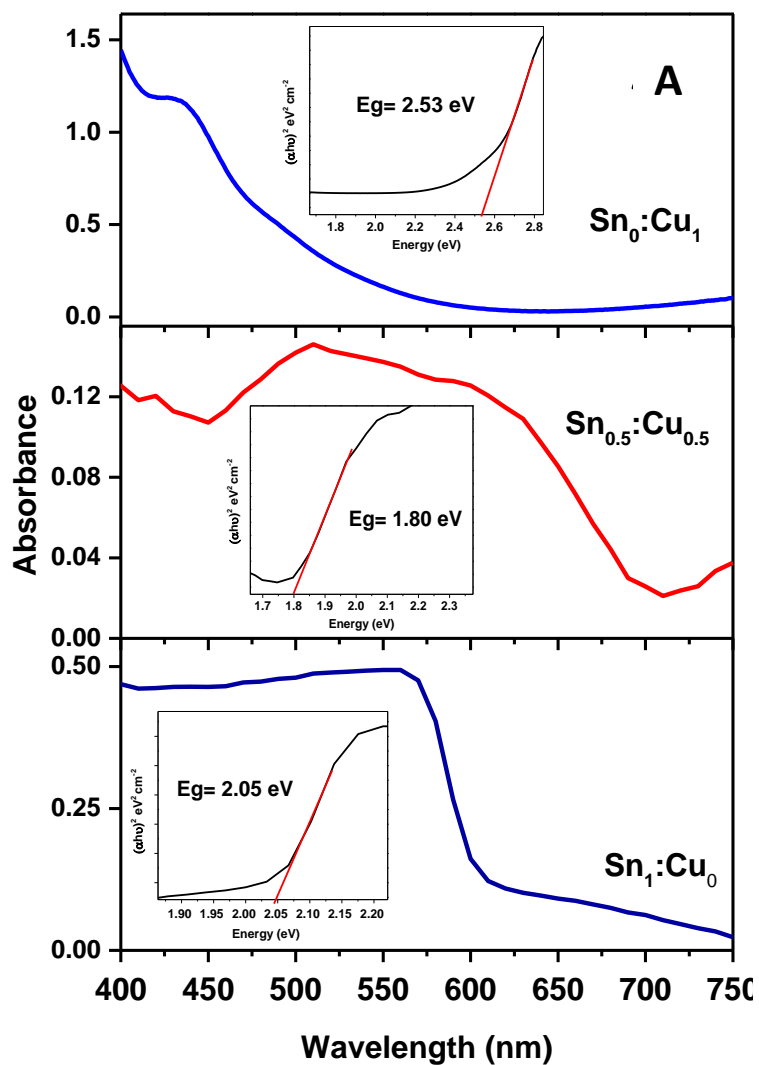


Figure 6.6 (A) UV-visible absorption spectra and (B) Energy band diagram of the perovskites.

To evaluate the lifetime ( $\tau$ ) of the excitons generated on exposure to light, time-correlated single-photon counting (TCSPC) studies were carried out. (Figure 6.7B) shows the decay profile of the perovskite materials. The lifetime of  $\text{Sn}_{0.5}\text{Cu}_{0.5}$  is higher than that of  $\text{Sn}_1\text{Cu}_0$ . The average lifetime of  $\text{Sn}_{0.5}\text{Cu}_{0.5}$  fits biexponential, while a mono-exponential fit is obtained for  $\text{Sn}_1\text{Cu}_0$  (see Table 6.4). The lower fluorescence emission of the  $\text{Sn}_1\text{Cu}_0$  system compared to the  $\text{Sn}_{0.5}\text{Cu}_{0.5}$  system is corroborated by the lower lifetime component. For  $\text{Sn}_0\text{Cu}_1$ , the lifetime of the excited species could not be measured due to instrument limitation. The lifetime data prove the suitability of the tin-copper system over a single cation approach.

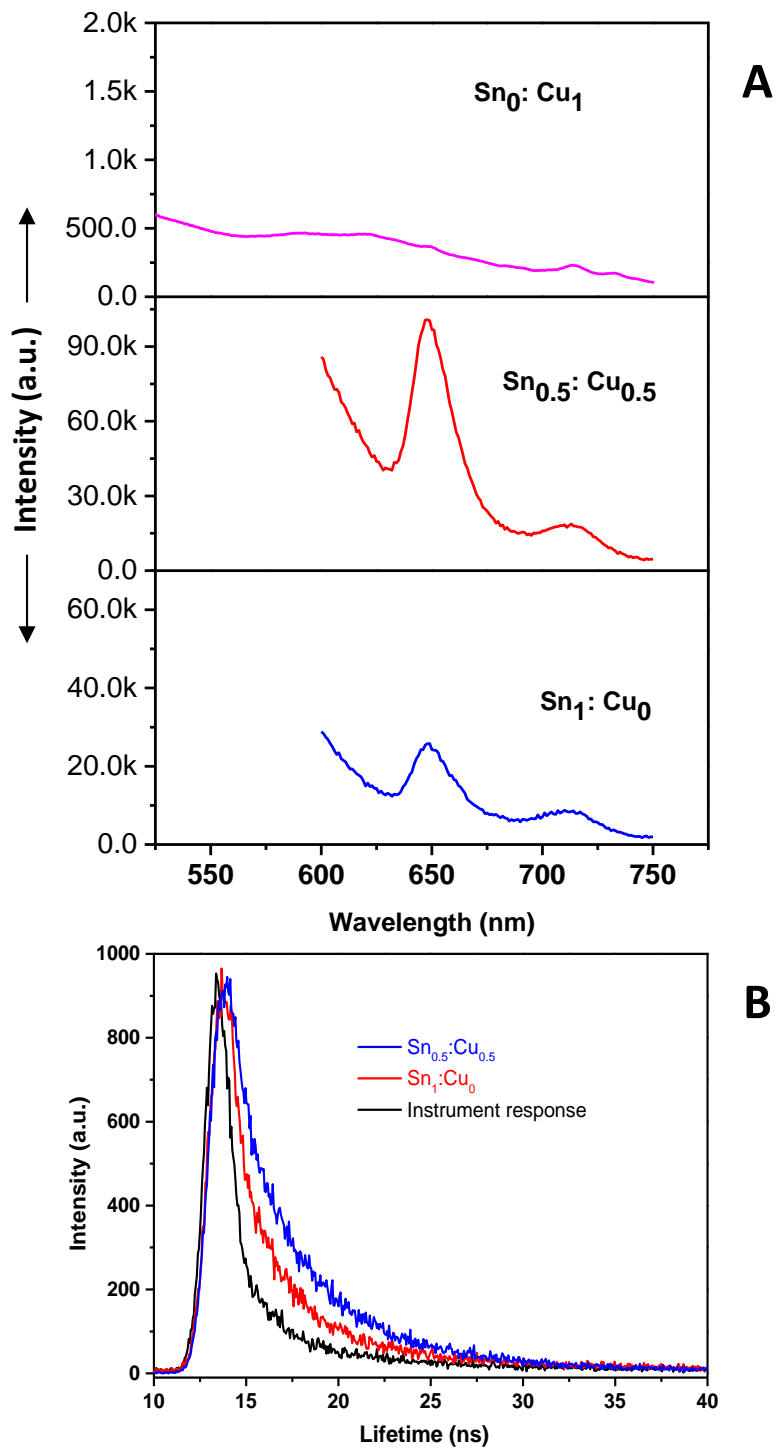


Figure 6.7 (A) Photoluminescence spectra of the perovskite materials and (B) lifetime measurements of the perovskites

Table 6.4 Lifetime components of perovskites, calculated from the lifetime spectra

Sample name	Lifetime (ns)	
	$\tau_1$	$\tau_2$
<b>Sn<sub>1</sub>:Cu<sub>0</sub></b>	1.3 (100%)	-
<b>Sn<sub>0.5</sub>:Cu<sub>0.5</sub></b>	10.2 (80 %)	0.4 (20 %)
<b>Sn<sub>0</sub>:Cu<sub>1</sub></b>	-	-

### 6.3.3 Morphological characterisation

The morphology of films examined by FE-SEM is shown in Figure 6.7 (A-C). It is observed that the Sn<sub>1</sub>:Cu<sub>0</sub> crystals exhibit irregular grains with poorly defined boundaries. The Sn<sub>0</sub>:Cu<sub>1</sub> crystals display a layered structure and exhibit non-homogenous behaviour with poorly defined crystal geometries. But in the case of Sn<sub>0.5</sub>:Cu<sub>0.5</sub>, a well-defined layered structure and crystal geometry are observed with clear crystal boundaries. From SEM-EDX analysis, the fraction of Sn and Cu is estimated as 0.48 and 0.52, respectively (Figure 6.8 and Table 6.5). The TEM images also support the FE-SEM results. Thus, the TEM image of the Sn<sub>0.5</sub>:Cu<sub>0.5</sub> sample shows the layered structure, while the other two samples do not show well-defined structures. The SAED pattern confirms the polycrystalline nature of all three materials. These studies reveal that the addition of copper can alter the crystallisation behaviour of Sn-perovskites and lead to enhanced stability and tailorable properties.

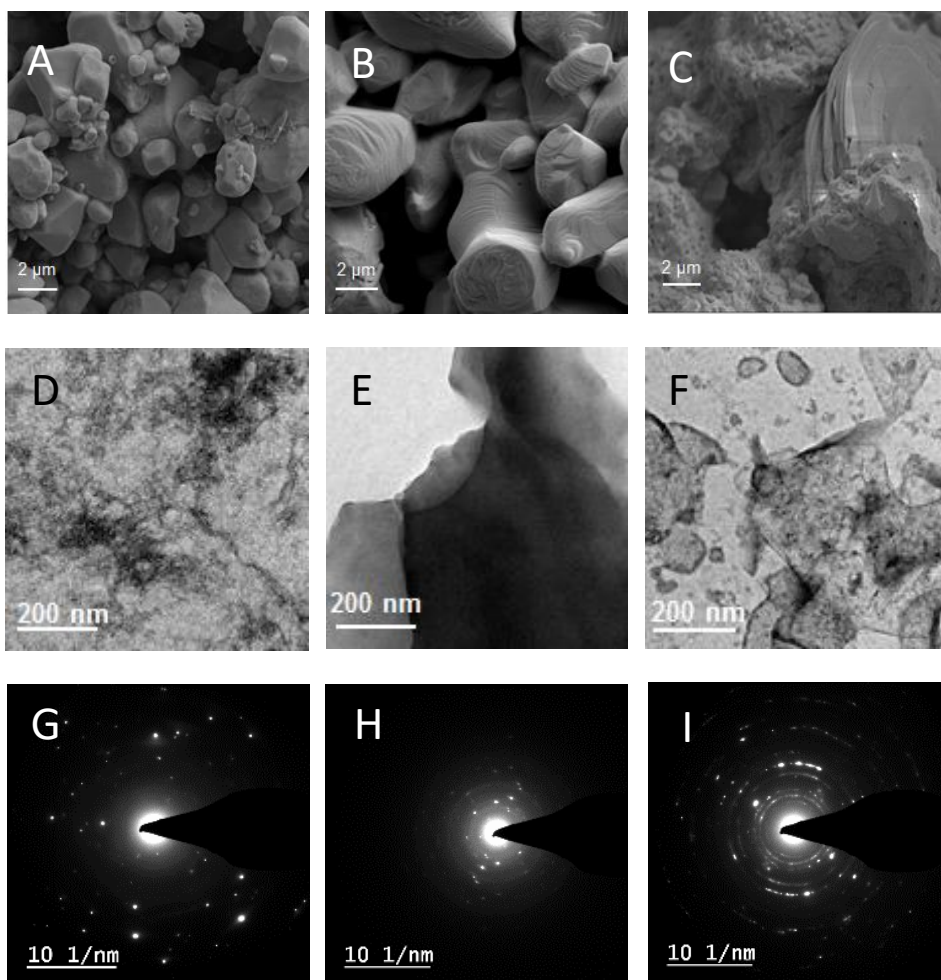


Figure. 6.8 (A)-(C) FE-SEM images of Sn<sub>1</sub>:Cu<sub>0</sub>, Sn<sub>0.5</sub>:Cu<sub>0.5</sub> and Sn<sub>0</sub>:Cu<sub>1</sub>, (D)-(F) TEM images of Sn<sub>1</sub>:Cu<sub>0</sub>, Sn<sub>0.5</sub>:Cu<sub>0.5</sub> and Sn<sub>0</sub>:Cu<sub>1</sub> and (G)-(I) SAED pattern of Sn<sub>1</sub>:Cu<sub>0</sub>, Sn<sub>0.5</sub>:Cu<sub>0.5</sub> and Sn<sub>0</sub>:Cu<sub>1</sub>

Table. 6. 5. The concentration of CuCl<sub>2</sub> (x) and SnBr<sub>2</sub> (1-x) was calculated using the values of copper and tin obtained from SEM-EDX.

Cu from SEM-EDX for Sn <sub>0.5</sub> :Cu <sub>0.5</sub> (%)	CuCl <sub>2</sub> calculated for Sn <sub>0.5</sub> :Cu <sub>0.5</sub> (%)	No. of moles of CuCl <sub>2</sub> (x)	Sn from SEM-EDX (Sn <sub>0.5</sub> :Cu <sub>0.5</sub> ) (%)	Sn calculated for SnBr <sub>2</sub> Sn <sub>0.5</sub> :Cu <sub>0.5</sub> (%)	No. of moles of SnBr <sub>2</sub> (1-x)
10.5	22.44	0.52	18.36	42.7	0.48

### 6.3.4 Computational analysis

Computational studies were carried out using Density Functional Theory (DFT) to predict the minimum energy structures of  $\text{Sn}_{0.5}\text{Cu}_{0.5}$  perovskite. The optimised structures of  $\text{Sn}_1\text{Cu}_0$ ,  $\text{Sn}_{0.5}\text{Cu}_{0.5}$ ,  $\text{Sn}_0\text{Cu}_1$  perovskites are shown in Figures 6.9 A, B and C. The stabilisation energy obtained for the  $\text{Sn}_1\text{Cu}_0$ ,  $\text{Sn}_{0.5}\text{Cu}_{0.5}$  and  $\text{Sn}_0\text{Cu}_1$  is -5368 kJ/mol, -10023 kJ/mol and -4325 kJ/mol, respectively.

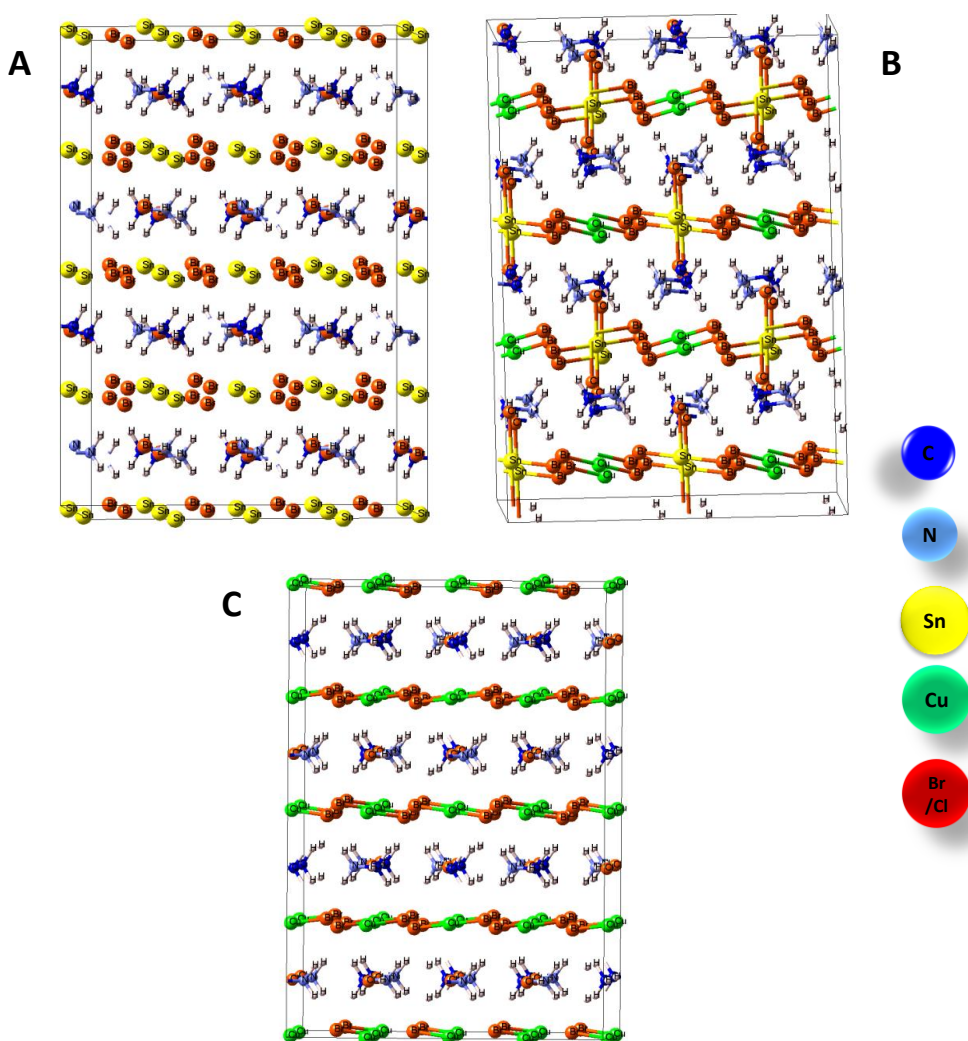


Figure 6.9 Optimised structures (A)  $\text{Sn}_1\text{Cu}_0$ , (B)  $\text{Sn}_{0.5}\text{Cu}_{0.5}$  and (C)  $\text{Sn}_0\text{Cu}_1$

The optimised structures obtained from the DFT method were used to investigate the band structure to compare with the experimental results. It is found that the band structures of these materials are in good agreement with the

experimental results. Band structures of the materials are given in Figure 6.10 A, B and C.

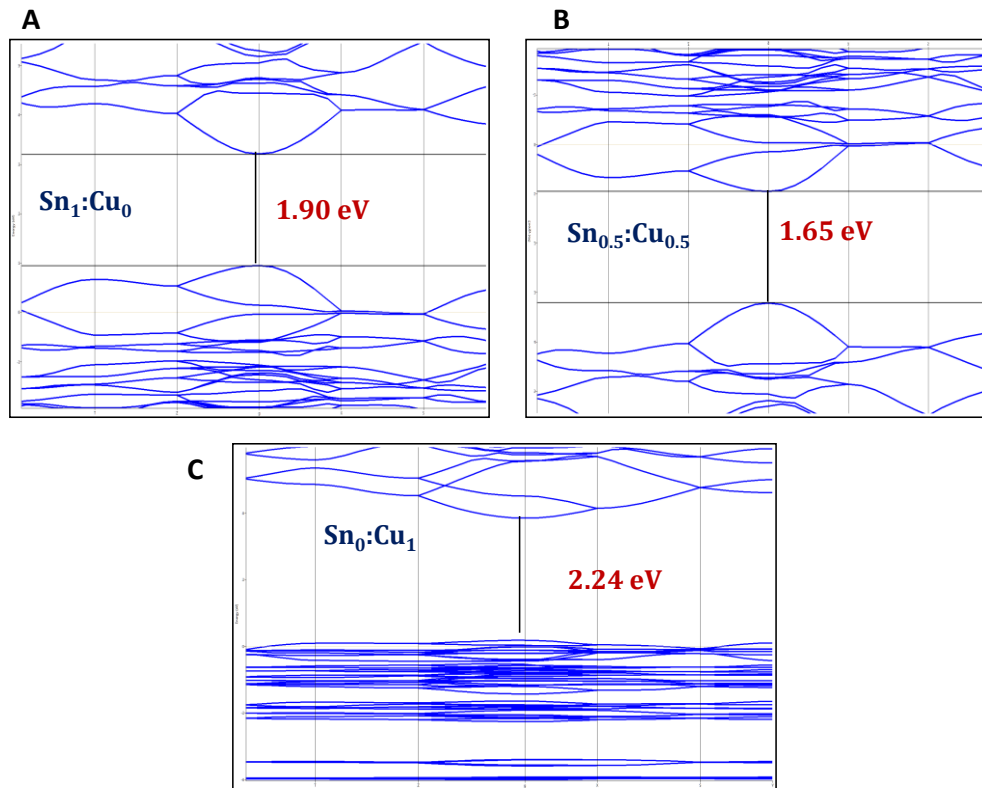


Figure 6.10 A, B and C shows the band structure of the perovskites calculated using DFT by Vienna Ab initio Simulation Package (VASP)

### 6.3.5 Electrical characterisation

To understand the electronic nature of the materials, impedance spectroscopy was performed. The data of the impedance spectroscopy scan are plotted in the Nyquist plot (Nyquist plot, Figure 6.11) starting from the high frequency to the low frequencies, with the high frequency region plotted near the origin of the  $Z'$  vs  $-Z''$  plot.

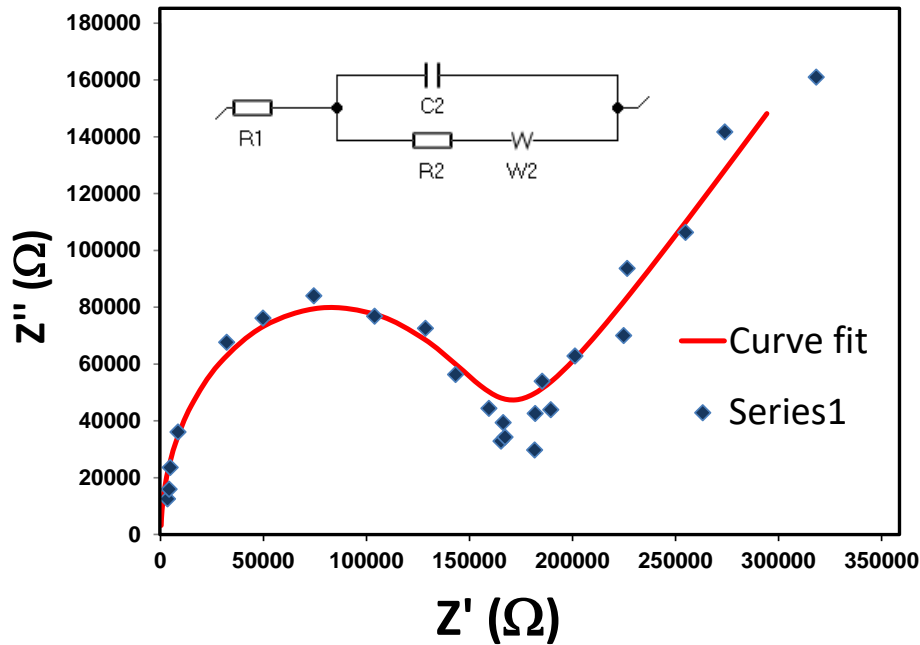


Figure. 6.11. Nyquist plot of Sn<sub>0.5</sub>:Cu<sub>0.5</sub>. *Inset*: equivalent circuit diagram

The high frequency region is mainly associated with the charge transfer resistance at the interface (contacts) or the transport resistance (active material). At the high frequency region on the left-hand side of the plot, the sample's resistivity is measured as 308 Ω cm, which is reported for the typical semiconductor materials (Serway 1998; Krupka 2013). Hence, it is confirmed that the present materials also belong to the category of semiconductors. The photovoltaic performance of the materials was evaluated and presented in Chapter 7.

## 6.4 Conclusions

Mixed perovskite crystals of Sn-perovskite (Sn<sub>1</sub>:Cu<sub>0</sub>), Cu-perovskite (Sn<sub>0</sub>:Cu<sub>1</sub>) and Sn-Cu mixed perovskite (Sn<sub>0.5</sub>:Cu<sub>0.5</sub>) were synthesised and characterised. Cu is chosen as a substitution element for the partial replacement of Sn. The mixed perovskites evidenced characteristics of both 3D and 2D perovskite structures with the change in the lattice spacing in the XRD analysis. The detailed electronic structure of the mixed perovskites and their stability was investigated. The improved optical absorption in the visible region and the lower tendency for oxidation of Sn in the mixed perovskites depict the suitability of

$\text{Sn}_{0.5}\text{Cu}_{0.5}$  systems in photovoltaic and optoelectronic applications compared to the conventional  $\text{CH}_3\text{NH}_3\text{SnBr}_3$ . Computational results complement the experimental data. Stability issues of Sn-based perovskite and the toxicity of Pb in conventional solar cells can be resolved to a considerable extent using mixed Sn-Cu perovskites. The  $\text{Sn}_{0.5}\text{Cu}_{0.5}$  system exhibits great potential with improved environmental stability, tailorable optical properties and facile processing methods, implying its potential in optoelectronic applications.

# **CHAPTER 7**

## **EVALUATION OF PEROVSKITE BASED SOLAR CELLS**

### **7.1 Fabrication of Perovskite Solar Cells**

Perovskite based photovoltaic devices become candidates for replacing silicon-based solar cells due to their high efficiency, low cost and easy processing (Huang, Liu et al. 2021). Reports show that there is tremendous growth in perovskite solar cell technology in terms of efficiency (from 3.8% in 2009 to 25.2% in 2021) (Yoo, Seo et al. 2021). To improve the efficiency of perovskite solar cells, different fabrication methods include spin/spray coating, drop casting, slot die coating, electrode deposition, CVD, thermal vapour deposition, vacuum deposition, screen printing, ink-jet printing etc. have been attempted. (Barrows, Pearson et al. 2014; Lang, Gluba et al. 2015; Wang, Liu et al. 2016; Rong, Ming et al. 2018; Zuo and Ding 2021). The performance of the devices depends on the efficacy of the fabrication techniques and the suitability of the material.

This chapter describes the fabrication of perovskite solar cells using the materials discussed in previous chapters and compares the performance.

#### **7.1.1 Preparation of coating solutions**

##### **7.1.1.1 TiO<sub>2</sub> blocking layer**

A solution of 0.15M titanium diisopropylbisacetylacetonate (TDIP) in butanol was used for preparing TiO<sub>2</sub> layer.

##### **7.1.1.2 Mesoporous layer**

0.6 g of TiO<sub>2</sub> paste was dispersed in 5 mL of anhydrous ethanol by magnetic stirring for 10 min and used for coating.

##### **7.1.1.3 Perovskite precursor solution**

Perovskite solution diluted to ~40 wt% in DMF and used for coating.

#### 7.1.1.4 Hole transport layer (HTM)

The HTM is prepared by adding 72.3 mg spiro-MeOTAD, 28.8  $\mu\text{l}$  of 4-tert-butyl pyridine and 17.5  $\mu\text{l}$  of lithium bis(trifluoromethane sulfonyl) imide (Li-TFSI) solution in 1ml of chlorobenzene. Li-TFSI solution is prepared by dissolving 520 mg Li-TSFI in 1 ml acetonitrile (Sigma–Aldrich, 99.8 %).

## 7.2. Fabrication Steps

### 7.2.1 Masking and etching process

Fluorinated tin oxide (FTO) coated glass plate is used as the substrate for fabrication. FTO glass plate was cut to 2.5 x 2.5 cm dimension and the active area for coating was masked using Kapton tape (Figure 7.1B). Active area and mask area to get a typical pattern is shown in Figure 7.1A.

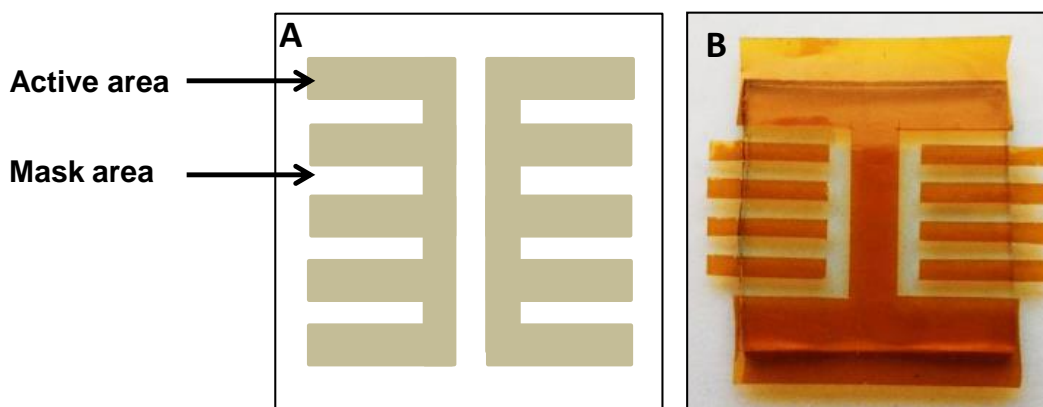


Figure 7.1 (A) Representation of patterned FTO plate after masking and (B) the photograph is showing the masked substrate (using Kapton tape).

The exposed area (after masking) is etched using dry zinc powder and HCl (2M in deionised water) to obtain the required electrode pattern. Zn powder was spread over the exposed FTO glass and 2M HCl was slowly dropped over the Zn powder using a dropper to remove the FTO coating selectively. After the  $\text{H}_2$  evolution has ceased, the substrate was washed with distilled water multiple times and dried under vacuum at 60  $^\circ\text{C}$  (Figure 7.2)

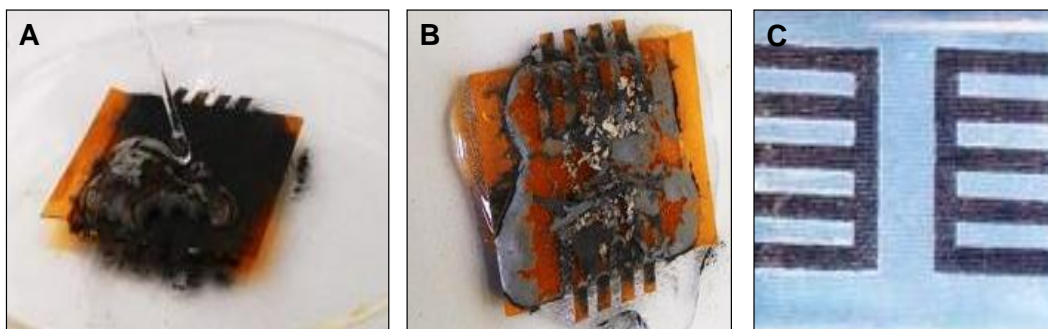


Figure 7.2 (A) Spreading of Zn powder on FTO glass and dropping of HCl solution on it, (B) Evolution of H<sub>2</sub> gas along with the etched FTO (C) the etched FTO glass after cleaning

### 7.2.2 Spin coating

Spin coating is used for depositing thin films on substrates. Material required for coating was dissolved/ dispersed in a solvent. It is spun at a very high speed to generate an even coating with thickness ranging from few nanometres to a few microns in thickness (Tyona 2013). Figure 7.3 shows the spin coating machine (Speciality coating Systems P-6700 series) used for coating the FTO substrates.



Figure 7.3 Spin coating machine

Four different stages of the spin coating method are deposition, spin-up, spin-off and evaporation of the solvent (Figure 7.4). The thickness of a spin

coated film is proportional to the inverse of the spin speed and the relation is as follows:

$$h_f \propto \frac{1}{\sqrt{\omega}}$$

Where  $h_f$  is the thickness of the coating and  $\omega$  is the angular velocity. The thickness of the coating will depend upon the material concentration and solvent evaporation rate (which depends upon the solvent viscosity, vapour pressure, temperature and humidity) and the spin speed (Birnie 2004).

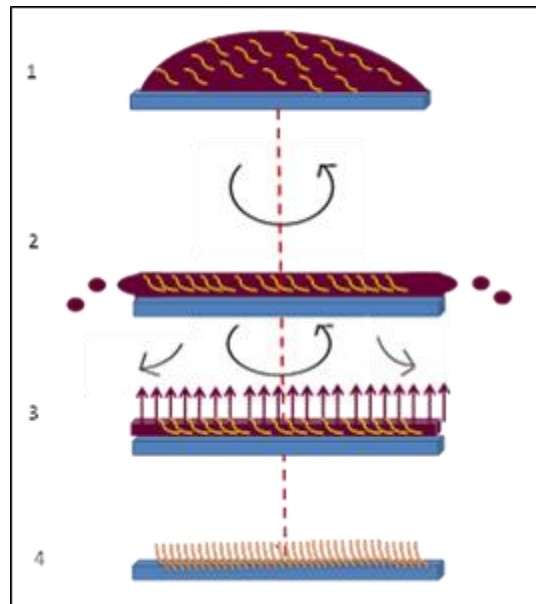


Figure 7.4. Four steps involved spin coating of material (1) A drop of the sample solution added over the substrate, (2) substrate is rotated at very high speed (several thousand rpm) and a majority of solution flew off, (3) Solvent gets dried by airflow leaving a plasticised film and (4) shows the deposited molecules of the sample on the surface of the substrate

There are two different solution dispensing methods in the spin coating. They are (a) Static dispensing method: Solution is dispensed onto the substrate before the spinning starts. (b) Dynamic dispensing method: the substrate is rotated at high speed and then the solution is dispensed onto the spinning substrate. (Tyona 2013).

Other important parameters which affect the film quality are (a) spin speed (rpm), (b) spin duration (sec) and (c) volume of solution ( $\mu\text{l}/\text{spin}$ ). In the present study, the dynamic dispensing method is optimised for coating different layers over FTO substrate. The coating parameters employed for the current study are given in Table. 7.1

Table 7.1 Optimised spin coating parameters for different layers

Layer name	Spinning speed (rpm)	Duration (s)
TiO <sub>2</sub> (blocking layer)	3000	40
TiO <sub>2</sub> (mesoporous layer)	2000	20
Perovskite layer	2000	20
Spiro-MeOTAD (HTM) layer	3000	30

### 7.2.3 Sintering of spin coated layers

The coatings were immediately subjected to sintering to ensure complete evaporation of the solvent and crystallisation after coating each layer. The sintering temperatures for various coatings are listed in Table 7.2.

Table 7.2 Sintering temperature for various layer

Layer	Sintering temperature ( $^{\circ}\text{C}$ )	Sintering time (min)
TiO <sub>2</sub> (blocking layer)	450	10
TiO <sub>2</sub> (mesoporous layer)	500	30
Perovskite layer	100	10

### 7.2.4 Sputtering to prepare counter electrode

Sputtering is a technique in which noble metals like gold or platinum are used as the target. The target is bombarded with heavy gas atoms (usually argon). Atoms ejected from the target by the ionised gas cross the plasma to get deposited

on the substrate kept in the coating unit. The conventional sputter chamber is pumped with a rotary pump. The lowest voltage required for the plasma to strike is applied for the application. (Thornton 1973).

After spin coating and sintering, the cells are masked using a template as shown in Figure 7.5. This design ensures the deposition of gold over the desired areas (the active area just above the HTL). In the present study, sputtering was optimised at 30 mA of current for 30 second duration to get the desired thickness.

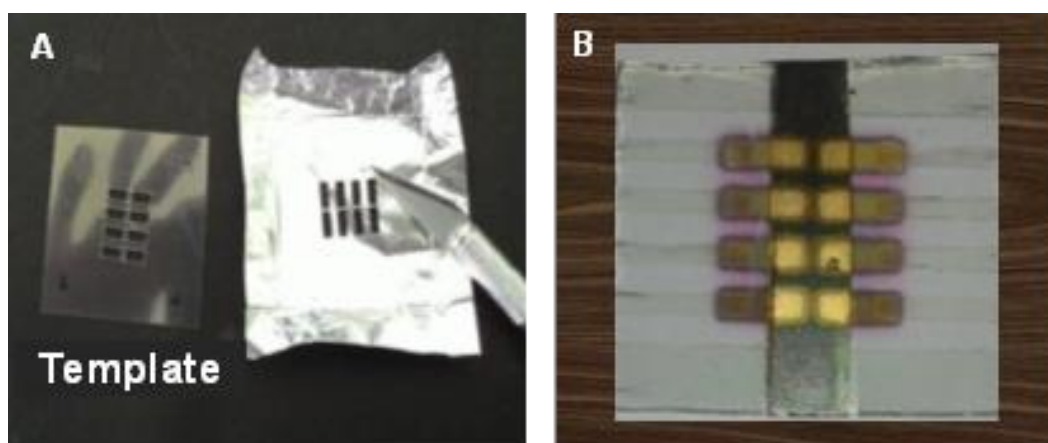


Figure 7.5 (A) Aluminum foil masking (B) the cells after sputtering

Electrical contacts are made using connection legs which act as the positive and negative electrodes. Gold acts as the positive electrode and bare FTO acts as the negative electrode. (Figure 7.6)

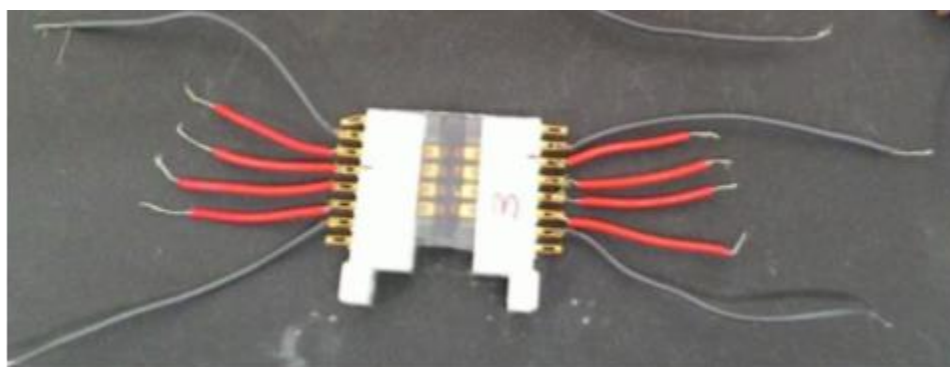


Figure 7.6 The photograph of the cells after attaching the connection leg

## 7.3 Photovoltaic Evaluation

The photovoltaic performance of the devices was monitored using a solar simulator (AM 1.5G, XES40S1, SAN-EI); (Figure 7.7A) and a metal mask (area  $0.15 \text{ cm}^2$ ) was used during the measurement. The scan rate employed was  $0.07 \text{ V/s}$ . The solar simulator was calibrated with a standard Si reference cell (Oriol, PN 91150 V, VLSI standards) before each measurement. The active area is  $0.15 \text{ cm}^2$ . All the tests were carried out under ambient conditions of temperature ( $28\text{--}35 \text{ }^\circ\text{C}$ ) and a relative humidity (RH) of  $70\text{--}80\%$ .

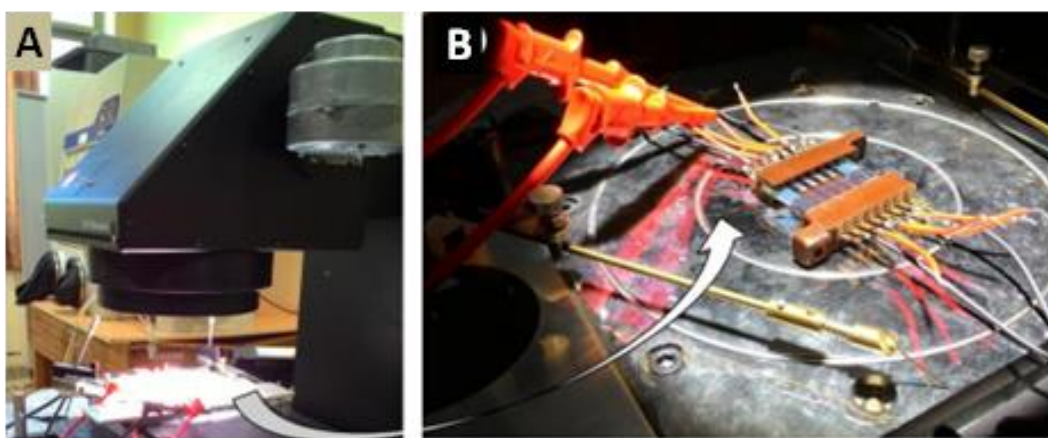


Figure 7.7 Photograph of (A) solar simulator used for the study and (B) shows the solar cells connected to measuring aperture

### 7.3.1 Evaluation of photovoltaic properties of fabricated devices

#### 7.3.1.1 N 719 sensitised methylammonium lead bromide perovskite solar cells

The cells are fabricated using the procedure described in Section 7.2. Figure 7.7A shows different layers of coating and Figure 7.7B shows the complete device. Results of the photovoltaic performance evaluation of N719 dye doped  $\text{MAPbBr}_3$  are listed in Table 7.3. An efficiency of  $\sim 9.94\%$  was observed for N 719 dye-  $\text{MAPbBr}_3$  active material with a consistent voltage  $\sim 0.99 \text{ V}$  and a current of  $\sim 11.44 \text{ mA}$ . Figure 7.8C shows J-V curve of N 719 dye+  $\text{MAPbBr}_3$  and  $\text{MAPbBr}_3$ .

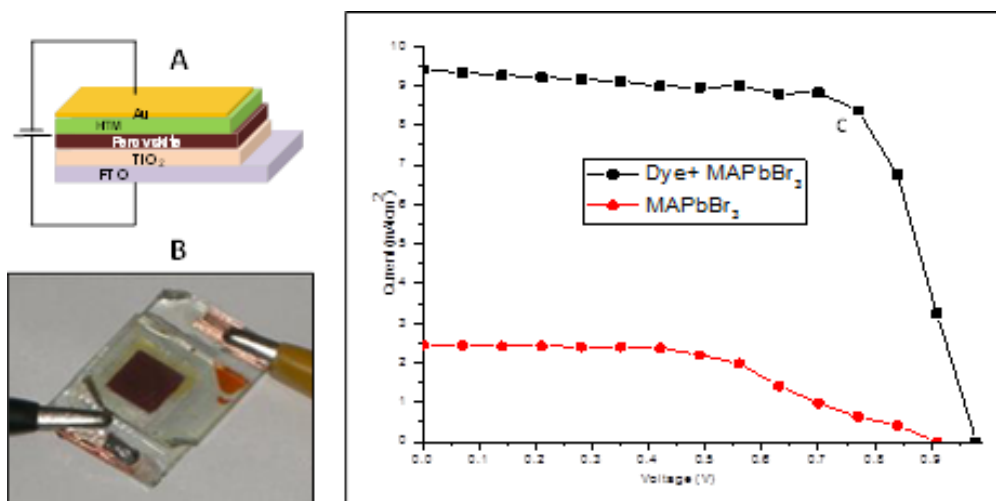


Table 7.3 Photovoltaic parameters under 1 Sun illumination

Cell configuration	Voltage, V <sub>oc</sub> (V)	Current, J <sub>sc</sub> (mA/cm <sup>2</sup> )	Fill Factor	Efficiency (%)
N719 dye + MAPbBr <sub>3</sub>	0.99	11.44	0.87	9.94
	0.99	11.52	0.86	9.81
	0.99	8.35	0.70	5.79
	0.99	9.42	0.68	6.34
	0.99	9.52	0.72	6.79
MAPbBr <sub>3</sub>	0.88	2.66	0.55	1.9
	0.82	1.83	0.68	1.02
	0.91	2.45	0.50	1.16
	0.89	1.65	0.57	0.84
	0.92	3.54	0.41	1.34
N 719 dye alone	0.55	0.08	0.18	0.05
	0.48	0.07	0.19	0.06
	0.52	0.09	0.16	0.08
	0.53	0.10	0.20	0.09
	0.49	0.12	0.18	0.08

### 7.3.1.2. Oligomer assisted synthesized of MASnBr<sub>3</sub>

The photovoltaic performance of the perovskite/polymer solar cells based on CH<sub>3</sub>NH<sub>3</sub>SnBr<sub>3</sub>/PSQ was fabricated and the device architecture is given in Figure 7.9 A. The J-V curve and the corresponding electrical parameters are presented in Figure 7.9 C and Table 7.4, respectively. As seen in Table 7.4, oligomer assisted perovskite shows an open-circuit voltage ( $V_{oc}$ ) of ~1 V and a short circuit current density ( $J_{sc}$ ) of ~0.8 mA/cm<sup>2</sup>, resulting in a power conversion efficiency of ~1.2%. The cell fabricated using CH<sub>3</sub>NH<sub>3</sub>SnBr<sub>3</sub> alone shows a maximum current of 0.28 mA/cm<sup>2</sup> and a fill factor (FF) of less than 30% only, with an average power conversion efficiency of 0.24%.

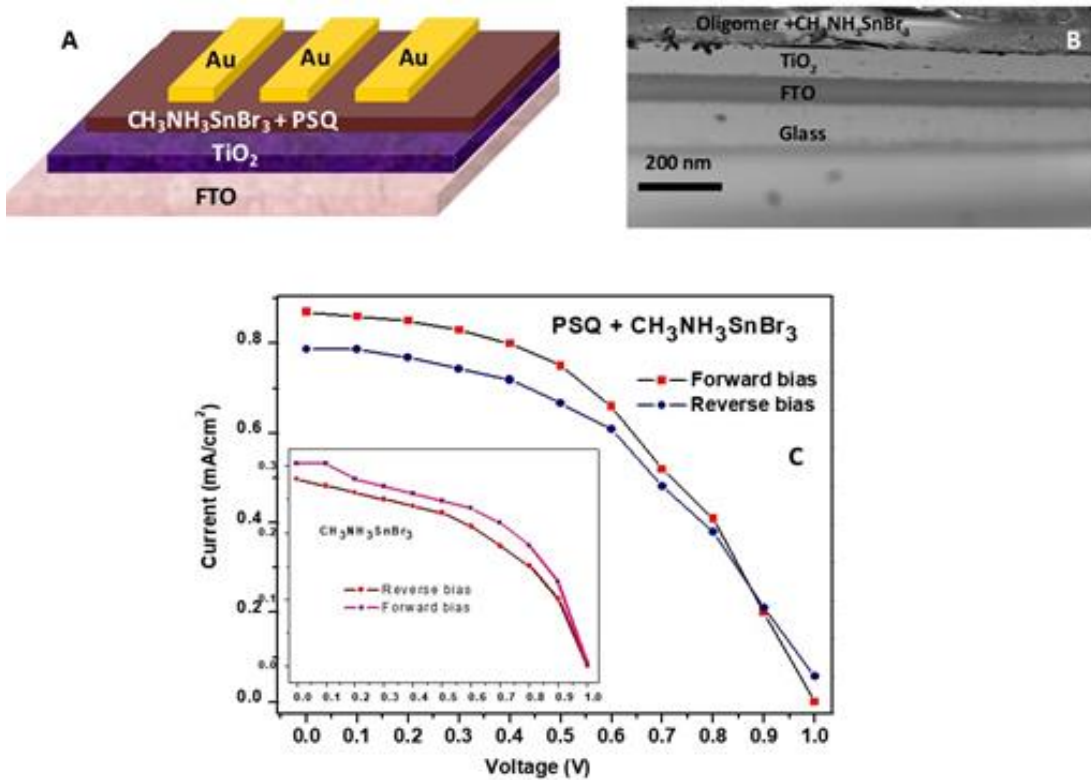


Figure 7.9 (A) Photocurrent observed for FTO/CH<sub>3</sub>NH<sub>3</sub>SnBr<sub>3</sub>/PSQ/Au, (B) J-V curve of FTO/TiO<sub>2</sub>/CH<sub>3</sub>NH<sub>3</sub>SnBr<sub>3</sub>/HTM/Au under 1 Sun illumination and inset of (C) J-V curve of FTO/TiO<sub>2</sub>/CH<sub>3</sub>NH<sub>3</sub>SnBr<sub>3</sub>+PSQ/Au under the same conditions.

Table 7.4 Photovoltaic parameter of CH<sub>3</sub>NH<sub>3</sub>SnBr<sub>3</sub>/PSQ solar cells under 1 Sun illumination

Cell configuration	Voltage, V <sub>oc</sub> (V)	Current, J <sub>sc</sub> (mA/cm <sup>2</sup> )	Fill Factor	Efficiency (%)
FTO/TiO <sub>2</sub> / CH <sub>3</sub> NH <sub>3</sub> SnBr <sub>3</sub> / /PSQ/Au	1.09	4.53	0.38	1.88
	1.01	4.93	0.40	1.99
	1.02	5.40	0.41	2.26
	1.04	5.13	0.38	2.03
	1.02	5.80	0.35	2.07
FTO/TiO <sub>2</sub> / CH <sub>3</sub> NH <sub>3</sub> SnBr <sub>3</sub> / HTM/Au	0.81	1.47	0.40	0.48
	0.85	1.20	0.22	0.22
	0.88	1.67	0.12	0.18
	0.87	1.53	0.25	0.33

### 7.3.1.3 Tin-Copper mixed metal cation based solar cells

Solar cells are fabricated using tin-copper (Sn<sub>0.5</sub>:Cu<sub>0.5</sub>) mixed cation perovskite as an active layer. The construction of the solar cell is the same as given in Section 7.3.1.1 (Figure 7.8A). The different layers of materials were spin-coated over fluorine-doped tin oxide (FTO) glass plate under normal atmospheric conditions (Temperature: 28-32°C, RH~60%). The roughness of the perovskite films was estimated from the AFM topographic images and is found to be less than 100 nm (Figure 7.10 A, B and C). The mixed perovskite exhibited the lowest roughness and uniform morphology (Figure 7.10 D) due to the layered structure. The cross-sectional image of the cell showing various layers is given in Fig. 7.10 E.

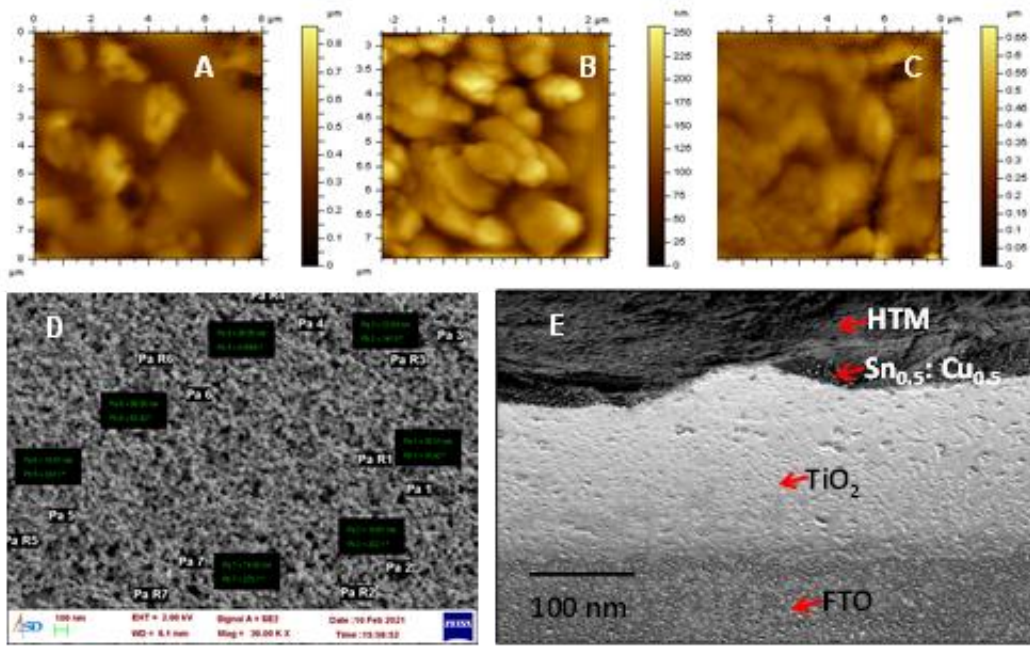


Figure 7.10 (A), (B) and (C) are AFM images of  $\text{Sn}_{0.5}\text{Cu}_{0.5}$  layer; (D) FE-SEM image of  $\text{Sn}_{0.5}\text{Cu}_{0.5}$  over FTO substrate and (E) shows the cross-sectional image of different layers of coating of the solar cell.

The photovoltaic parameters of the device were measured under 1 Sun illumination. For comparison, tin- and copper- individual perovskites layers are also used as the active layer and the photovoltaic parameters were evaluated (Table 7.5). To the best of our knowledge, this is the first attempt to evaluate the photovoltaic effect in tin-copper mixed perovskites. The hysteresis of the cell was assessed by performing a forward scan and a reverse scan. Hysteresis was less for tin-copper perovskite active layers. The device made of tin and copper ( $\text{Sn}_{0.5}\text{Cu}_{0.5}$ ) exhibited a power conversion efficiency of  $\sim 2\%$  with an open-circuit voltage of  $\sim 0.95$  V, short circuit current of  $\sim 4.3$   $\text{mA}/\text{cm}^2$  and a fill factor of  $\sim 0.55$ . The devices made of tin perovskite ( $\text{Sn}_1\text{Cu}_0$ ) and copper perovskite ( $\text{Sn}_0\text{Cu}_1$ ) exhibited lower efficiencies. The expected efficiency is not achieved for  $\text{Sn}_{0.5}\text{Cu}_{0.5}$  based perovskite solar cells due to the formation of  $\text{Cu}^+$  trap states, which is confirmed from the XPS analysis. However, the enhanced environmental stability and tailorable optical properties reveal the potential of mixed perovskites for optoelectronic applications.

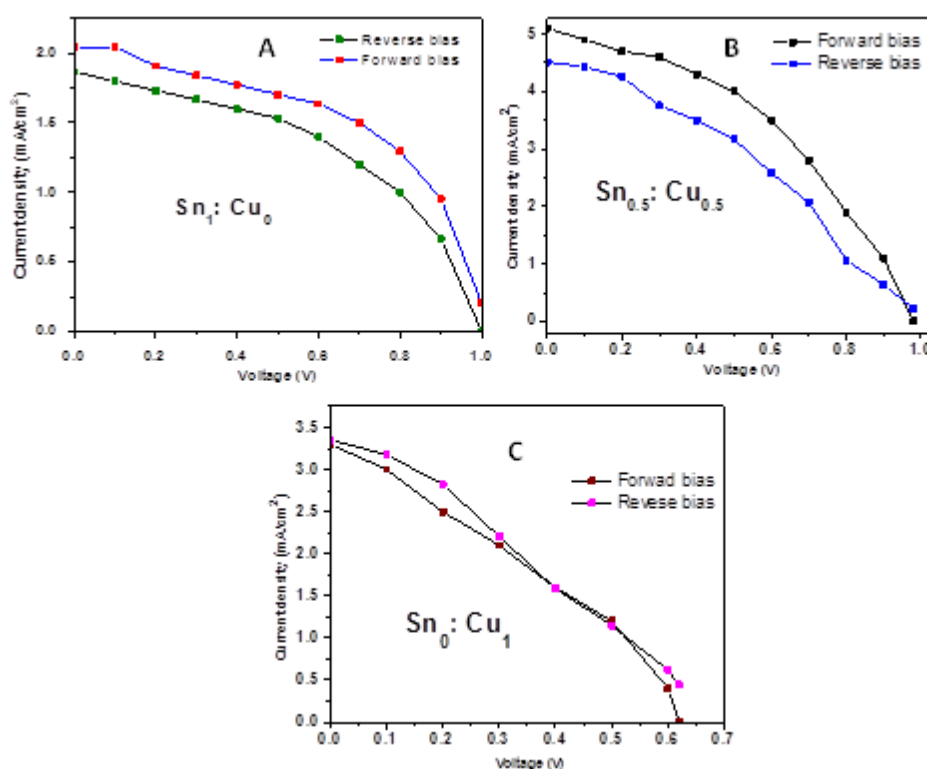


Figure 7.11. J-V curve of the cell fabricated using various tin-copper perovskite under 1 Sun illumination

Table 7.5. Photovoltaic parameters of tin-copper mixed metal cation based solar cells under 1 Sun illumination

Cell configuration	Voltage, $V_{oc}$ (V)	Current, $J_{sc}$ (mA/cm <sup>2</sup> )	Fill Factor	Efficiency (%)
FTO/TiO <sub>2</sub> /Sn <sub>1</sub> :Cu <sub>0</sub> /HTM/Au	0.81	1.5	0.40	0.48
	0.85	1.2	0.22	0.22
	0.88	1.7	0.12	0.18
	0.87	1.5	0.25	0.33
	0.82	1.4	0.28	0.33
FTO/TiO <sub>2</sub> /Sn <sub>0.5</sub> :Cu <sub>0.5</sub> /HTM/Au	0.95	4.3	0.52	2.12
	0.94	4.0	0.50	1.88
	0.91	3.6	0.40	1.31
	0.92	4.2	0.45	1.73
	0.92	4.6	0.40	1.69

FTO/TiO <sub>2</sub> / Sn <sub>0</sub> :Cu <sub>1</sub> /HTM/Au	0.66	2.2	0.40	0.58
	0.62	3.3	0.33	0.67
	0.55	3.1	0.28	0.48
	0.65	2.9	0.26	0.49
	0.68	2.3	0.32	0.50

## 7.4 Conclusions

Solar cells are fabricated using newly developed materials as the active layer and device performance was compared. N 719 dye sensitised perovskite has shown maximum efficiency of ~9.9 % with a  $V_{oc}$  of 0.99 V and  $J_{sc}$  of ~11mA. A new device configuration was also developed by replacing the hole transport layer, where the perovskite crystallises within an oligomer matrix. Here oligomer itself acts as a hole transport layer and a power conversion efficiency of ~1.2% is obtained. Mixed metal cation of tin-copper shows efficiency of ~2%. Further improvement in the device performance can be achieved by fine-tuning the fabrication procedures.



## CHAPTER 8

### CONCLUSIONS AND FUTURE DIRECTIONS

#### 8.1 Conclusion

To understand the perovskite semiconductor technology in detail and explore the different possibilities of altering the perovskites by changing the cation and anion part of the perovskites was attempted in the present thesis.

In summary, hybrid organic/inorganic perovskites of lead-halide and tin-halide were synthesised using different strategies. A comprehensive literature survey was presented in Chapter 1 along with the objectives of the present work. Chapter 2 deals with materials and methods.

Chapter 3 deals with the synthesis of perovskites using imidazolium based ionic liquids. The 2D layered perovskites of lead, incorporated with imidazolium based ILs are reported for the first time. These materials are non-hygroscopic and exhibited excellent environmental stability. These novel compounds absorbing in the UV region showed good photocurrent, offering potential as active material in optoelectronic applications.

Chapter 4 describes methylammonium lead bromide synthesis using a dye sensitizer. The optical and photophysical properties of methylammonium lead bromide perovskite were altered using a Ru based N719 dye. The structural, optical and photovoltaic properties were investigated in detail. Dye sensitised  $\text{CH}_3\text{NH}_3\text{PbBr}_3$  shows changes in the UV-Visible absorption and the fluorescence emission properties indicating changes in HOMO-LUMO energy levels in dye sensitized  $\text{CH}_3\text{NH}_3\text{PbBr}_3$ . Thus a novel approach to improve the properties of the  $\text{CH}_3\text{NH}_3\text{PbBr}_3$  is established.

Chapter 5 explains the synthesis of a novel, oligomeric silsesquioxane (PSQ) encapsulated  $\text{CH}_3\text{NH}_3\text{SnBr}_3$  perovskites were synthesised. The PSQ demonstrates appropriate energy levels, good solubility for perovskite precursors, easy fabrication and excellent transparency in the UV-Visible and NIR regions

and enhances the environmental stability of the material which are the essential factors influencing the performance of photovoltaic devices.

The stability of a Sn-based perovskite was enhanced by the partial replacement of Sn with Cu is explained in chapter 6. The detailed electronic structure of the mixed perovskites and their stability was investigated. The improved optical absorption in the visible region and the lower tendency for oxidation of Sn in the mixed perovskites depict the suitability of mixed tin-copper perovskites in photovoltaic and optoelectronic applications compared to the conventional  $\text{CH}_3\text{NH}_3\text{SnBr}_3$ . Stability issues of Sn-based perovskite and the toxicity of Pb in conventional solar cells, can be resolved to a considerable extent using mixed Sn-Cu perovskites. The mixed tin-copper perovskite system exhibits great potential with improved environmental stability, tailorable optical properties and facile processing methods, implying its potential in optoelectronic applications. These works a new class of stable perovskite materials that can be used for photovoltaic and optoelectronic applications.

Chapter 7 deals with the steps of fabrication of solar cells and methodology adopted for fabrication processes. All the solar cells were fabricated using the newly synthesized materials as the active layer. Ionic liquid based 2D perovskite absorbs in the UV region only. Out of all the materials, dye sensitized solar cells showed maximum efficiency of ~9.9 %.

## **8.2 Future Perspectives**

Metal halide perovskites have fascinated scientists over the past due to their high-quality optoelectronic properties, surprising processing strategies i.e., materials processed from solution and at low temperature and also functions as the light absorbing layers in highly efficient photovoltaic (PV) devices. Perovskites typically adopt a 3D crystal structure with a stoichiometry of  $\text{ABX}_3$ . The hybrid organic-inorganic perovskite compounds with methylammonium (MA) or formamidinium (FA) as the A cation and lead or tin as the B cation and halide anion ( $\text{Cl}^-$ ,  $\text{Br}^-$  or  $\text{I}^-$ ) showed the best efficiency in solar cell devices. A variety of compositions of perovskites and their properties have raised great interest for the researcher community. From the first reported perovskite solar cells to present

single-junction cells are already approaching power conversion efficiency (PCE) of 23%. But the long-term stability of perovskite solar cells has raised major concern which hinders the commercialization. As the properties of perovskites are not yet fully understood, further research are needed to explore the materials as well as the device level technology.

A few of the new systems to be studied include: (1) perovskite-based solar cells using suitable metal organic frameworks (MOFs) as sensitisers to achieve better environmental stability and efficiency, (2) Introduce different electron transport layers (such as SnO<sub>2</sub>) to achieve the best performance, (3) MXene –HOPs composite can also be explored as active material in solar cell devices.



## REFERENCES

1. Ahmadi, M., T. Wu, et al. (2017). "A review on organic–inorganic halide perovskite photodetectors: device engineering and fundamental physics." *Advanced Materials* **29**(41): 1605242.
2. Bhalla, A., R. Guo, et al. (2000). "The perovskite structure—a review of its role in ceramic science and technology." *Materials research innovations* **4**(1): 3-26.
3. Bhaumik, S., S. A. Veldhuis, et al. (2016). "Highly stable, luminescent core–shell type methylammonium–octylammonium lead bromide layered perovskite nanoparticles." *Chemical communications* **52**(44): 7118-7121.
4. Bibes, M. and A. Barthelemy (2007). "Oxide spintronics." *IEEE Transactions on Electron Devices* **54**(5): 1003-1023.
5. Brenner, T. M. (2016). "D. a. Egger, L. Kronik, G. Hodes, D. Cahen." *Nat. Rev. Mater* **1**: 15007.
6. Carpenter, M. A. and C. J. Howard (2009). "Symmetry rules and strain/order-parameter relationships for coupling between octahedral tilting and cooperative Jahn–Teller transitions in ABX<sub>3</sub> perovskites. I. Theory." *Acta Crystallographica Section B: Structural Science* **65**(2): 134-146.
7. Chen, Q. and N. De Marco (2015). "Y.(Michael) Yang, T." B. Song, C.-C. Chen, H. Zhao, Z. Hong, H. Zhou and Y. Yang, *Nano Today* **10**: 355-396.
8. Cheng, Z. and J. Lin (2010). "Layered organic–inorganic hybrid perovskites: structure, optical properties, film preparation, patterning and templating engineering." *CrystEngComm* **12**(10): 2646-2662.
9. de Mello Donegá, C., P. Liljeroth, et al. (2005). "Physicochemical evaluation of the hot-injection method, a synthesis route for monodisperse nanocrystals." *Small* **1**(12): 1152-1162.
10. Fang, Y., Q. Dong, et al. (2015). "Highly narrowband perovskite single-crystal photodetectors enabled by surface-charge recombination." *Nature photonics* **9**(10): 679-686.
11. Filip, M. R., G. E. Eperon, et al. (2014). "Steric engineering of metal-halide perovskites with tunable optical band gaps." *Nature communications* **5**(1): 1-9.
12. Frost, J. M., K. T. Butler, et al. (2014). "Atomistic origins of high-performance in hybrid halide perovskite solar cells." *Nano letters* **14**(5): 2584-2590.
13. Galkowski, K., A. Mitioglu, et al. (2016). "Determination of the exciton binding energy and effective masses for methylammonium and formamidinium lead tri-halide perovskite semiconductors." *Energy & Environmental Science* **9**(3): 962-970.

14. Gao, X., X. Zhang, et al. (2019). "Ruddlesden–Popper Perovskites: Synthesis and Optical Properties for Optoelectronic Applications." *Advanced Science* **6**(22): 1900941.
15. Gedamu, D., I. M. Asuo, et al. (2018). "Solvent-antisolvent ambient processed large grain size perovskite thin films for high-performance solar cells." *Scientific reports* **8**(1): 1-11.
16. Hao, F., C. C. Stoumpos, et al. (2014). "Lead-free solid-state organic–inorganic halide perovskite solar cells." *Nature photonics* **8**(6): 489-494.
17. Hsiao, Y. C., T. Wu, et al. (2015). "Magneto-optical studies on spin-dependent charge recombination and dissociation in perovskite solar cells." *Advanced Materials* **27**(18): 2899-2906.
18. Jena, A. K., A. Kulkarni, et al. (2019). "Halide perovskite photovoltaics: background, status, and future prospects." *Chemical reviews* **119**(5): 3036-3103.
19. Ju, M.-G., J. Dai, et al. (2017). "Lead-free mixed tin and germanium perovskites for photovoltaic application." *Journal of the American Chemical Society* **139**(23): 8038-8043.
20. Krishnamoorthy, T., H. Ding, et al. (2015). "Lead-free germanium iodide perovskite materials for photovoltaic applications." *Journal of Materials Chemistry A* **3**(47): 23829-23832.
21. Kwon, S. G. and T. Hyeon (2011). "Formation mechanisms of uniform nanocrystals via hot-injection and heat-up methods." *Small* **7**(19): 2685-2702.
22. Liu, M., M. B. Johnston, et al. (2013). "Efficient planar heterojunction perovskite solar cells by vapour deposition." *Nature* **501**(7467): 395-398.
23. Liu, X.-K., W. Xu, et al. (2020). "Metal halide perovskites for light-emitting diodes." *Nature Materials*: 1-12.
24. Liu, X., L. Cao, et al. (2019). "A review of perovskite photovoltaic materials' synthesis and applications via chemical vapor deposition method." *Materials* **12**(20): 3304.
25. Ma, H. H., M. Imran, et al. (2018). "Growth of metal halide perovskite, from nanocrystal to micron-scale crystal: A review." *Crystals* **8**(5): 182.
26. Mao, L., C. C. Stoumpos, et al. (2018). "Two-dimensional hybrid halide perovskites: principles and promises." *Journal of the American Chemical Society* **141**(3): 1171-1190.
27. Murphy, D., S. Sunshine, et al. (1987). "New superconducting cuprate perovskites." *Physical review letters* **58**(18): 1888.
28. Nayak, P. K., D. T. Moore, et al. (2016). "Mechanism for rapid growth of organic–inorganic halide perovskite crystals." *Nature communications* **7**(1): 1-8.

29. Nie, W., H. Tsai, et al. (2015). "High-efficiency solution-processed perovskite solar cells with millimeter-scale grains." *Science* **347**(6221): 522-525.
30. Niu, G., X. Guo, et al. (2015). "Review of recent progress in chemical stability of perovskite solar cells." *Journal of Materials Chemistry A* **3**(17): 8970-8980.
31. Noh, J. H., S. H. Im, et al. (2013). "Chemical management for colorful, efficient, and stable inorganic–organic hybrid nanostructured solar cells." *Nano letters* **13**(4): 1764-1769.
32. Ou, Q., X. Bao, et al. (2019). "Band structure engineering in metal halide perovskite nanostructures for optoelectronic applications." *Nano Materials Science* **1**(4): 268-287.
33. Parola, S., B. Julián-López, et al. (2016). "Optical properties of hybrid organic-inorganic materials and their applications." *Advanced Functional Materials* **26**(36): 6506-6544.
34. Prochazkova, A. J., M. C. Scharber, et al. (2020). "Synthesis conditions influencing formation of MAPbBr<sub>3</sub> perovskite nanoparticles prepared by the ligand-assisted precipitation method." *Scientific reports* **10**(1): 1-12.
35. Pu, Y., F. Cai, et al. (2018). "Colloidal synthesis of semiconductor quantum dots toward large-scale production: a review." *Industrial & Engineering Chemistry Research* **57**(6): 1790-1802.
36. Ramadass, N. (1978). "ABO<sub>3</sub>-type oxides—Their structure and properties—A bird's eye view." *Materials Science and Engineering* **36**(2): 231-239.
37. Rao, C., A. Cheetham, et al. (2008). "Hybrid inorganic–organic materials: a new family in condensed matter physics." *Journal of Physics: Condensed Matter* **20**(8): 083202.
38. Saidaminov, M. I., A. L. Abdelhady, et al. (2015). "High-quality bulk hybrid perovskite single crystals within minutes by inverse temperature crystallization." *Nature communications* **6**(1): 1-6.
39. Schmidt, L. C., A. Pertegás, et al. (2014). "Nontemplate synthesis of CH<sub>3</sub>NH<sub>3</sub>PbBr<sub>3</sub> perovskite nanoparticles." *Journal of the American Chemical Society* **136**(3): 850-853.
40. Shamsi, J., A. S. Urban, et al. (2019). "Metal halide perovskite nanocrystals: synthesis, post-synthesis modifications, and their optical properties." *Chemical reviews* **119**(5): 3296-3348.
41. Shannon, R. D. (1976). "Revised effective ionic radii and systematic studies of interatomic distances in halides and chalcogenides." *Acta crystallographica section A: crystal physics, diffraction, theoretical and general crystallography* **32**(5): 751-767.
42. Shi, P., Y. Ding, et al. (2019). "Template-Assisted Formation of High-Quality  $\alpha$ -Phase HC (NH<sub>2</sub>)<sub>2</sub>PbI<sub>3</sub> Perovskite Solar Cells." *Advanced Science* **6**(21): 1901591.

43. Shirayama, M., M. Kato, et al. (2016). "Degradation mechanism of  $\text{CH}_3\text{NH}_3\text{PbI}_3$  perovskite materials upon exposure to humid air." *Journal of Applied Physics* **119**(11): 115501.
44. Smith, A. and A. Welch (1960). "Some mixed metal oxides of perovskite structure." *Acta Crystallographica* **13**(8): 653-656.
45. Stoumpos, C. C., C. D. Malliakas, et al. (2013). "Semiconducting tin and lead iodide perovskites with organic cations: phase transitions, high mobilities, and near-infrared photoluminescent properties." *Inorganic chemistry* **52**(15): 9019-9038.
46. Sun, S., D. Yuan, et al. (2016). "Ligand-mediated synthesis of shape-controlled cesium lead halide perovskite nanocrystals via reprecipitation process at room temperature." *ACS nano* **10**(3): 3648-3657.
47. Sutherland, B. R. and E. H. Sargent (2016). "Perovskite photonic sources." *Nature Photonics* **10**(5): 295.
48. Tan, T.-Y., B. J. Kennedy, et al. (2012). "Impact of Jahn-Teller active  $\text{Mn}^{3+}$  on strain effects and phase transitions in  $\text{Sr}_{0.65}\text{Pr}_{0.35}\text{MnO}_3$ ." *Physical Review B* **85**(10): 104107.
49. Tang, X., Z. Hu, et al. (2017). "Perovskite  $\text{CsPb}_2\text{Br}_5$  microplate laser with enhanced stability and tunable properties." *Advanced Optical Materials* **5**(3): 1600788.
50. Tian, X., Y. Zhang, et al. (2020). "Two-dimensional organic-inorganic hybrid Ruddlesden-Popper perovskite materials: preparation, enhanced stability, and applications in photodetection." *Sustainable Energy & Fuels* **4**(5): 2087-2113.
51. Travis, W., E. Glover, et al. (2016). "On the application of the tolerance factor to inorganic and hybrid halide perovskites: a revised system." *Chemical Science* **7**(7): 4548-4556.
52. Tyagi, P., S. M. Arveson, et al. (2015). "Colloidal organohalide perovskite nanoplatelets exhibiting quantum confinement." *The journal of physical chemistry letters* **6**(10): 1911-1916.
53. Wang, Z., A. M. Ganose, et al. (2019). "Two-dimensional eclipsed arrangement hybrid perovskites for tunable energy level alignments and photovoltaics." *Journal of Materials Chemistry C* **7**(17): 5139-5147.
54. Wu, Y., W. Chen, et al. (2018). "The impact of hybrid compositional film/structure on organic-inorganic Perovskite solar cells." *Nanomaterials* **8**(6): 356.
55. Xia, H., S. Tong, et al. (2018). "Flexible and air-stable perovskite network photodetectors based on  $\text{CH}_3\text{NH}_3\text{PbI}_3/\text{C}_8\text{BTBT}$  bulk heterojunction." *Applied Physics Letters* **112**(23): 233301.

56. Yamada, Y., T. Nakamura, et al. (2014). "Photocarrier recombination dynamics in perovskite CH<sub>3</sub>NH<sub>3</sub>PbI<sub>3</sub> for solar cell applications." *Journal of the American Chemical Society* **136**(33): 11610-11613.
57. Ye, M., X. Hong, et al. (2016). "Recent advancements in perovskite solar cells: flexibility, stability and large scale." *Journal of Materials Chemistry A* **4**(18): 6755-6771.
58. Yoo, J. J., G. Seo, et al. (2021). "Efficient perovskite solar cells via improved carrier management." *Nature* **590**(7847): 587-593.
59. Yuan, Y., T. Li, et al. (2017). "Anomalous photovoltaic effect in organic-inorganic hybrid perovskite solar cells." *Science advances* **3**(3): e1602164.
60. Zhang, Q., R. Su, et al. (2017). "Advances in small perovskite-based lasers." *Small Methods* **1**(9): 1700163.
61. Zhao, Z., F. Gu, et al. (2017). "Mixed-organic-cation tin iodide for lead-free perovskite solar cells with an efficiency of 8.12%." *Advanced Science* **4**(11): 1700204.
62. Zhou, C., H. Lin, et al. (2019). "Low dimensional metal halide perovskites and hybrids." *Materials Science and Engineering: R: Reports* **137**: 38-65.
63. Zhou, Z., S. Pang, et al. (2016). "The fabrication of formamidinium lead iodide perovskite thin films via organic cation exchange." *Chemical communications* **52**(19): 3828-3831.
64. Becke, A. D. (1996). "Density-functional thermochemistry. IV. A new dynamical correlation functional and implications for exact-exchange mixing." *The Journal of chemical physics* **104**(3): 1040-1046.
65. Blöchl, P. E. (1994). "Projector augmented-wave method." *Physical review B* **50**(24): 17953.
66. Frisch, M., G. Trucks, et al. (2009). "Wallingford." CT: Gaussian Inc.
67. Hafdallah, A., F. Yanineb, et al. (2011). "In doped ZnO thin films." *Journal of Alloys and Compounds* **509**(26): 7267-7270.
68. Kresse, G. and J. Furthmüller (1996). "Efficiency of ab-initio total energy calculations for metals and semiconductors using a plane-wave basis set." *Computational materials science* **6**(1): 15-50.
69. Leonat, L., G. Sbarcea, et al. (2013). "Cyclic voltammetry for energy levels estimation of organic materials." *UPB Sci Bull Ser B* **75**: 111-118
70. Perdew, J. P., K. Burke, et al. (1996). "Generalised gradient approximation made simple." *Physical review letters* **77**(18): 3865. Becke, A. D. (1996). "Density-functional thermochemistry. IV. A new dynamical correlation functional and implications for exact-exchange mixing." *The Journal of chemical physics* **104**(3): 1040-1046.

71. Bonamartini Corradi, A., A. M. Ferrari, et al. (2001). "An additional structural and electrical study of polymeric haloplumbates (II) with heterocyclic diprotonated amines." *Inorganic chemistry* **40**(2): 218-223.
72. Chen, Y., Y. Sun, et al. (2018). "2D Ruddlesden–Popper perovskites for optoelectronics." *Advanced Materials* **30**(2): 1703487.
73. Coleman, F., G. Feng, et al. (2013). "Lead (II) chloride ionic liquids and organic/inorganic hybrid materials—a study of chloroplumbate (II) speciation." *Dalton Transactions* **42**(14): 5025-5035.
74. Colodrero, R. M., P. Olivera-Pastor, et al. (2010). "Structural mapping and framework interconversions in 1D, 2D, and 3D divalent metal R, S-hydroxyphosphonoacetate hybrids." *Inorganic chemistry* **49**(2): 761-768.
75. Cortecchia, D., S. Neutzner, et al. (2017). "Broadband emission in two-dimensional hybrid perovskites: The role of structural deformation." *Journal of the American Chemical Society* **139**(1): 39-42.
76. Dobrzycki, L. and K. Woźniak (2008). "Inorganic–organic hybrid salts of diaminobenzenes and related cations." *CrystEngComm* **10**(5): 577-589.
77. Faustini, M., L. Nicole, et al. (2018). "History of organic–inorganic hybrid materials: prehistory, art, science, and advanced applications." *Advanced Functional Materials* **28**(27): 1704158.
78. Feng, R., D. Zhao, et al. (2010). "Revisiting characteristics of ionic liquids: a review for further application development." *Journal of Environmental Protection* **1**(02): 95.
79. Frisch, M., G. Trucks, et al. (2009). "Wallingford." CT: Gaussian Inc.
80. Goossens, K., K. Lava, et al. (2016). "Ionic liquid crystals: versatile materials." *Chemical reviews* **116**(8): 4643-4807.
81. Hayashi, S., R. Ozawa, et al. (2003). "Raman spectra, crystal polymorphism, and structure of a prototype ionic-liquid [bmim] Cl." *Chemistry letters* **32**(6): 498-499.
82. Holbrey, J. D., W. M. Reichert, et al. (2004). "Crystal structures of imidazolium bis (trifluoromethanesulfonyl) imide 'ionic liquid' salts: the first organic salt with a cis-TFSI anion conformation." *Dalton Transactions*(15): 2267-2271.
83. Katayanagi, H., S. Hayashi, et al. (2004). "Structure of an ionic liquid, 1-n-butyl-3-methylimidazolium iodide, studied by wide-angle X-ray scattering and Raman spectroscopy." *Chemical Physics Letters* **392**(4-6): 460-464.
84. Li, W., Z. Wang, et al. (2017). "Chemically diverse and multifunctional hybrid organic–inorganic perovskites." *Nature Reviews Materials* **2**(3): 1-18.

85. Li, Y., C. Lin, et al. (2006). "Novel  $\langle 110_L \rangle$ -Oriented Organic– Inorganic Perovskite Compound Stabilized by N-(3-Aminopropyl) imidazole with Improved Optical Properties." *Chemistry of Materials* **18**(15): 3463-3469.
86. Posypaiko, V. I. and E. Alekseeva (1987). *Phase equilibria in binary halides*, Springer.
87. Saveleva, M. S., K. Eftekhari, et al. (2019). "Hierarchy of hybrid materials—The place of inorganics-in-organics in it, their composition and applications." *Frontiers in chemistry* **7**: 179.
88. Stoumpos, C. C., D. H. Cao, et al. (2016). "Ruddlesden–Popper hybrid lead iodide perovskite 2D homologous semiconductors." *Chemistry of Materials* **28**(8): 2852-2867.
89. Tsai, H., W. Nie, et al. (2016). "High-efficiency two-dimensional Ruddlesden–Popper perovskite solar cells." *Nature* **536**(7616): 312-316.
90. Wang, X., M. Sternberg, et al. (2014). "Long-alkyl-chain-derivatised imidazolium salts and ionic liquid crystals with tailor-made properties." *Rsc Advances* **4**(24): 12476-12481.
91. Wilkes, J. S. (2004). "Properties of ionic liquid solvents for catalysis." *Journal of Molecular Catalysis A: Chemical* **214**(1): 11-17.
92. Yang, Y., F. Gao, et al. (2018). "Origin of the stability of two-dimensional perovskites: a first-principles study." *Journal of Materials Chemistry A* **6**(30): 14949-14955.
93. Zhang, X., M. Hejazi, et al. (2013). "From 1D Chain to 3D Network: A New Family of Inorganic–Organic Hybrid Semiconductors  $MO_3(L) \times (M = Mo, W; L = \text{Organic Linker})$  Built on Perovskite-like Structure Modules." *Journal of the American Chemical Society* **135**(46): 17401-17407.
94. Albero, J., Asiri, A. M. & García, H. 2016. Influence of the composition of hybrid perovskites on their performance in solar cells. *Journal of Materials Chemistry A*, **4**, 4353-4364.
95. Ding, J., Zhao, Y., Du, S., Sun, Y., Cui, H., Zhan, X., Cheng, X. & Jing, L. 2017. Controlled growth of MAPbBr<sub>3</sub> single crystal: understanding the growth morphologies of vicinal hillocks on (100) facet to form perfect cubes. *Journal of Materials Science*, **52**, 7907-7916.
96. Dubey, A., Adhikari, N., Mabrouk, S., Wu, F., Chen, K., Yang, S. & Qiao, Q. 2018. A strategic review on processing routes towards highly efficient perovskite solar cells. *Journal of Materials Chemistry A*, **6**, 2406-2431.
97. Gao, P., Ji, Y., Song, J., Zhou, G., Lai, J., Yin, X., Li, Y., Song, T., Zhao, Z. & Chen, Q. 2021. Crown ether-induced supramolecular passivation and two-dimensional crystal interlayer formation in perovskite photovoltaics. *Cell Reports Physical Science*, 100450.

98. Hirose, F., Shikaku, M., Kimura, Y. & Niwano, M. 2010. IR study on N719 dye adsorption with high temperature dye solution for highly efficient dye-sensitized solar cells. *Journal of the Electrochemical Society*, 157, B1578.
99. Kakiage, K., Aoyama, Y., Yano, T., Otsuka, T., Kyomen, T., Unno, M. & Hanaya, M. 2014. An achievement of over 12 percent efficiency in an organic dye-sensitized solar cell. *Chemical communications*, 50, 6379-6381.
100. Mcfarlane, T. D., De Castro, C. S., Holliman, P. J. & Davies, M. L. 2019. Improving the light harvesting and colour range of methyl ammonium lead tri-bromide (MAPbBr<sub>3</sub>) perovskite solar cells through co-sensitisation with organic dyes. *Chemical communications*, 55, 35-38.
101. Niu, G., Guo, X. & Wang, L. 2015. Review of recent progress in chemical stability of perovskite solar cells. *Journal of Materials Chemistry A*, 3, 8970-8980.
102. Portillo-Cortez, K., Martínez, A., Dutt, A. & Santana, G. 2019. N719 Derivatives for Application in a Dye-Sensitized Solar Cell (DSSC): A Theoretical Study. *The Journal of Physical Chemistry A*, 123, 10930-10939.
103. Roldán-Carmona, C., Malinkiewicz, O., Soriano, A., Espallargas, G. M., Garcia, A., Reinecke, P., Kroyer, T., Dar, M., Nazeeruddin, M. & Bolink, H. 2014. *Energy Environ. Sci.*, 7, 994.
104. Sheng, R., Ho-Baillie, A., Huang, S., Chen, S., Wen, X., Hao, X. & Green, M. A. 2015. Methylammonium lead bromide perovskite-based solar cells by vapor-assisted deposition. *The Journal of Physical Chemistry C*, 119, 3545-3549.
105. Weber, D. 1978. CH<sub>3</sub>NH<sub>3</sub>PbX<sub>3</sub>, ein Pb (II)-system mit kubischer perovskitstruktur/CH<sub>3</sub>NH<sub>3</sub>PbX<sub>3</sub>, a Pb (II)-system with cubic perovskite structure. *Zeitschrift für Naturforschung B*, 33, 1443-1445.
106. Zhang, F. & Zhu, K. 2020. Additive engineering for efficient and stable perovskite solar cells. *Advanced Energy Materials*, 10, 1902579.
107. Zhuang, J., Mao, P., Luan, Y., Yi, X., Tu, Z., Zhang, Y., Yi, Y., Wei, Y., Chen, N. & Lin, T. 2019. Interfacial passivation for perovskite solar cells: the effects of the functional group in phenethylammonium iodide. *ACS Energy Letters*, 4, 2913-2921.
108. Abhilash, K. A. S., T. Deepthi, et al. (2015). "Functionalised polysilsesquioxane-based hybrid silica solid amine sorbents for the regenerative removal of CO<sub>2</sub> from air." *ACS applied materials & interfaces* 7(32): 17969-17976.
109. Ava, T. T., A. Al Mamun, et al. (2019). "A review: thermal stability of methylammonium lead halide based perovskite solar cells." *Applied Sciences* 9(1): 188.
110. Boix, P. P., S. Agarwala, et al. (2015). "Perovskite solar cells: beyond methylammonium lead iodide." *The Journal of Physical Chemistry Letters* 6(5): 898-907.

111. Diau, E. W.-G., E. Jocar, et al. (2019). "Strategies to improve performance and stability for tin-based perovskite solar cells." *ACS Energy Letters* 4(8): 1930-1937.
112. Fakharuddin, A., M. Seybold, et al. (2018). "Perovskite-polymer blends influencing microstructures, nonradiative recombination pathways, and photovoltaic performance of perovskite solar cells." *ACS applied materials & interfaces* 10(49): 42542-42551.
113. Han, T.-H., J.-W. Lee, et al. (2019). "Perovskite-polymer composite cross-linker approach for highly-stable and efficient perovskite solar cells." *Nature communications* 10(1): 1-10.
114. Ji, X., X. Peng, et al. (2018). "On the performance of polymer: organometal halide perovskite composite light emitting devices: The effects of polymer additives." *Organic Electronics* 52: 350-355.
115. Jiang, J., Q. Wang, et al. (2018). "Polymer doping for high-efficiency perovskite solar cells with improved moisture stability." *Advanced Energy Materials* 8(3): 1701757.
116. Konstantakou, M. and T. Stergiopoulos (2017). "A critical review on tin halide perovskite solar cells." *Journal of Materials Chemistry A* 5(23): 11518-11549.
117. Krishnan, U., M. Kaur, et al. (2019). "Factors affecting the stability of perovskite solar cells: a comprehensive review." *Journal of Photonics for Energy* 9(2): 021001.
118. Li, C. Z., C. C. Chueh, et al. (2013). "Doping of fullerenes via anion-induced electron transfer and its implication for surfactant facilitated high performance polymer solar cells." *Advanced Materials* 25(32): 4425-4430.
119. Serrano-Lujan, L., N. Espinosa, et al. (2015). "Tin-and lead-based perovskite solar cells under scrutiny: an environmental perspective." *Advanced Energy Materials* 5(20): 1501119.
120. Sun, Y., Y. Wu, et al. (2017). "Long-term stability of organic-inorganic hybrid perovskite solar cells with high efficiency under high humidity conditions." *Journal of Materials Chemistry A* 5(4): 1374-1379.
121. Wei, J., F. Guo, et al. (2018). "SnO<sub>2</sub>-in-polymer matrix for high-efficiency perovskite solar cells with improved reproducibility and stability." *Advanced Materials* 30(52): 1805153.
122. Wei, J., F. Huang, et al. (2018). "Highly stable hybrid perovskite solar cells modified with polyethylenimine via ionic bonding." *ChemNanoMat* 4(7): 649-655.
123. Yuan, J., B. Li, et al. (2017). "Study on cobalt doped tin based perovskite material with enhanced air stability." *Materials Science in Semiconductor Processing* 57: 95-98.

124. Abdelhady, A. L., Saidaminov, M. I., Murali, B., Adinolfi, V., Voznyy, O., Katsiev, K., Alarousu, E., Comin, R., Dursun, I. & Sinatra, L. 2016. Heterovalent dopant incorporation for bandgap and type engineering of perovskite crystals. *The journal of physical chemistry letters*, 7, 295-301.
125. Babayigit, A., Ethirajan, A., Muller, M. & Conings, B. 2016. Toxicity of organometal halide perovskite solar cells. *Nature materials*, 15, 247.
126. Brivio, F., Frost, J. M., Skelton, J. M., Jackson, A. J., Weber, O. J., Weller, M. T., Goni, A. R., Leguy, A. M., Barnes, P. R. & Walsh, A. 2015. Lattice dynamics and vibrational spectra of the orthorhombic, tetragonal, and cubic phases of methylammonium lead iodide. *Physical Review B*, 92, 144308.
127. Chen, Z., Wang, J. J., Ren, Y., Yu, C. & Shum, K. 2012a. Schottky solar cells based on CsSnI<sub>3</sub> thin-films. *Applied Physics Letters*, 101, 093901.
128. Chen, Z., Yu, C., Shum, K., Wang, J. J., Pfenninger, W., Vockic, N., Midgley, J. & Kenney, J. T. 2012b. Photoluminescence study of polycrystalline CsSnI<sub>3</sub> thin films: Determination of exciton binding energy. *Journal of luminescence*, 132, 345-349.
129. Cheng, Z. & Lin, J. 2010. Layered organic–inorganic hybrid perovskites: structure, optical properties, film preparation, patterning and templating engineering. *CrystEngComm*, 12, 2646-2662.
130. Correa-Baena, J.-P., Abate, A., Saliba, M., Tress, W., Jacobsson, T. J., Grätzel, M. & Hagfeldt, A. 2017. The rapid evolution of highly efficient perovskite solar cells. *Energy & Environmental Science*, 10, 710-727.
131. Cortecchia, D., Dewi, H. A., Yin, J., Bruno, A., Chen, S., Baikie, T., Boix, P. P., Grätzel, M., Mhaisalkar, S. & Soci, C. 2016. Lead-free MA<sub>2</sub>CuCl<sub>x</sub>Br<sub>4-x</sub> hybrid perovskites. *Inorganic chemistry*, 55, 1044-1052.
132. Dawson, M., Ribeiro, C. & Morelli, M. R. 2021. MnCl<sub>2</sub> doping increases phase stability of tin halide perovskites. *Materials Science in Semiconductor Processing*, 132, 105908.
133. Dimesso, L., Mayer, T. & Jaegermann, W. 2018. Investigation of methylammonium tin strontium bromide perovskite systems. *ECS Journal of Solid State Science and Technology*, 7, R27.
134. Elseman, A. M., Shalan, A. E., Sajid, S., Rashad, M. M., Hassan, A. M. & Li, M. 2018. Copper-substituted lead perovskite materials constructed with different halides for working (CH<sub>3</sub>NH<sub>3</sub>)<sub>2</sub>CuX<sub>4</sub>-based perovskite solar cells from experimental and theoretical view. *ACS applied materials & interfaces*, 10, 11699-11707.
135. Eperon, G. E. & Ginger, D. S. 2017. B-site metal cation exchange in halide perovskites. *ACS Energy Letters*, 2, 1190-1196.
136. Goetz, K. P., Taylor, A. D., Paulus, F. & Vaynzof, Y. 2020. Shining light on the photoluminescence properties of metal halide perovskites. *Advanced Functional Materials*, 30, 1910004.

137. GREENWOOD, N. N. & EARNSHAW, A. 2012. *Chemistry of the Elements*, Elsevier.
138. He, Y., Liu, M., Darabedian, N., Liang, Y., Wu, D., Xiang, J. & Zhou, F. 2014. pH-dependent coordination of Pb<sup>2+</sup> to metallothionein<sub>2</sub>: Structures and insight into lead detoxification. *Inorganic chemistry*, 53, 2822-2830.
139. Jahandar, M., Heo, J. H., Song, C. E., Kong, K.-J., Shin, W. S., Lee, J.-C., Im, S. H. & Moon, S.-J. 2016. Highly efficient metal halide substituted CH<sub>3</sub>NH<sub>3</sub>I (PbI<sub>2</sub>) 1- X (CuBr<sub>2</sub>) X planar perovskite solar cells. *Nano Energy*, 27, 330-339.
140. Ju, M.-G., Dai, J., Ma, L. & Zeng, X. C. 2017. Lead-free mixed tin and germanium perovskites for photovoltaic application. *Journal of the American Chemical Society*, 139, 8038-8043.
141. Kim, M., Kim, G.-H., Lee, T. K., Choi, I. W., Choi, H. W., Jo, Y., Yoon, Y. J., Kim, J. W., Lee, J. & Huh, D. 2019. Methylammonium chloride induces intermediate phase stabilization for efficient perovskite solar cells. *Joule*, 3, 2179-2192.
142. Krupka, J. 2013. Contactless methods of conductivity and sheet resistance measurement for semiconductors, conductors and superconductors. *Measurement Science and Technology*, 24, 062001.
143. Lee, B., Stoumpos, C. C., Zhou, N., Hao, F., Malliakas, C., Yeh, C.-Y., Marks, T. J., Kanatzidis, M. G. & Chang, R. P. 2014. Air-stable molecular semiconducting iodosalts for solar cell applications: Cs<sub>2</sub>SnI<sub>6</sub> as a hole conductor. *Journal of the American Chemical Society*, 136, 15379-15385.
144. Lu, C.-H., Biesold-Mcgee, G. V., Liu, Y., Kang, Z. & Lin, Z. 2020. Doping and ion substitution in colloidal metal halide perovskite nanocrystals. *Chemical Society Reviews*, 49, 4953-5007.
145. Prasanna, R., Gold-Parker, A., Leijtens, T., Conings, B., Babayigit, A., Boyen, H.-G., Toney, M. F. & McGehee, M. D. 2017. Band gap tuning via lattice contraction and octahedral tilting in perovskite materials for photovoltaics. *Journal of the American Chemical Society*, 139, 11117-11124.
146. Quan, L. N., Rand, B. P., Friend, R. H., Mhaisalkar, S. G., Lee, T.-W. & Sargent, E. H. 2019. Perovskites for next-generation optical sources. *Chemical reviews*, 119, 7444-7477.
147. Serway, R. A. 1998. Principles of Physics . Fort Worth, Texas; London: Saunders College Pub. ISBN 0-03-020457-7.
148. Song, Z., Jiang, Y., Liu, J., Pan, Q., Zuo, W., Zhang, X., Liao, C. & Mei, J. 2018. Copper Incorporation in Organic-Inorganic Hybrid Halide Perovskite Solar Cells. *ChemistrySelect*, 3, 12198-12204.
149. Tang, Z.-K., Xu, Z.-F., Zhang, D.-Y., Hu, S.-X., Lau, W.-M. & Liu, L.-M. 2017. Enhanced optical absorption via cation doping hybrid lead iodine perovskites. *Scientific reports*, 7, 1-7.

150. Travis, W., Glover, E., Bronstein, H., Scanlon, D. & Palgrave, R. 2016. On the application of the tolerance factor to inorganic and hybrid halide perovskites: a revised system. *Chemical Science*, 7, 4548-4556.
151. Tsai, C.-M., Wu, H.-P., Chang, S.-T., Huang, C.-F., Wang, C.-H., Narra, S., Yang, Y.-W., Wang, C.-L., Hung, C.-H. & Diao, E. W.-G. 2016. Role of tin chloride in tin-rich mixed-halide perovskites applied as mesoscopic solar cells with a carbon counter electrode. *ACS Energy Letters*, 1, 1086-1093.
152. Wang, Y., Zhang, T., Kan, M. & Zhao, Y. 2018. Bifunctional stabilization of all-inorganic  $\alpha$ -CsPbI<sub>3</sub> perovskite for 17% efficiency photovoltaics. *Journal of the American Chemical Society*, 140, 12345-12348.
153. Willett, R., Place, H. & Middleton, M. 1988. Crystal structures of three new copper (II) halide layered perovskites: structural, crystallographic, and magnetic correlations. *Journal of the American Chemical Society*, 110, 8639-8650.
154. Xia, W., Wang, H., Zeng, X., Han, J., Zhu, J., Zhou, M. & Wu, S. 2014. High-efficiency photocatalytic activity of type II SnO/Sn<sub>3</sub>O<sub>4</sub> heterostructures via interfacial charge transfer. *CrystEngComm*, 16, 6841-6847.
155. Xiao, Z. & Yan, Y. 2017. Progress in theoretical study of metal halide perovskite solar cell materials. *Advanced Energy Materials*, 7, 1701136.
156. Yang, S. J., Choi, J., Song, S., Park, C. & Cho, K. 2021. Enhancing air-stability and reproducibility of lead-free formamidinium-based tin perovskite solar cell by chlorine doping. *Solar Energy Materials and Solar Cells*, 227, 111072.
157. Yuan, J., Li, B. & Hao, C. 2017. Study on cobalt doped tin based perovskite material with enhanced air stability. *Materials Science in Semiconductor Processing*, 57, 95-98.
158. Zhang, R., Mao, X., Cheng, P., Yang, Y., Yang, S., Wumaier, T., Deng, W. & Han, K. 2019. Bismuth doped lead-free two-dimensional tin based halide perovskite single crystals. *Journal of Energy Chemistry*, 36, 1-6.
159. Barrows, A. T., Pearson, A. J., Kwak, C. K., Dunbar, A. D., Buckley, A. R. & Lidzey, D. G. 2014. Efficient planar heterojunction mixed-halide perovskite solar cells deposited via spray-deposition. *Energy & Environmental Science*, 7, 2944-2950.
160. Birnie, D. 2004. Spin coating technique. Sol-gel technologies for glass producers and users. Springer.
161. Huang, H.-H., Liu, Q.-H., Tsai, H., Shrestha, S., Su, L.-Y., Chen, P.-T., Chen, Y.-T., Yang, T.-A., Lu, H. & Chuang, C.-H. 2021. A simple one-step method with wide processing window for high-quality perovskite mini-module fabrication. *Joule*, 5, 958-974.
162. Lang, F., Gluba, M. A., Albrecht, S., Rappich, J. R., Korte, L., Rech, B. & Nickel, N. H. 2015. Perovskite solar cells with large-area CVD-graphene for tandem solar cells. *The Journal of Physical Chemistry Letters*, 6, 2745-2750.

163. Rong, Y., Ming, Y., Ji, W., Li, D., Mei, A., Hu, Y. & Han, H. 2018. Toward industrial-scale production of perovskite solar cells: screen printing, slot-die coating, and emerging techniques. *The Journal of Physical Chemistry Letters*, 9, 2707-2713.
164. Thornton, J. A. 1973. Sputter Coating—Its Principles and Potential. *SAE Transactions*, 1787-1805.
165. Tyona, M. 2013a. A comprehensive study of spin coating as a thin film deposition technique and spin coating equipment. *Advances in materials Research*, 2, 181.
166. Tyona, M. 2013b. A theoretical study on spin coating technique. *Advances in materials Research*, 2, 195.
167. Wang, G., Liu, D., Xiang, J., Zhou, D., Alameh, K., Ding, B. & Song, Q. 2016. Efficient perovskite solar cell fabricated in ambient air using one-step spin-coating. *Rsc Advances*, 6, 43299-43303.
168. Yoo, J. J., Seo, G., Chua, M. R., Park, T. G., Lu, Y., Rotermund, F., Kim, Y.-K., Moon, C. S., Jeon, N. J. & Correa-Baena, J.-P. 2021. Efficient perovskite solar cells via improved carrier management. *Nature*, 590, 587-593.
169. Zuo, C. & Ding, L. 2021. Drop-Casting to Make Efficient Perovskite Solar Cells under High Humidity. *Angewandte Chemie International Edition*, 60, 11242-11246.



## LIST OF PUBLICATION BASED ON THESIS

1. Nisha. B, Asha. S, Vijayalakshmi. K. P, Temina. M. R, Bhuvaneswari. S, J. Cyriac,\* D. Mathew,\* Layered organic-inorganic hybrid materials based on ionic liquid and lead chloride: Insights into the structure and properties,, Journal of Molecular Liquids 307 (2020) 112947, doi.org/10.1016/j.molliq.2020.112947
2. Nisha. B, Temina M. R, J. Cyriac,\* D. Mathew,\* Co-sensitization of perovskite solar cells by organometallic compounds: Mechanism and photovoltaic characterization, Springer proceedings in energy, doi.org/10.1007/978-981-15-5955-6\_151
3. Nisha. B, Smitha. S, Temina M .R, J. Cyriac,\* D. Mathew,\* Multi-functionalized polysilsesquioxanes assisted synthesis of methylammonium tin bromide perovskite: A novel approach,, Materials Science & Engineering B 261 (2020) 114761, doi.org/10.1016/j.mseb.2020.114761
4. Nisha. B, Jayalatha T, Temina M. R, J. Cyriac,\* D. Mathew,\* Lead-free stable mixed tin-copper halide perovskite, Journal of Alloys and Compounds, 879, (2021) 160325. doi.org/10.1016/j.jallcom.2021.160325.



## LIST OF CONFERENCES

### Oral Presentations

1. 6th International Conference on Advances in Energy Research-ICAER-2017- IIT Mumbai, **December 2017**, Non-hygroscopic and thermally stable 2D hybrid perovskites: Synthesis, characterization and evaluation of photovoltaic performance. (**Best paper award**)
2. 7th International Conference on Advances in Energy Research-ICAER-2019-IIT Mumbai, **December 2019**, Co-sensitization of perovskite solar cells by organometallic compounds: Mechanism and photovoltaic characterization.

### Poster Presentations

1. International conference on material science and technology-ICMST 2018- IIST, Trivandrum, **October 2018**, Synthesis of stable mixed metal halide perovskites: Structure and optical properties
2. Polymer Conference for Young Researchers, 2018- PCYR'18-NIIST, Trivandrum, **November 2018**, entitled Environmentally stable, conducting tin halide perovskite films mediated by Polysilsesquioxanes : Synthesis, Characterization and evaluation
3. International conference on material science and technology-NCMST, 2020-IIST, Trivandrum **December 2020**, Environmentally stable oligomer-encapsulated perovskite solar cell.